ANALYSIS OF UNUSUAL ELECTRON SPIN RESONANCE SPECTRA IN DIAMONDS

By

PAUL EDWARD KLINGSPORN

Bachelor of Science
Southwest Missouri State College
Springfield, Missouri
1961

Master of Science
Kansas State College of Pittsburg
Pittsburg, Kansas
1964

Submitted to the Faculty of the Graduate College
of the Oklahoma State University
in partial fulfillment of the requirements
for the Degree of
DOCTOR OF PHILOSOPHY
August, 1969

ANALYSIS OF UNUSUAL ELECTRON SPIN RESONANCE SPECTRA IN DIAMONDS

Thesis Approved:

William J. Leivo
Thesis Adviser

Francis C. Todd

J. A. Wiebelt

Paul A. McCollum

D. D. Durham
Dean of the Graduate College

ACKNOWLEDGMENTS

The author is sincerely grateful to Dr. W. J. Leivo for his many enlightening discussions, guidance, and constant encouragement.

Special thanks are also extended to Dr. F. C. Todd, Dr. J. A. Wiebelt, and Professor Paul McCollum for their aid and cooperation.

Gratitude is expressed to Dr. J. F. H. Custers, Research Consultant, and Dr. H. B. Dyer, Director of Research of the Diamond Research Laboratory, both of Industrial Distributors (1946) Limited for furnishing semiconducting diamonds in our collection. Thanks also go to Dr. G. Switzer of the U. S. National Museum, for the loan of a semiconducting diamond.

The financial support provided by the National Science Foundation and administered through the Research Foundation of Oklahoma State University is gratefully acknowledged.

TABLE OF CONTENTS

LIST OF FIGURES

Figure | Page

LIST OF FIGURES (CONTINUED)

CHAPTER I

INTRODUCTION

Preliminary Remarks

The phenomenon of electron spin resonance involves the resonant absorption of electromagnetic radiation by unpaired electrons in the presence of a magnetic field. Electron spin resonance, often abbreviated as "ESR", can in principle be observed in a solid when unpaired electrons are present. Normally, when crystalline bonds are formed, the Pauli exclusion principle dictates that electron spins will be paired, thereby resulting in a net electronic magnetic moment of zero. However, unpaired spins may be present in a solid for a number of reasons. For example, the presence of impurity ions introduced either naturally or artifically during the growth of a crystal can give rise to the presence of unpaired electrons. Mechanical damage as well as radiation damage can result in unpaired spins localized at isolated damage sites within the lattice. For these reasons, among others, unpaired spins resulting in a net non-zero electronic magnetic moment can yield detectable ESR spectra in solids.

When it can be detected ESR provides a very useful and powerful technique in the study of solids. Each paramagnetic solid exhibits a unique spin resonance spectrum revealing the nature of interaction of the unpaired spins with their magnetic environment in the crystalline lattice. Moreover, it is often possible to investigate one type of defect center or impurity in the presence of larger concentrations of other impurities.

Previous Work on Diamond

In the perfect diamond lattice each carbon atom is linked to four nearest neighbors located at the vertices of a regular tetrahedron. Two of the six electrons belonging to each carbon atom pair off to form the inner core states; each of the remaining four electrons is paired in a covalent bond with an electron from one of the four nearest neighbors. Therefore, the net electronic magnetic moment is zero in the perfect diamond and ESR cannot be detected.

It is conceivable that bombardment of the diamond structure by high energy particles could knock carbon atoms from their normal lattice positions into interstitial sites leaving behind broken bonds which would contribute to a net electronic magnetic moment different from zero. It is not surprising, therefore, that the first electron spin resonance reported in diamond was that produced by fast neutron irradiation. The work was performed in 1954 by Griffiths, Owen, and Ward (1) who also found a single resonance line in diamonds exposed to 1-Mev electron irradiation. The results were discussed in terms of vacancies, interstitials, and aggregated defects by O'Brien and Pryce (2). Baldwin (3) later found that the "single" resonance observed by Griffiths et al. (1) in electron irradiated diamond is actually composed of three superimposed resonances, one of which is sensitive to illumination with ultraviolet light. Further ESR studies of diamonds subjected to more prolonged electron and neutron irradiation have been reported (4,5,6).

Smith, Sorokin, Gelles, and Lasher (7) first reported the observation of ESR in natural unirradiated diamonds, and attributed it to the presence of substitutional nitrogen donors. The nitrogen was supposedly included into the lattice by a natural process during the growth of the diamonds at an unknown time in the past. Loubser and DuPreez (8) later detected additional weak resonance lines associated with the ESR spectrum from nitrogen donors. The spectra referred to in references (7) and (8) will be dealt with in more detail in Chapter IV following the presentation in Chapter II of certain basic concepts concerning electron spin resonance.

Smith, Gelles, and Sorokin (9) also reported a rather complex ESR spectrum occurring in natural unirradiated diamonds which they had initially attributed to the presence of bound aluminum acceptors, but later (7) felt that further work was necessary to establish conclusively that the spectrum can be identified with aluminum acceptors.

King and Leivo (10) observed that the ESR spectra reported by Smith et al. (7,9) were sensitive to illumination with ultraviolet light. Steckelberg and Leivo (11) reported an uncommon spin resonance exhibited by natural unirradiated brown diamonds; an interesting feature of the resonance is that it disappears when the magnetic field is oriented in certain planes of the crystal. The uncommon resonance is also sensitive to exposure with ultraviolet light (10,11).

Historically, dating back to 1934 with the work of Robertson et al. (12), diamonds have been classified into "Type I" and "Type II" on the basis of their optical properties. Custers (13) discovered a Type II diamond which exhibited a relatively high electrical conductivity. He classified the non-conducting Type II diamonds as Type IIa and the conducting diamonds as Type IIb. Type IIa diamonds are fairly rare but Type IIb diamonds are still more rare. Recently a further designation into Types Ia and Ib was advanced by Dyer et al. (14), prompted by correlations between optical absorption features and the presence or absence of paramagnetic nitrogen. Almost all the neutron and electron irradiation studies mentioned above were performed on Type Ia or IIa diamonds, which do not contain nitrogen in paramagnetic form. The remaining work referred to above dealt exclusively with Type Ib diamonds in which paramagnetic nitrogen is present.

Electron spin resonance was detected in much rarer natural semiconducting diamonds (Type IIb) by Bell and Leivo (15) who also observed a similar resonance line produced in a Type Ia diamond as a result of mechanical crushing of the specimen. A correlation was found between the strength of the ESR absorption and the magnitude of the p-type conductivity of the Type IIb diamonds investigated.

The ESR spectrum from nitrogen donors has also been observed in synthetic diamonds (16,17,18). Huggins and Cannon (19) reported the nitrogen spectrum superimposed on a broad underlying resonance which they attributed to the presence of transition metal catalysts employed during preparation. Loubser and Van Ryneveld (20) reported a resonance due to nickel in synthetic diamond. To date, the resonances observed in man-made diamonds, including the nitrogen spectrum, exhibit very broad linewidths which obscure the presence of structural details observed in natural specimens with much narrow linewidths. However, with special heat treatment methods, Angel and Smith (21) have recently succeeded in reducing the nitrogen linewidths in synthetic diamonds to near that of the narrower nitrogen lines present in natural stones.

Present Study

The present work involves a study of an unusual electron spin resonance spectrum observed in natural unirradiated Type Ib diamonds. The experimental findings are analyzed in detail and a model is advanced in terms of which the observed spectrum can be reconstructed theoretically.

The design and construction of a microwave cavity and stress application device to study the effect of stress on electron spin resonance spectra is described. Efforts to detect a stress effect on ESR in Type Ib diamonds are discussed.

CHAPTER II

ELECTRON SPIN RESONANCE

Preliminary Considerations

The purpose of this chapter is to provide a physical basis for understanding the unique conditions to be fulfilled at resonance, and to discuss some of the effects resulting from interaction of the unpaired electrons with the electric and magnetic fields present within the specimen itself. In order to distinguish the electron spin angular momentum from its orbital momentum, consider first the simple classical notion in which an electron of charge e executes a circular orbit of radius r with uniform speed v as shown in Figure 1. By convention in classical mechanics the orbital angular momentum $\vec{L}$ has the direction shown. The circulating electronic charge is equivalent to a current loop and thus produces an associated magnetic moment $\vec{\mu}_L$ whose direction is that determined by convention in classical electromagnetism. The quantities L and μ_L are proportional as shown by the following simple calculation.

$$L = mvr \qquad \text{(m = mass of electron)}$$

$$\mu_L = \text{(current)x(area encompassed)} = \frac{\left(\frac{e}{c}\right)}{\left(\frac{2\pi r}{v}\right)}\pi r^2$$

Therefore,

$$\mu_L = \left(\frac{e}{2mc}\right)L \ . \qquad (2\text{-}1)$$

In the above calculation, the speed of light c is introduced because

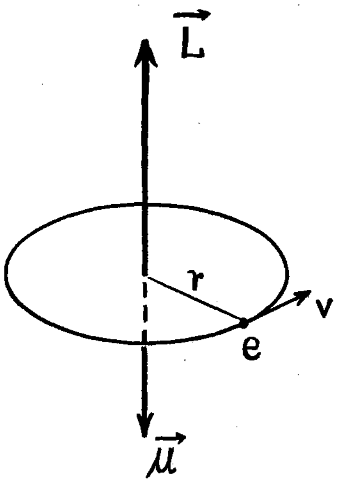

Figure 1. Classical idea of an electron executing a circular orbit with uniform speed.

the units of charge must be electromagnetic units. i.e., e/c if e is expressed in electrostatic units.

According to the hypothesis introduced by Goudsmit and Uhlenbeck (22) in 1925, the electron in addition to its orbital angular momentum $\vec{L}$ also possesses an intrinsic angular momentum or spin $\vec{S}$ whose projection S_z in any direction can have the possible values

$$S_z = \pm \frac{1}{2}\hbar , \tag{2-2}$$

where $\hbar$ is Planck's constant divided by 2π. Uhlenbeck and Goudsmit further hypothesized that associated with the intrinsic spin $\vec{S}$ is an intrinsic magnetic moment $\vec{\mu}_s$ given by

$$\vec{\mu}_s = \frac{e}{mc}\vec{S}\,. \tag{2-3}$$

Note that the proportionality constant between the intrinsic spin angular momentum of the electron and its intrinsic magnetic moment is twice that beween $\vec{L}$ and $\vec{\mu}_L$ for the orbital motion.

The proportionality factor in equation (2-3) is often expressed in terms of a quantity called the Bohr magneton and defined by

$$\beta \equiv \frac{e\hbar}{2mc}\,.$$

Equation (2-3) can then be written

$$\vec{\mu}_s = g_s \frac{\beta}{\hbar}\vec{S} \tag{2-4}$$

provided $g_s = 2$. It should be noted that a quantum-electrodynamical radiative correction to the magnetic interaction energy of an electron in a magnetic field was calculated by Schwinger (23) and corresponds to a corrected free electron g-value given by

$$g = 2.00232. \tag{2-5}$$

Stated alternatively, equations (2-2) and (2-3) indicate that the magnitude of the intrinsic magnetic moment of a free electron is greater than one Bohr magneton (0.92734×10^{-20} erg/Gauss) by the factor 0.00116.

The Resonance Phenomenon

Although the mechanism governing resonant absorption of electromagnetic radiation by unpaired spins in a magnetic field can at present only be described correctly through quantum mechanical considerations, valuable physical insight can be obtained through an appeal to classical reasoning.

Consider a single free electron in the presence of an external magnetic field $\vec{H}$ as shown in Figure 2. The field $\vec{H}$ has been arbitrarily chosen to lie along the z-axis. The two possible orientations of the intrinsic spin angular momentum $\vec{S}$ are as shown in Figures 2a and 2b, corresponding to $S_z = -\frac{1}{2}\hbar$ and $S_z = +\frac{1}{2}\hbar$, respectively. The antiparallelism of $\vec{\mu}_s$ and $\vec{S}$ results from the conventional means of choosing their directions; for a positively charged particle such as a proton the magnetic moment and spin angular momentum would point in the same direction.

From classical electromagnetism a torque $\vec{\tau}$ exerted on the intrinsic magnetic moment is given by

$$\vec{\tau} = \vec{\mu}_s \times \vec{H}. \tag{2-6}$$

Classical mechanics expresses the torque in terms of the spin angular momentum $\vec{S}$ through the relation

$$\vec{\tau} = \frac{d}{dt}\vec{S}. \tag{2-7}$$

Equations (2-4) and (2-7) allow the result in (2-6) to be expressed in the form

$$\frac{d}{dt}\vec{\mu}_s = \frac{g_s\beta}{\hbar}(\vec{\mu}_s \times \vec{H}). \tag{2-8}$$

By noting that $\vec{H} = 0\hat{i} + 0\hat{j} + H\hat{k}$, $\vec{\mu}_s = \mu_{sx}\hat{i} + \mu_{sy}\hat{j} + \mu_{sz}\hat{k}$,

and writing equation (2-8) in component form, it is easily verified that a solution for $\vec{\mu}_s$ is

$$\mu_{sx} = \mu_s \sin\theta \sin\omega_s t \tag{2-9}$$

$$\mu_{sy} = \mu_s \sin\theta \cos\omega_s t \tag{2-10}$$

$$\mu_{sz} = \mu_s \cos\theta = \text{constant} \tag{2-11}$$

where $\omega_s = g_s \frac{\beta}{\hbar} H$.

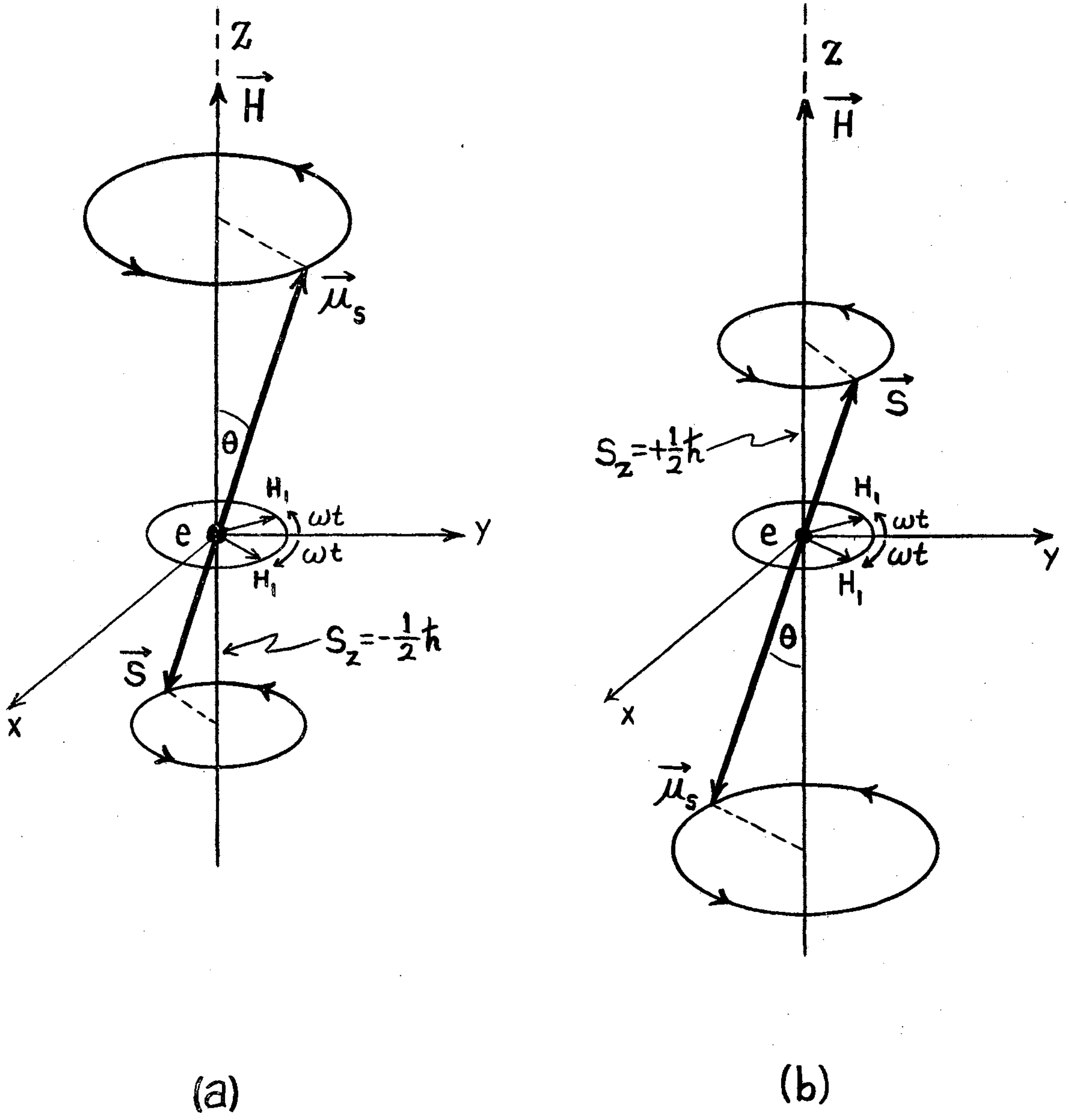

Figure 2. Possible orientations of a single electron in the presence of an external magnetic field $\vec{H}$.

Equations (2-9) and (2-10) indicate that the projections of $\vec{\mu}_s$ on the x- and y-axes oscillate harmonically in time whereas equation (2-11) reveals that the projection of $\vec{\mu}_s$ in the field direction is a constant in time. This result is known as Larmor's precession theorem which states that the intrinsic magnetic moment $\vec{\mu}_s$ (and also the intrinsic spin angular momentum $\vec{S}$) precess about the external magnetic field direction with angular frequency $\omega_s = g_s \frac{\beta}{\hbar} H$ and in such a manner that $\vec{\mu}_s$ makes a constant angle θ with $\vec{H}$.

Now consider the effect of an alternating magnetic field $2H_1 \cos \omega t$ which is applied in a direction perpendicular to $\vec{H}$, for example, along the y-axis in Figure 2. The alternating field can be considered to be composed of two circularly polarized fields, one rotating in a clockwise sense and the other counterclockwise. The two component fields can be written

clockwise: $\vec{H}_1 = H_1 \sin \omega t \, \hat{i} + H_1 \cos \omega t \, \hat{j} + 0 \, \hat{K}$

counterclockwise: $\vec{H}_1 = -H_1 \sin \omega t \, i + H_1 \cos \omega t \, \hat{j} + 0 \, \hat{K}$

At any instant the projections on the x-axis cancel to zero whereas the instantaneous projections on the y-axis combine to yield an alternating magnetic field $2H_1 \cos \omega t \; \hat{j}$ perpendicualr to $\vec{H}$.

Obviously, one of the rotating components will have the same sense as the precession of $\vec{\mu}_s$ about $\vec{H}$; assume for discussion purposes that the clockwise component has this sense. The clockwise rotating field will produce a torque $\vec{\tau}_1 = \vec{\mu}_s \times \vec{H}_1$ perpendicular to the plane in which $\vec{\mu}_s$ and $\vec{H}_1$ lie. If the angular frequency ω of $\vec{H}_1$ is less than or greater than $\omega_s = g_s \frac{\beta}{\hbar} H$ then $\vec{H}_1$ rotates out of "phase" with the projection of $\vec{\mu}_s$ in the x-y plane. The plane defined by $\vec{\mu}_s$ and $\vec{H}_1$ constantly changes in spatial orientation. Consequently, the direction of the torque $\vec{\tau}_1$ changes continually and its time-averaged effect is zero. Similar reasoning leads to a zero time-averaged effect produced by the counterclockwise rotating component.

However, when the clockwise component rotates at the frequency precisely equal to the precession frequency $\omega_S = g_S \frac{\beta}{\hbar} H$ of $\vec{\mu}_S$ about the direction of $\vec{H}$, then the rotation of $\vec{H}_1$ is synchronized with the precessional motion of $\vec{\mu}_S$. In this case the torque $\vec{\tau}_1$ will have a constant magnitude and, in time, will cause the intrinsic magnetic moment $\vec{\mu}_S$ to reorient into the antiparallel position shown in Figure 2b. This phenomenon is known as "resonance" and will occur only when the frequency of the alternating field $2H_1 \cos\omega t$ is precisely equal to the precession frequency of $\vec{\mu}_S$. It should be noted that the counter-rotating component, although its frequency at resonance is equal to the precession frequency, produces a torque whose direction and magnitude vary rapidly in time, thereby yielding no time-average effect.

The case considered above is often described by stating that the electron undergoes a transition from $S = -\frac{1}{2}$ *to* $S = +\frac{1}{2}$. Reasoning identical to the foregoing can be employed for the case in which $\vec{\mu}_S$ is initially antiparallel to $\vec{H}$ as shown in Figure 2b. The effect of the alternating field $2H_1 \cos\omega t\,\hat{j}$ would be to induce a transition from $S = +\frac{1}{2}$ to $S = -\frac{1}{2}$.

By analogy with the case of a simple bar magnet, the state in which $\vec{\mu}_S$ is "parallel" to the external field $\vec{H}$ (Figure 2a) is lower in energy than the "antiparallel" state (Figure 2b). Therefore, energy is absorbed by the electron spin in the resonant transition $S = -\frac{1}{2} \longrightarrow S = +\frac{1}{2}$, whereas energy is emitted during resonance in the transition $S = +\frac{1}{2} \rightarrow S = -\frac{1}{2}$. The energy either absorbed or emitted during resonance can be calculated with the aid of the expression for the magnetic interaction energy

$$E = -\vec{\mu}_s \cdot \vec{H} \quad . \tag{2-12}$$

Using equation (2-4), the interaction energies of the $S = +\frac{1}{2}$ and $S = -\frac{1}{2}$ states are

$$E_- = -g_s \frac{\beta}{\hbar} \vec{S}_- \cdot \vec{H} = -g_s \frac{\beta}{\hbar}\left(-\frac{1}{2}\hbar\right)H = \frac{1}{2} g_s \beta H$$

$$\text{and} \quad E_+ = -g_s \frac{\beta}{\hbar} \vec{S}_+ \cdot \vec{H} = -g_s \frac{\beta}{\hbar}\left(+\frac{1}{2}\hbar\right)H = -\frac{1}{2} g_s \beta H \ .$$

The magnitude of the energy either absorbed or emitted is

$$\Delta E \equiv |E_+ - E_-| = g_s \beta H \ . \tag{2-13}$$

That is, photons of energy

$$h\nu = g_s \beta H \tag{2-14}$$

or mean angular frequency $\omega_s = g_s \frac{\beta}{\hbar} H$ can induce transitions between the two possible states.

When the resonant transition $S = -\frac{1}{2} \longrightarrow S = +\frac{1}{2}$ occurs, the electron absorbs a photon of mean frequency ν from the alternating field $2H_1 \cos \omega_s t$; a photon of the same energy is emitted into the field during the transition $S = +\frac{1}{2} \longrightarrow S = -\frac{1}{2}$. The two transitions have the same a priori probability. Therefore, in a solid containing unpaired spins as many would emit energy as absorb energy during resonance. No observable effect would result. However, nature has provided a difference in population between the two spin states at thermal equilibrium, which is given by

$$\frac{N_+}{N_-} = e^{-\frac{\Delta E}{KT}} = e^{-\frac{g_s \beta H}{KT}} \ . \tag{2-15}$$

This is the classical Maxwell-Boltzman distribution giving the ratio of the number of electrons in the lower energy spin-state to the number in the higher energy state under thermal equilibrium conditions at temperature T. When resonance occurs the number of electrons absorbing energy will exceed those emitting energy by the factor $e^{+\frac{g_s\beta H}{KT}}$, i.e. a net absorption will occur. During resonance the population distribution in equation (2-15) is temporarily reversed, i.e., thermal equilibrium among the spin-states is destroyed; however, nature has also arranged for thermal equilibrium to be restored. For example, the excess energy absorbed by the spins is transferred to the lattice through a process known as "spin-lattice relaxation". Also, the phase coherence of precessional motion established during resonance is destroyed to thermal equilibrium conditions through the effect of "spin-spin" interactions.

A few further remarks are in order. The presence of $\vec{H}$ causes a precession of $\vec{\mu}_s$ about $\vec{H}$ with frequency $\omega_s = g_s \frac{\beta}{\hbar} H$. By the same token, $\vec{\mu}_s$ should exhibit a precessional motion about the components H_1 at a frequency $\omega_1 = g_s \frac{\beta}{\hbar} H_1$. In practice, however, $\omega_s \gg \omega_1$ because H is several thousand Gauss while H_1 is less than one Gauss. It is clear that for off-resonance conditions $(\omega \neq \omega_s)$ the precessional tendency of $\vec{\mu}_s$ about the rotating components introduces only a minor perturbation on the main precession about $\vec{H}$. The same is true concerning the counter-rotating component even when $\omega = \omega_s$. At resonance when one of the components H_1 rotates in synchronism with $\vec{\mu}_s$, there will be many precessions about $\vec{H}$ before a half-precession (i.e., transition) occurs about $\vec{H}_1$. This is true because $\omega_s \gg \omega$.

Finally, from quantum mechanics the commutation of the spin angular momentum $\vec{S}$ with the Hamiltonian $\mathcal{H}$ is given by (24)

$$[\mathcal{H},\vec{S}\,]\equiv(\mathcal{H}\vec{S}-\vec{S}\mathcal{H})=-i\hbar\frac{d\vec{S}}{dt}\ , \tag{2-16}$$

where in this case $\mathcal{H}=-\vec{\mu}_s\cdot\vec{H}=-g_s\frac{\beta}{\hbar}\,\vec{S}\cdot\vec{H}$. This gives

$$(\vec{S}\cdot\vec{H})\vec{S}-\vec{S}(\vec{S}\cdot\vec{H})=\frac{i\hbar}{g_s\frac{\beta}{\hbar}}\frac{d\vec{S}}{dt}\ . \tag{2-17}$$

When equation (2-17) is written in component form and the commutation relations

$$[\mu_{sx},\mu_{sx}]=0,\ [\mu_{sz},\mu_{sx}]=i\hbar\mu_{sy}\ ,\ [\mu_{sx},\mu_{sy}]=i\hbar\mu_{sz}$$

are applied, the following result is obtained upon combining terms.

$$g_s\frac{\beta}{\hbar}(\vec{S}\times\vec{H})=\frac{d\vec{S}}{dt} \tag{2-18}$$

Note that Planck's constant has canceled from both sides of the latter expression and that it is identical to the classical equation of motion (2-8). This accounts for the success of the classical analysis of the resonance phenomenon.

Rabi (25) treated the resonance problem classically with the aid of a rotating reference frame attached to the component field $\vec{H}_1$. His paper includes a quantum mechanical analysis employing unitary operators and transformations.

The Spin Hamiltonian Characterizing the Zeeman and Hyperfine Interactions

The previous considerations concerning resonant absorption by a single unpaired electron can be extended to more complicated systems. For systems involving more than one electron the Wigner-Eckart theorem (26) from quantum mechanics assures that the net magnetic moment $\vec{\mu}$

will be proportional to the resultant angular momentum $\vec{J}$. In the case of a free paramagnetic ion, for example, the proportionality is given by

$$\vec{\mu} = g\frac{\beta}{\hbar}\vec{J} \quad , \tag{2-19}$$

where $\vec{J} = \vec{L} + \vec{S}$ and g is the familiar Lande g-factor from atomic spectroscopy.

$$g = 1 + \frac{J(J+1) + S(S+1) - L(L+1)}{2J(J+1)} \tag{2-20}$$

For the special case $J = L + S = 0 + \frac{1}{2}$ it is readily seen that equations (2-19) and (2-20) reduce to the expression in equation (2-3) for a free electron.

When paramagnetic ions are present in a solid the free ion expression for g in equation (2-20) is not valid. The g-factor then assumes the role of a parameter to be determined experimentally. Magnetic interactions of the spin with the orbital angular momentum are responsible for the experimentally observed deviations in g value from the free electron value in equation (2-5).

Quantum mechanics predicts that 2J+1 energy levels will result when a paramagnetic ion with resultant angular momentum $\vec{J}$ is subjected to an externally applied magnetic field $\vec{H}$ (27). This effect is known as the Zeeman interaction. Following the reasoning given earlier for a single electron, application of an alternating magnetic field $2\vec{H}_1 \cos\omega t$ at right angles to $\vec{H}$ can induce transitions between the 2J+1 energy levels. Selection rules allow only those transitions for which $\Delta J = \pm 1$. The Zeeman effect is the dominant interaction in electron spin resonance and is characterized by an expression known as the Hamiltonian $\mathcal{H}$, where

$$\mathcal{H} = \vec{\mu}\cdot\vec{H} = \frac{\beta}{\hbar}\bar{g}\cdot\vec{S}\cdot\vec{H} \ . \qquad (2\text{-}21)$$

The second equality in equation (2-21) follows from the Wigner-Eckart theorem, and $\vec{S}$ is called the "effective spin". As mentioned earlier, the g factor is not always a simple scalar as in the case of the Landé g-factor for free paramagnetic ions. The magnitude of g may depend upon the orientation of a paramagnetic solid relative to the external magnetic field $\vec{H}$. That is, g can have anisotropic properties and is therefore denoted as a tensor in equation (2-21). In the general case g can be expressed as a symmetric tensor of rank two and written in matrix form as follows.

$$g' = \begin{bmatrix} g'_{11} & g'_{12} & g'_{13} \\ g'_{21} & g'_{22} & g'_{23} \\ g'_{31} & g'_{32} & g'_{33} \end{bmatrix} \qquad (2\text{-}22)$$

The matrix for g is "Hermitian" because the components are real numbers and the symmetry property $g_{ij} = g_{ji}$ holds. Since any Hermitian matrix can be diagonalized, it follows that a similarity transformation $\bar{Q}$ exists such that $\bar{g} = \bar{Q}\bar{g}'\bar{Q}^{-1}$.

where $\bar{g}$ is

$$g = \begin{bmatrix} g_1 & 0 & 0 \\ 0 & g_2 & 0 \\ 0 & 0 & g_3 \end{bmatrix} \ . \qquad (2\text{-}23)$$

When $\bar{g}$ is expressed in diagonal form the additional subscripts are usually omitted. The quantities g_1 , g_2 , and g_3 are called the principal components of the g-tensor and lie along the three mutually perpendicular directions X_1 , X_2 , and X_3 . For an arbitrary orientation of a paramagnetic crystal relative to the externally applied magnetic field $\vec{H}$, the effective value of $\bar{g}$ in the direction of $\vec{H}$ is given by

$$g^2 = g_1^2\cos^2\varphi_1 + g_2^2\cos^2\varphi_2 + g_3^2\cos^2\varphi_3 \qquad (2\text{-}24)$$

or

$$g = \sqrt{g_1^2\cos^2\varphi_1 + g_2^2\cos^2\varphi_2 + g_3^2\cos^2\varphi_3}$$

where φ_1 , φ_2 , and φ_3 are the angles between $\vec{H}$ and the principal component directions X_1 , X_2 , and X_3 , respectively.

Other interactions can occur between the unpaired electron and its surroundings within the crystal. Electrostatic interaction with a nucleus possessing a quadrupole moment can affect the energy level separation. Also, an effect known as hyperfine interaction results from magnetic interaction of the electron spin with a nucleus of non-zero spin. As a final example, microscopic crystalline electric fields produced by charges in the vicinity of a paramagnetic species can cause splitting of the energy levels. The nature of the splitting depends not only upon the host crystal but also whether the paramagnetic species is a member of the rare earth or iron group. The analysis of any given ESR spectrum usually involves only one or two significant interactions in addition to the Zeeman interaction. In any given case, other interactions are either negligible or non-existent.

In addition to the dominant Zeeman interaction, the present study is concerned with hyperfine interaction which arises from magnetic interaction of an electron with the magnetic field produced by a nucleus of non-zero spin. The Hamiltonian expressing the magnetic interaction energy between a nucleus with spin $\vec{I}$ and the electron spin $\vec{S}$ is of the following form (28).

$$\mathcal{H}_{Hyperfine} = g_s g_I \beta\beta_N \left\{ \left[\frac{\vec{I}\cdot\vec{S}}{r^3} - \frac{3(\vec{I}\cdot\vec{r})(\vec{S}\cdot\vec{r})}{r^5} \right] + \frac{8\pi}{3}\delta(\vec{r})\vec{S}\cdot\vec{I} \right\} \tag{2-25}$$

g_s is the free electron g-value and g_I is the g-factor of the particular nucleus whose spin is $\vec{I}$. The nuclear magneton β_N is obtained from the Bohr magneton in equation (2-4) by replacing the electron mass m by the mass of the proton. The first two terms in equation (2-25) express the anisotropy of the interaction. The last term, called the "Fermi contact interaction", contains the Dirac delta function which is zero everywhere except at the nucleus. Since sufficient knowledge of the electronic wave function is never available to calculate expectation values of the individual terms in equation (2-25), the spin Hamiltonian for the hyperfine interaction is usually expressed in the form

$$\mathcal{H}_{Hyperfine} = \bar{I}\cdot\bar{A}\cdot\bar{S}\,, \tag{2-26}$$

where the components of $\bar{A}$ are to be determined through experimental analysis. In general, $\bar{A}$ is a symmetric tensor of rank two and can be represented in matrix form by

$$A' = \begin{bmatrix} A'_{11} & A'_{12} & A'_{13} \\ A'_{21} & A'_{22} & A'_{23} \\ A'_{31} & A'_{32} & A'_{33} \end{bmatrix} . \tag{2-27}$$

Since the components of $\bar{A}$ are real numbers and $\bar{A}$ is a symmetric tensor, it follows as in the case of the $\bar{g}$ tensor that a principal coordinate system can be found in which $\bar{A}$ is diagonal. The elements A_1, A_2, and A_3 are the principal components of the $\bar{A}$ tensor. The principal axes

$$A = \begin{bmatrix} A_1 & 0 & 0 \\ 0 & A_2 & 0 \\ 0 & 0 & A_3 \end{bmatrix} \tag{2-28}$$

along which A_1, A_2, and A_3 lie are designated by (y_1, y_2, y_3) to distinguish them from the principal axes of the g-tensor in equation (2-23). In other words, it is not true in general experimentally that the $\bar{g}$ and $\bar{A}$ tensors are diagonal in the same coordinate system.

If the externally applied magnetic field $\vec{H}$ makes angles Φ_1, Φ_2, and Φ_3 with the $\bar{A}$ tensor principal axes y_1, y_2, and y_3, respectively, then the effective value of $\bar{A}$ in the direction of $\vec{H}$ is

$$\begin{gathered} A^2 = A_1^2\cos^2\Phi_1 + A_2^2\cos^2\Phi_2 + A_3^2\cos^2\Phi_3 \\ \text{or} \quad A = \sqrt{A_1^2\cos^2\Phi_1 + A_2^2\cos^2\Phi_2 + A_3^2\cos^2\Phi_3} \end{gathered} \tag{2-29}$$

The result in equation (2-29) is analogous to the expression for the effective value of $\bar{g}$ in equation (2-24).

The hyperfine interaction can be understood by considering the magnetic field set up by the nucleus at the position of the unpaired electron. The nucleus with spin $\vec{I}$ is quantized in the presence of an external magnetic field and is thereby restricted to only 2I+1 allowed orientations in the field. The magnetic field at the electron position is different for each of the allowed orientations of the nuclear spin; hence, the magnetic interaction energy depends upon the nuclear orientation. For example, consider the simple case in which a single electron interacts with a nucleus of spin I=1. In the absence of an external magnetic field, all allowed orientations of a magnetic moment (either electronic or nuclear) are equal in energy, as indicated on the extreme left in Figure 3. Application of an external magnetic field removes the energy degeneracy of the electron spin states as shown in the middle portion of Figure 3. A nucleus with spin I=1 can assume 2I+1 or three allowed orientations in the external field. For each nuclear orientation, each electron spin state has a different interaction energy. Therefore, as shown in Figure 3 each electron energy level is "split" into three levels as a result of hyperfine interaction with the spin-one nucleus.

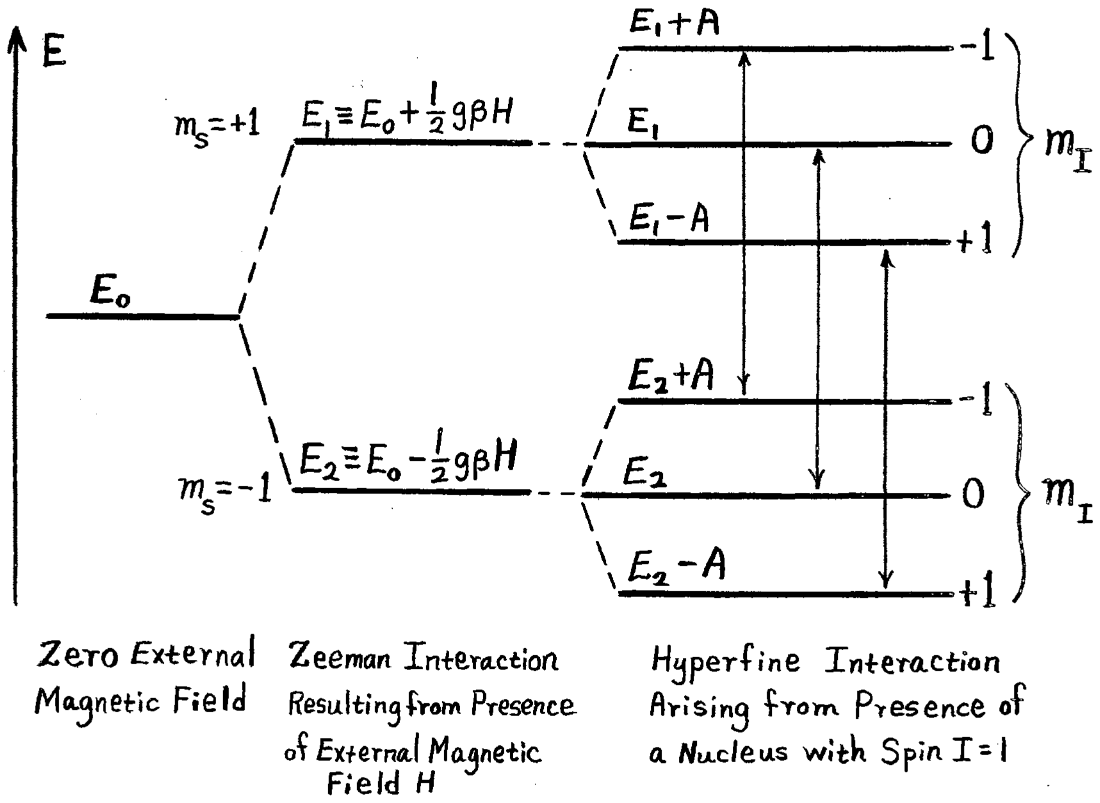

Figure 3. Hyperfine interaction of an electron with a nucleus of spin I=1.

It was pointed out earlier that the allowed orientations of the electron spin $\vec{S}$ are those for which the projections S_z on the direction of $\vec{H}$ are $S_z = \pm\frac{1}{2}\hbar$. This is often expressed in terms of the electron spin quantum number m_s by writing

$$S_z = \frac{1}{2} m_s \hbar \quad , \quad m_s = \pm 1 \quad . \tag{2-30}$$

Similarly, the allowed orientations of a nucleus with spin $\vec{I}$ are those for which the projections I_z on the external field direction are given by

$$I_z = m_I \hbar \tag{2-31}$$

where the nuclear spin quantum number m_I can have the values

$$m_I = I, \ I-1, \ I-2, \ldots -I \quad . \tag{2-32}$$

Resonant absorption of electromagnetic radiation can occur only when the electron spin changes orientation relative to $\vec{H}$ without a simultaneous change in nuclear spin orientation. That is, the selection rules for the allowed ESR transitions are $\Delta m_s = \pm 1$, $\Delta m_I = 0$, and transitions occur only between the levels connected by arrows in Figure 3. The physical basis underlying the selection rules can be understood by the following reasoning. When the electron undergoes the resonant transition $m_s = -1 \longrightarrow m_s = +1$, a photon of mean energy $h\nu = g_s \beta H$ is absorbed from the alternating field perpendicular to $\vec{H}$. Conservation of energy is obeyed in that the gain in energy of the electron is equal to the energy of the photon absorbed. Now, the change in angular momentum of the electron during the transition

$m_s=-1 \rightarrow m_s=+1$ is $\Delta S_z=\frac{1}{2}\hbar-(-\frac{1}{2}\hbar)=\hbar$, or one unit of Planck's constant divided by 2π. The spin angular momentum of any photon is $\hbar$. For each resonant absorption by an electron one unit of angular momentum $\hbar$ is extracted from the alternating electromagnetic field, but the same unit of spin angular momentum is acquired by the electron. Therefore, both conservation of energy and angular momentum are satisfied by resonant transitions of the type $\Delta m_s=\pm 1, \Delta m_I=0$. Note that for a transition involving $\Delta m_s=\pm 1$ and $\Delta m_I=\pm 1$, energy is conserved through absorption of a photon whose energy is $g_s\beta H$, but angular momentum is not conserved because only one unit $\hbar$ is given forth by the alternating field whereas a total angular momentum of $2\hbar$ is required if both the electron and nuclear spins are to reorient relative to the external field $\vec{H}$. It should be noted that conservation of energy and angular momentum also hold for transitions of the type $\Delta m_s=0, \Delta m_I=\pm 1$, which are essentially nuclear resonance transitions. For a given external magnetic field strength H, the resonant absorption occurs at a frequency lower than the ESR frequency by the factor $\frac{\beta}{\beta_N} \approx 1840$.

Combining equations (2-21) and (2-26), the spin Hamiltonian for the Zeeman and hyperfine interactions is given by

$$\mathcal{H}=\beta \bar{g}\cdot\bar{S}\cdot\bar{H}+\bar{I}\cdot\bar{A}\cdot\bar{S}\,. \qquad (2\text{-}33)$$

$\bar{S}$ and $\bar{I}$ are the dimensionless electron and nuclear spin operators, respectively. The allowed energy levels can be obtained from the Hamiltonian in equation (2-33). When the anisotropy in $\bar{g}$ an $\bar{A}$ is neglected the energy levels (for $S = \frac{1}{2}$) of the Hamiltonian in equation (2-33) are given by the Breit-Rabi (29) expression.

$$E(I\pm\tfrac{1}{2},m_I\pm\tfrac{1}{2})=-\frac{A}{4}\pm\frac{A(2I+1)}{4}\left[1+\frac{8(m_I\pm\frac{1}{2})g\beta H}{A(2I+1)^2}+\frac{4g^2\beta^2H^2}{A^2(2I+1)^2}\right]^{\frac{1}{2}} \quad (2\text{-}34)$$

The positive and negative signs correspond to the two electron spin states represented by the spin quantum numbers $m_S=+1$ and $m_s=-1$, respectively. The Breit-Rabi relation in equation (2-34) can be rearranged and written in the form

$$E(I\pm\tfrac{1}{2},m_I\pm\tfrac{1}{2})=-\frac{A}{4}\pm\frac{g\beta H}{2}\left[1+\frac{2(m_I\pm\frac{1}{2})A}{g\beta H}+\frac{A^2(2I+1)^2}{4g^2\beta^2H^2}\right]^{\frac{1}{2}} \quad (2\text{-}35)$$

The energy absorbed in the transition $m_S=-1\longrightarrow m_s=+1$, $\Delta m_I=0$ can be obtained from equation (2-35).

$$h\nu=E(I+\tfrac{1}{2},m_I+\tfrac{1}{2})-E(I-\tfrac{1}{2},m_I-\tfrac{1}{2}) \quad (2\text{-}36)$$

The hyperfine interaction energy A is normally much smaller than the Zeeman energy $g\beta H$, and therefore the terms involving $\frac{A}{g\beta H}$ in the Breit-Rabi expression are much less than unity. This is especially true in the present study. Under the circumstances, valid use can be made of the approximation

$$(1+X)^{\frac{1}{2}}=1+\frac{X}{2}+\frac{X^2}{4}\quad,\quad X\ll 1\ . \quad (2\text{-}37)$$

Applying the approximation to the energy level expression in equation (2-35) and substituting into equation (2-36), it is found that the allowed ESR transitions ($\Delta m_S=\pm1$, $\Delta m_I=0$) are given to second order in $\frac{A}{g\beta H}$ by the following relation.

$$h\nu=g\beta H+m_I A+\frac{A^2}{2g\beta H}\left[I(I+1)-m_I^2\right] \quad (2\text{-}38)$$

Since ESR experiments are performed at constant frequency for practical reasons, it is convenient to solve equation (2-38) explicitly for the variable magnetic field strength H,

$$H = \frac{1}{2g\beta}\left[(h\nu - m_I A) + \sqrt{(h\nu - m_I A)^2 - 2A^2\left[I(I+1) - m_I^2\right]}\right] \qquad (2\text{-}39)$$

Although the Breit-Rabi expression from which equation (2-38) was obtained neglects any anisotropy in g the expression is entirely adequate for the present analysis because the maximum anisotropy in g for the unusual ESR spectrum is only 0.06% of the average magnitude of g. Furthermore, although equation (2-38) neglects anisotropy in A for the second order terms the magnitude of A ($\sim 6 \times 10^{-4}$ cm^{-1}) is sufficiently small so that the second order terms do not contribute significantly anyway.

CHAPTER III

INSTRUMENTATION

Simple Bridge Spectrometer

It was shown in Chapter II that resonant absorption by unpaired electrons will occur if the small field $2H_1 \cos \omega t$ oscillates at the same frequency as the precession frequency of the unpaired electrons in the presence of the large field $\vec{H}_0$. The condition for resonance was expressed in equation (2-14) and is given by

$$h\nu = g_s \beta H \quad . \tag{3-1}$$

According to the Boltzman distribution, equation (2-15), for thermal equilibrium conditions at absolute temperature T, the greatest population difference between the two spin states occurs at maximum separation of the energy levels. The energy level separation $\Delta E \equiv h\nu$ is obviously a maximum for maximum frequency ν. That is, maximum absorption or maximum sensitivity at a given temperature T will be obtained at the highest possible frequency ν of the small oscillating field. A convenient region of operation results in a practical value of ν lying in the approximate range 9-25 $Kmc\ sec^{-1}$ which is in the microwave region. The spectrometer employed in the present study operates at a nominal frequency of 9.5 $Kmc\ sec^{-1}$ which is in the "x-band" region of the microwave spectrum. At this frequency equation

(3-1) predicts that resonant absorption by a free electron will occur at a magnetic field $\vec{H}$ having the magnitude $H \approx 3400$ Gauss.

In principle, resonance can be achieved either by maintaining $\vec{H}$ constant in magnitude and varying ν until the equality in equation (3-1) is satisfied, or by holding ν constant and varying H slowly to achieve the equality. The latter alternative is superior because practical considerations make it convenient and more satisfactory to stabilize the microwave frequency ν and slowly sweep the magnetic field H through the resonance condition.

Before discussing the sophisticated ESR spectrometer used in the present study, consider first the simplest form of a bridge spectrometer shown diagrammatically in Figure 4. The large magnetic field $\vec{H}$ is supplied by the electromagnet. Microwave energy supplied by the klystron is transmitted by waveguide and enters arm 1 of a waveguide junction called a "magic Tee". At the junction a portion of the energy is diverted into arms 2 and 3, and in general, a portion passes into arm 4. The microwave energy in arm 2 sustains an electromagnetic field configuration or "mode" within the microwave cavity. The cavity is positioned in the presence of the large magnetic field $\vec{H}$ such that the microwave magnetic field $2\vec{H}_1 \cos\omega t$ oscillates in a direction perpendicular to $\vec{H}$. The paramagnetic sample is placed in the region of maximum microwave magnetic field.

The magic Tee has the property that no microwave energy is transmitted by arm 4 provided arms 2 and 3 share equal amounts of energy (30). The losses in arm 2 will depend upon the nature of the microwave cavity and the particular paramagnetic specimen under investigation. The device called a "slide screw tuner" inserted in arm 3

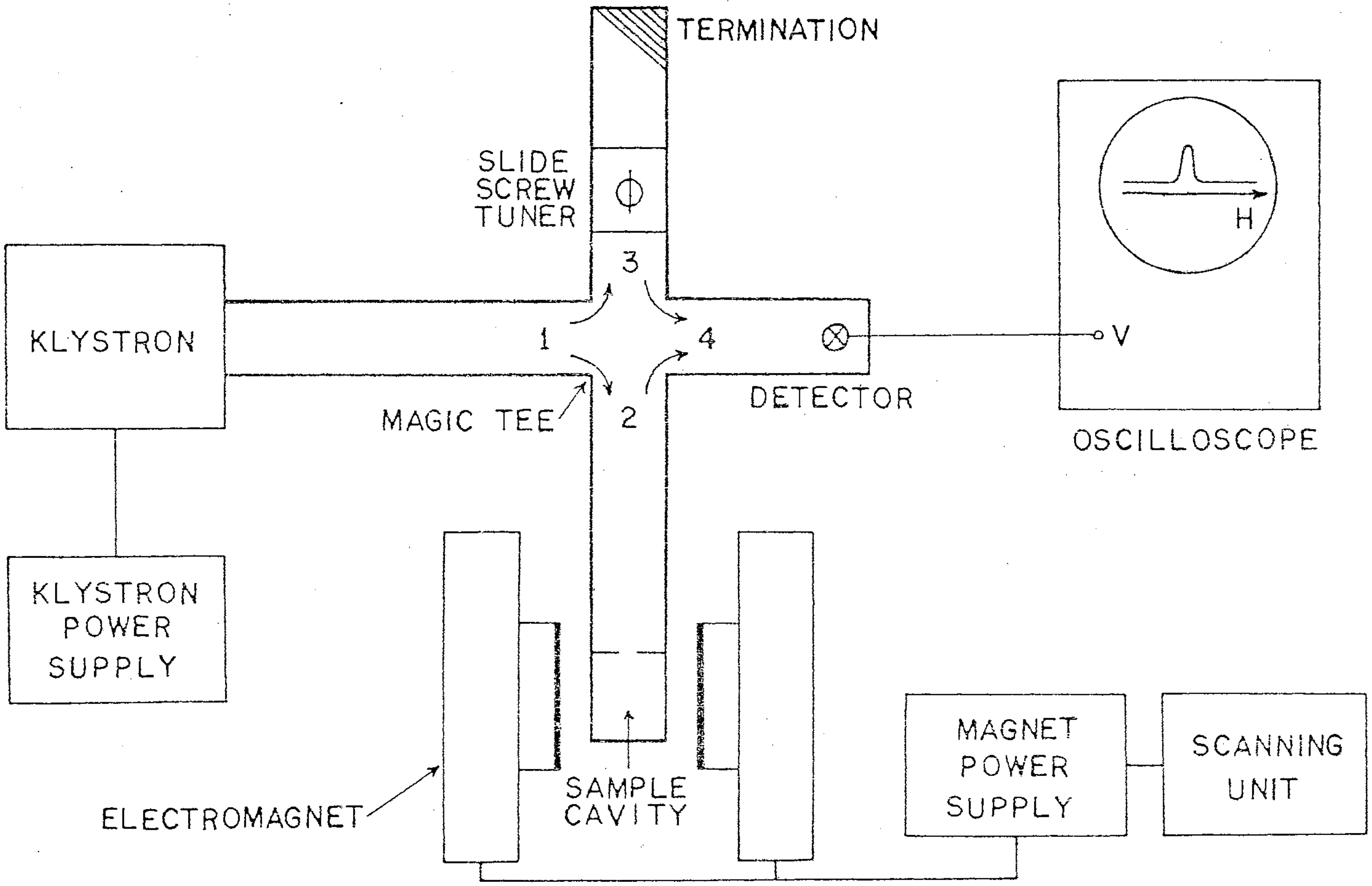

Figure 4. A Simple ESR Bridge Spectrometer.

contains a metal probe whose depth of insertion in the region of maximum microwave electric field can be varied. The position of the probe can also be varied along the length of the waveguide. For a given cavity and sample the slide screw tuner can be adjusted so that arms 2 and 3 are electrically matched. Under this condition the magic Tee prevents any energy from arriving at the detector in arm 4. However, when the magnitude of H is adjusted to satisfy the condition in equation (3-1), resonance occurs resulting in an absorption of energy from the microwave field in the cavity. During resonance there is an unbalance in energy between arms 2 and 3, thereby allowing energy to pass into arm 4 where the detector responds to the magnitude of energy unbalance.

Spectrometer Employed in the Present Study

Electron spin resonance can be detected with the simple bridge arrangement depicted in Figure 4, but not with a high degree of sensitivity. Several factors affect the sensitivity of detection, and their consideration leads to a more complex system. The ESR spectrometer employed in the present study was constructed in this laboratory by M. D. Bell (31), but it includes several Varian components. The system is shown diagrammatically in Figure 5. Microwave radiation proceeding directly from the Varian Type V-153 reflex klystron passes through two ferrite isolators before entering arm 1 of the magic-Tee T_1. The device called a ferrite isolator has a non-linear property which permits energy to transmit freely in one direction but not in the reverse (32). Therefore, any microwave radiation reflected from various parts of the system is attenuated in the isolator and is prevented from producing

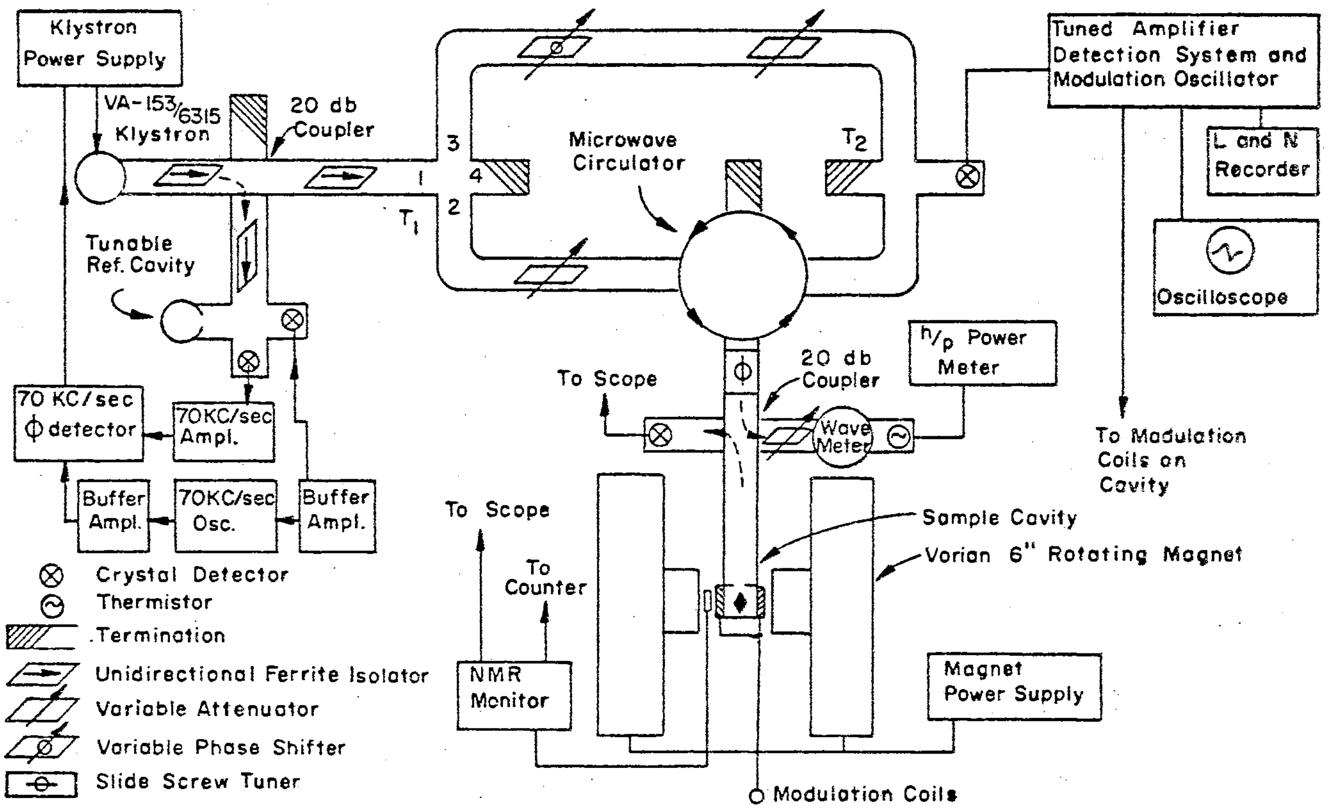

Figure 5. Electron Spin Resonance Spectrometer
Used in the Study.

undesirable changes in the klystron frequency. Radiation entering through arm 1 is divided by arms 2 and 3. Arm 2 directs energy through a precision variable attenuator and then to the microwave ferrite circulator. The circulator has the property that radiation entering by one arm can exit only by a second arm in sequence (33). The energy entering arm 1 of the circulator is exited by arm 2 and passes into the Varian V-4531 rectangular parallelopiped cavity. Energy reflected from the cavity re-enters the circulator by arm 2, but exits by arm 3. Arm 3 of the circulator directs the radiation to the magic Tee T_2 where the energy is divided, half being detected by the crystal detector in arm 2 and the remaining being dissipated by arm 3 of T_2. The radiation transmitted by arm 3 of T_1 is employed in biasing the crystal detector; the bias voltage to the crystal is adjusted by means of the variable attenuator in the bias arm. The variable phase shifter in the bias arm together with the slide screw tuner in the arm containing the cavity provide a means of electrical tuning used in balancing the bridge immediately before recording the spectrum of a given paramagnetic sample.

The large magnetic field $\vec{H}$ causing precession of the unpaired spins is produced by a Varian magnet which can be rotated about a vertical axis. The 6" diameter pole pieces are separated by 2.875". The coils of the electromagnet are energized by the current-regulated model V2200 Varian magnet power supply. Since paramagnetic samples necessarily occupy a finite region in space, it is desirable that the field H possess a high degree of homogeneity to assure that all the spins are exposed to the same magnetic field strength. The Varian magnet produces a field whose homogeneity is one part in 10^4 over a circular region approximately 1" in diameter lying in the median plane between the pole faces and centered about their central axis. Since the largest dimension of any of the diamonds investigated is approximately 0.2", the degree of homogeneity is considerably greater over the small region occupied by the specimens.

One of the most important factors affecting the sensitivity of detection is the degree of monochromaticity in the klystron frequency. In Figure 5 the waveguide section leading directly from the klystron contains a 20db directional coupler whose function is to divert a portion of the microwave energy for use in stabilizing the klystron frequency. The method of stabilization utilized is known as the "modified Pound" system (34); the circuitry is shown in more expanded form in Figure 6. The method employs a cylindrical cavity serving as a reference the frequency of which can be varied over a small but suitable range by varying its length with the aid of a precision micrometer movement. After the reference cavity resonant frequency is matched to that of the sample cavity, the modified Pound stabilization system maintains the klystron frequency locked to the resonant frequency of the sample cavity. The small portion of energy diverted by the coupler enters arm 1 of the magic Tee, where it is then divided by arms 2 and 3. Arms 2 and 3 are adjusted to have equal effective lengths, and arm 3 is a matched load so that no radiation is reflected in the absence of modulation. In operation, the microwave radiation entering arm 3 is modulated at 70 Kc sec^{-1}. A portion of the reflected radiation enters arm 1 to be dissipated in the ferrite isolator and thereby prevented from perturbing the klystron frequency. The portion entering arm 4 has superimposed upon it a wave reflected from the reference

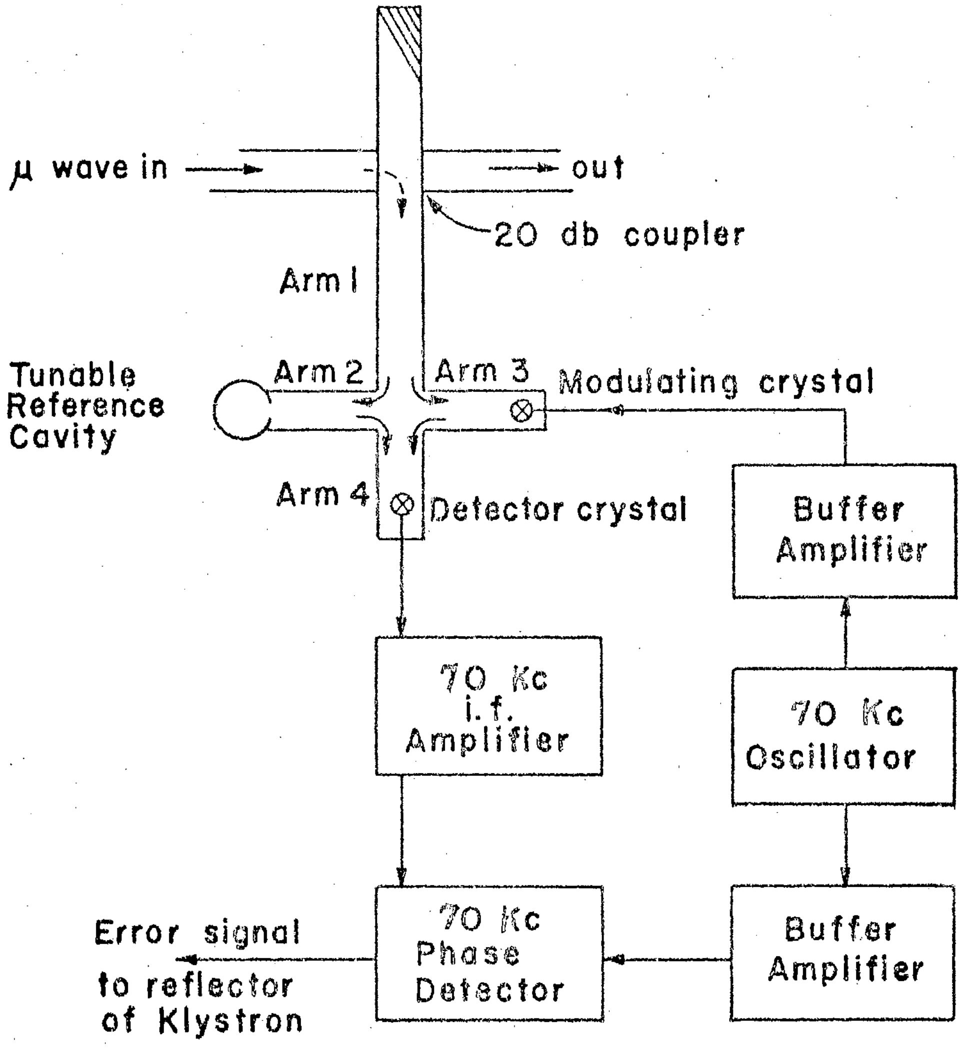

Figure 6. Modified Pound Frequency Stabilizer.

cavity. If the klystron drifts from the resonant frequency of the reference cavity, a reactive component will appear in the reflected wave from the cavity. The sign of the reactive change will depend upon whether the klystron frequency is greater or less than that of the reference cavity. The 70 Kc $\sec^{-1}$ output of the detector crystal will have an amplitude proportional to the reactive component in the wave reflected from the reference cavity, and its phase will differ by 180° on either side of the cavity resonance. The detector output has an amplitude which is proportional to the klystron frequency deviation; the phase of the output is determined by the direction of the frequency deviation and is amplified by a 70 Kc $\sec^{-1}$ amplifier. A crystal diode phase detector is employed to compare the amplified signal with a reference signal from the 70 Kc $\sec^{-1}$ oscillator. The phase detector produces a dc output the amplitude of which is determined by the magnitude of frequency deviation of the klystron. The sign of the dc signal depends upon the phase of the 70 Kc $\sec^{-1}$ signal from the detector. The ± dc or "error signal" is applied to the reflector of the klystron in a manner to correct for the frequency deviation. By this method the klystron frequency is stabilized to the resonant frequency of the Varian sample cavity with a degree of stabilization better than one part in 10^6. A Hewlett-Packard model 540 B transfer oscillator is used in conjunction with the model 525 D electronic counter for measuring the klystron frequency.

As a further means of increasing the signal-to-noise ratio, the spectrometer in Figure 5 employs modulation of the magnetic field H. The output signal-to-noise ratio of the spectrometer increases as the square root of the modulation field frequency (35). The Varian model

V-4560 modulation and control unit produces modulation of the magnetic field H at a frequency of 100 Kc sec^{-1}, which is the highest practicable value. The unit contains a 100 Kc sec^{-1} oscillator which drives a power amplifier which in turn excites the modulation field coils to produce magnetic field modulation at the position of the sample. Upon resonance, the sample converts the magnetic field modulation into modulation of the microwave radiation field, which in turn is detected, amplified, and finally compared with the original 100 Kc sec^{-1} modulation by means of a phase sensitive detector. The output of the phase sensitive detector is connected to a pen-recorder enabling the spectra to be displayed graphically on chart paper.

When the amplitude of the magnetic field modulation is much less than the line width of the resonance being investigated, the result is a signal which approaches the derivative of the resonance. This is true because the modulation and phase detection process measures the change in signal of a magnetic field dependent phenomenon for a small change in magnetic field as a function of the magnetic field itself. This is precisely the definition of the derivative of the signal with respect to the magnetic field. Therefore, the spectra traced out by the recorder appear in the form of a derivative of the ordinary absorption peak.

CHAPTER IV

INVESTIGATION OF UNUSUAL ESR SPECTRA IN NATURAL DIAMONDS

Review of the Nitrogen Spectrum

The most frequently observed and reported electron spin resonance spectrum in natural, unirradiated diamond is that arising from substitutional nitrogen donors (7). The nitrogen spectrum is present in the diamonds containing the spectra under investigation in the present study. It is appropriate to describe the nitrogen spectrum in some detail in order to distinguish it from the spectra being studied.

In the diamond lattice each carbon atom is located at the center of a regular tetrahedron and is covalently bonded with its four nearest neighbors positioned at the vertices of the tetrahedron. The tetrahedral bonding arrangement of the diamond structure is depicted in Figure 7. When a nitrogen impurity atom replaces a carbon atom in the diamond lattice two of the seven electrons of the nitrogen are incorporated into the core states and four electrons participate in the normal covalent bonds, one with each of the four nearest neighbor carbon atoms. The unpaired spin of the "extra" or donor electron is responsible for the paramagnetism. According to Smith et al. (7), the donor electron is confined mainly to the substitutional nitrogen atom and one of the four nearest neighbor carbon atoms. Any of the four

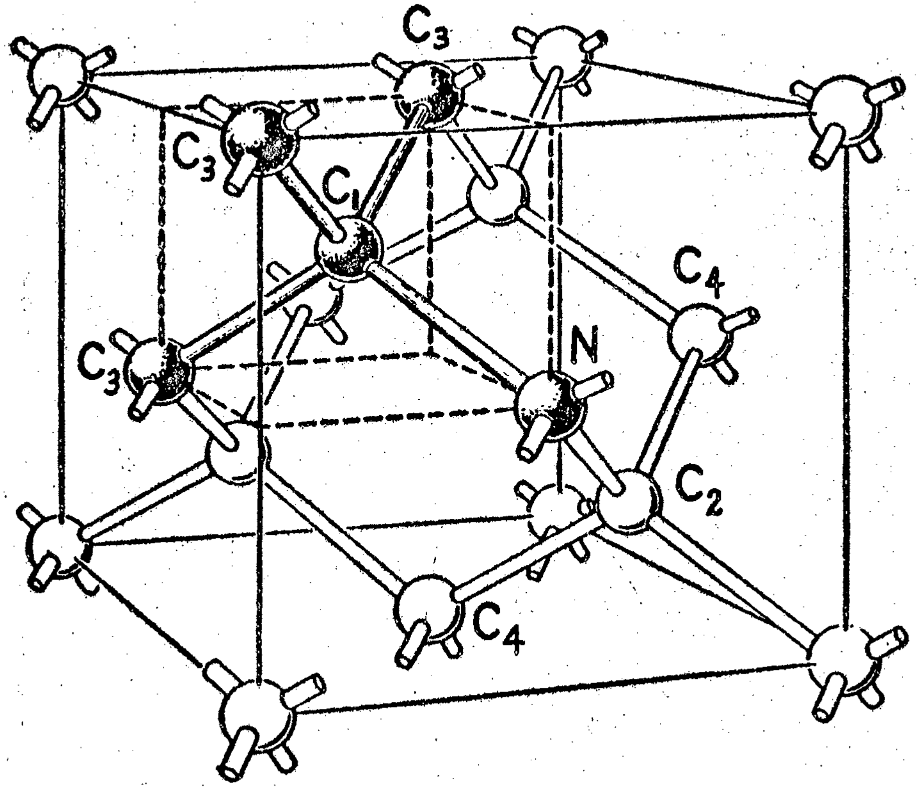

Figure 7. Tetrahedral Bonding Arrangement of the Diamond Structure.

nearest-neighbor carbon-nitrogen bond directions can serve as an axis for hyperfine interaction of the donor electron with the nitrogen nucleus whose spin is one. One possible hyperfine axis is the bond direction connecting the substitutional nitrogen N with the carbon atom C_1 in Figure 7. Since the nitrogen nucleus has spin $I=1$, it follows from the discussion of Chapter II that each site such as the N-C_1 site in Figure 7 will result in a spectrum with $2I+1$ or 3 equally intense lines. The possibility of 4 equally probable but differently oriented sites introduces additional structure. The spectrum from nitrogen donors is shown schematically in Figure 8. When the external magnetic field $\vec{H}$ is parallel to a $\langle 100\rangle$ direction of the diamond lattice all the bonds make an angle of $54^{\circ}40'$ with the field; that is, when $\vec{H}$ is along a $\langle 100\rangle$ direction all the possible hyperfine axes are inclined at the same angle relative to the magnetic field. For this case all the possible sites are equivalent and a simple spectrum of 3 equally intense lines results, and the outer lines are spaced equally relative to the central line. When $\vec{H}$ is in a $\langle 110\rangle$ direction half the bonds are perpendicular to the field and half are inclined at $35^{\circ}20'$, yielding two outer lines on either side of the central unshifted line. Each of the outer lines has half the intensity of the central line. When $\vec{H}$ is parallel to a $\langle 111\rangle$ direction of the crystal, one-fourth the bonds are parallel to the field and three-fourths are inclined at an angle of 70°. Consequently, the outer components exhibit an intensity ratio of 3 to 1, with the smaller one having an intensity one-fourth that of the main central component. For an arbitrary orientation of the diamond relative to the external magnetic field, a maximum of four equally intense components is

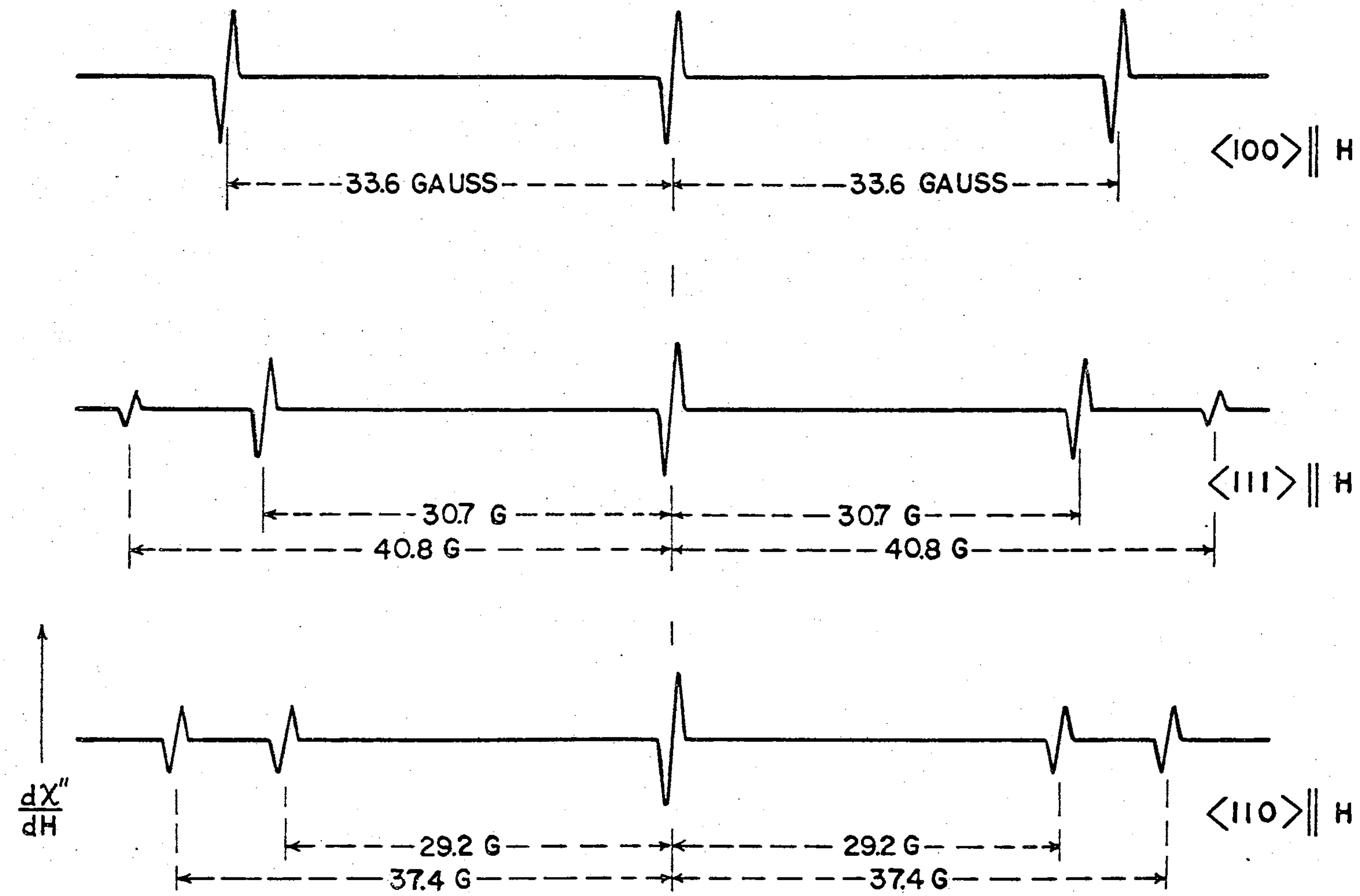

Figure 8. Schematic Representation of the Main ESR Spectrum from Substitutional Nitrogen Donors in Diamond.

observed on either side of the main central line. Since the g-factor is isotropic (g=2.0024$\pm$0.0005), the central component does not shift in position for various orientations of the diamond in the magnetic field.

Although C^{12} has no nuclear spin, there is a 1.1% natural abundance of C^{13} whose nuclear spin is ½. Interaction of the nitrogen donor electron with the C^{13} nuclear spin splits each of the main nitrogen lines into 2I+1 or 2 components. However, since only 1.1% of the sites designated C_1 in Figure 7 will be occupied by C^{13}, the resulting spectral lines will have only $\frac{1}{180}$ the intensity of the corresponding spectral lines in Figure 8. As Smith et al. (7) reported, only that portion of the weak C^{13} spectrum lying beyond the outer satellites of the main nitrogen spectrum in Figure 8 can be distinguished. Those portions of the C^{13} spectrum lying near the main nitrogen lines are rendered unresolvable because of their extremely small intensity.

Smith et al. (7) also observed pairs of weak lines symmetrically disposed about each main nitrogen absorption and separated from it by 6.4 Gauss. The lines were detected only with $\vec{H}$ along a $\langle 100 \rangle$ direction and were attributed to interaction of the donor electron with C^{13} in the position labeled C_2 in Figure 7. Since there are three C_2 positions for each C_1 position for a given site N, the pairs observed are 3 $(\frac{1}{180})$ or $\frac{1}{60}$ the intensity of the main nitrogen lines. Loubser and DuPreez (8) not only detected the weak pairs for $\vec{H}$ along a $\langle 100 \rangle$ direction but also with $\vec{H}$ parallel to $\langle 110 \rangle$ and $\langle 111 \rangle$. Figure 9 is an enlarged reproduction of the spectrum as shown by Loubser and DuPreez. The three large lines are the main nitrogen lines observed when $\vec{H}$ is parallel to a $\langle 100 \rangle$ direction. The outer components of the

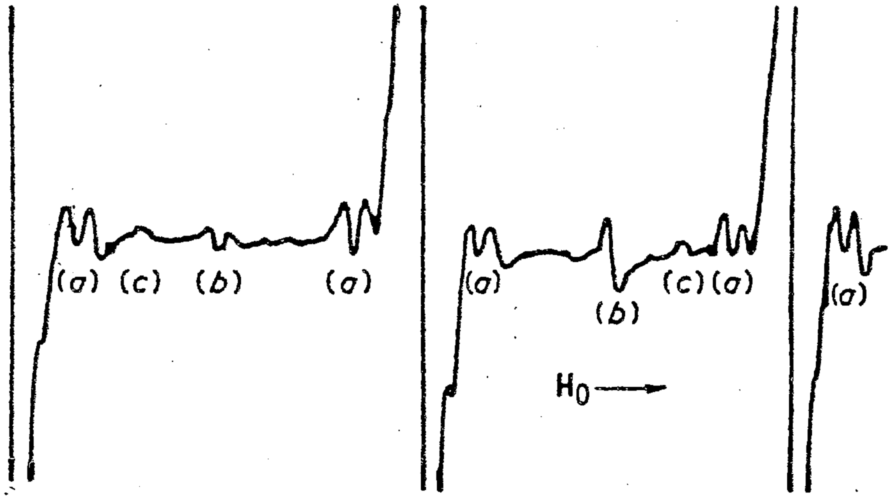

Figure 9. Additional Lines in the ESR Spectrum From Substitutional Nitrogen Donors in Diamond.

system labeled "(a)" in Figure 9 are separated from each main nitrogen line by 6.4 Gauss and were observed by Smith et al. (7). The inner components of the (a) system are separated from each main nitrogen line by 4.6 Gauss and were first observed by Loubser and Du Preez who attributed them to hyperfine interaction of the donor electron with the C^{13} nucleus in the position designated C_3 in Figure 7. The latter lines are isotropic and therefore do not split into more components when $\vec{H}$ is parallel to $\langle 110 \rangle$ or $\langle 111 \rangle$ directions.

The weak lines designated by (b) in Figure 9 occur approximately midway between the central and outer nitrogen lines. Loubser and Du Preez (8) explained their presence in terms of an interaction of the small nitrogen quadrupole moment with the electric field gradient. Finally, the feeble lines marked (c) in Figure 9 are separated from the central nitrogen line by 24.2 Gauss. Since only two lines were observed and their intensity was approximately $\frac{1}{200}$ that of the main nitrogen lines, Loubser and Du Preez associated them with interaction of the donor electron with the 0.365% naturally abundant isotope N^{15} whose nuclear spin is ½.

Other ESR Spectra in Natural Diamonds

It has long been known that complex ESR spectra in addition to that of the simple nitrogen spectrum of Figure 8 are present in natural diamonds. Smith et al. (9) reported a spectrum consisting of 14 lines for the case in which the external magnetic field was oriented along a $\langle 100 \rangle$ axis of the crystal. The system of lines is centered about the g value 2.0027 ± 0.0005, and the 14 nearly equally spaced components span a small magnetic field interval of approximately 25 Gauss.

Smith et al. (9) tentatively advanced the idea that the spectrum was associated with bound aluminum acceptors but later (7) indicated that the association was largely speculative.

In most diamonds containing ESR spectra other than that of nitrogen donors the additional spectra are of a very complex and anisotropic nature. Even with a ⟨100⟩ direction parallel to the magnetic field the additional spectra in some diamonds consist of thirty or more components spanning a field interval of only 25 Gauss. Diamond D-82 of our collection is representative of the highly complex spectra present in natural unirradiated diamonds. The ESR spectrum of D-82 is shown in Figure 10 for three orientations of the diamond relative to the external magnetic field. Upon comparison with Figure 8 it is seen that the number and relative intensities of the outer components in Figure 10 reveal that the nitrogen spectrum is present in D-82, although the additional complex spectra completely obscure the central isotropic nitrogen absorption. Complicated spectra such as that exhibited by D-82 presumably arise from the presence of more than one impurity resulting in a superposition of spectra near $g = 2.00$ which renders an analysis virtually impossible.

Experimentally Determined Nature of the Unusual ESR Spectrum

In a few natural diamonds the spectra in addition to the nitrogen spectrum are of a simpler nature than that of D-82 in Figure 10. The diamond specimens D-51A, D-51B, and D-58 of our collection exhibit the unusual electron spin resonance spectra under consideration in the present study. The spectra were recorded at room temperature with the

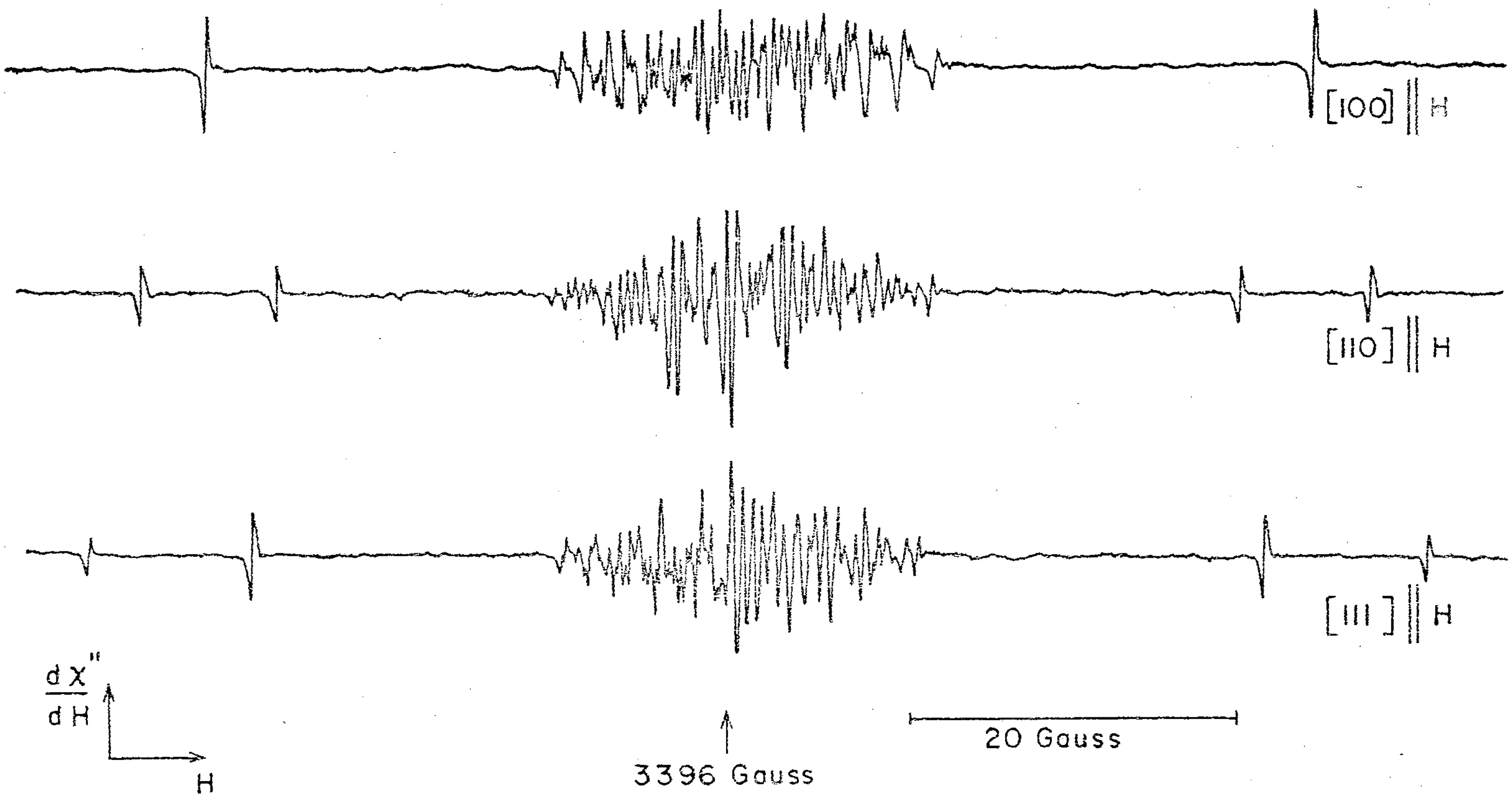

D-82 (Yellow Octahedron)

Figure 10. Electron Spin Resonance in Diamond D-82.

spectrometer shown in Figure 5 and discussed earlier. Each diamond was oriented by means of an x-ray back reflection technique (36) and attached to quartz tubes and positioned in the microwave cavity such that angular dependence studies of the spectra could be made with the external magnetic field $\vec{H}$ lying in a $\{110\}$ plane of the crystal. Angular variation studies were also made with $\vec{H}$ lying in a $\{100\}$ and $\{111\}$ crystalline plane. However, the angular behavior of the spectra with $\vec{H}$ rotated in a $\{110\}$ plane is perhaps the most revealing because $\vec{H}$ can be aligned parallel to each of the three major crystalline directions $\langle 100\rangle$, $\langle 110\rangle$, and $\langle 111\rangle$.

Magnetic field values were determined with the aid of a nuclear resonance probe, and DPPH ($g = 2.0036 \pm 0.0003$) was employed as a standard g-value indicator. In using a standard g-value reference it is desirable that the resonance line of the standard be recorded simultaneously with the spectrum under investigation and that the standard be positioned very near the sample to assure that both the sample and the standard are exposed to the same magnetic field strength. To this end, a 0.025" diameter recess was drilled to an approximate depth of 0.028" in a small piece of teflon. After tamping a small quantity of powdered DPPH into the recess the excess teflon was carefully carved away to produce a small teflon capsule approximately 0.03" on a side containing the DPPH standard. Ordinary Duco cement contains no ESR signal to interfere with that of the diamond and was used not only in attaching the diamond to the quartz tube but also in securing the small teflon capsule to a face of the diamond.

In determining g values the standard resonance line was recorded simultaneously with the spectrum of the diamond. If H_{DPPH} and $H_{Dia.}$

are the magnetic field values of the DPPH resonance and a particular line in the diamond spectrum, respectively, and g_{DPPH} and $g_{Dia.}$ are the corresponding g values, equation (2-14) yields the relationship

$$h\nu = g_{DPPH}\beta H_{DPPH} = g_{Dia.}\beta H_{Dia.} \qquad (4\text{-}1a)$$

or
$$g_{Dia.} = g_{DPPH}\frac{H_{DPPH}}{H_{Dia.}} \quad .$$

That is, the standard resonance is observed at the same frequency as the diamond spectrum. The magnetic field values H_{DPPH} and $H_{Dia.}$ were determined with the aid of the nuclear resonance probe. Since the probe is necessarily external to the microwave cavity and slightly off the central axis, the magnetic field as determined by the probe usually differs by a few tenths of one Gauss from the field at the position of the diamond and DPPH standard. To account for this a correction factor was determined by comparing the measured field H_{DPPH} with the correct field calculated from

$$H_{DPPH}^{Corr.} = \frac{h\nu}{g_{DPPH}\beta} \quad . \qquad (4\text{-}1b)$$

The correction factor was then used to obtain the correct field $H_{Dia}^{Corr.}$. Using the corrected values for H_{DPPH} and $H_{Dia.}$, the value of $g_{Dia.}$ was computed from the relation in equation (4-1a). The microwave frequency ν in equation (4-1b) was measured with the aid of the Hewlett-Packard model 540B transfer oscillator used in conjunction with the model 524D electronic counter.

Figure 11 shows the complete spectra of D-51A and D-51B with ⟨100⟩, ⟨111⟩, and ⟨110⟩ parallel to the magnetic field. Reference to Figure 8 reveals that the outermost lines on the high and

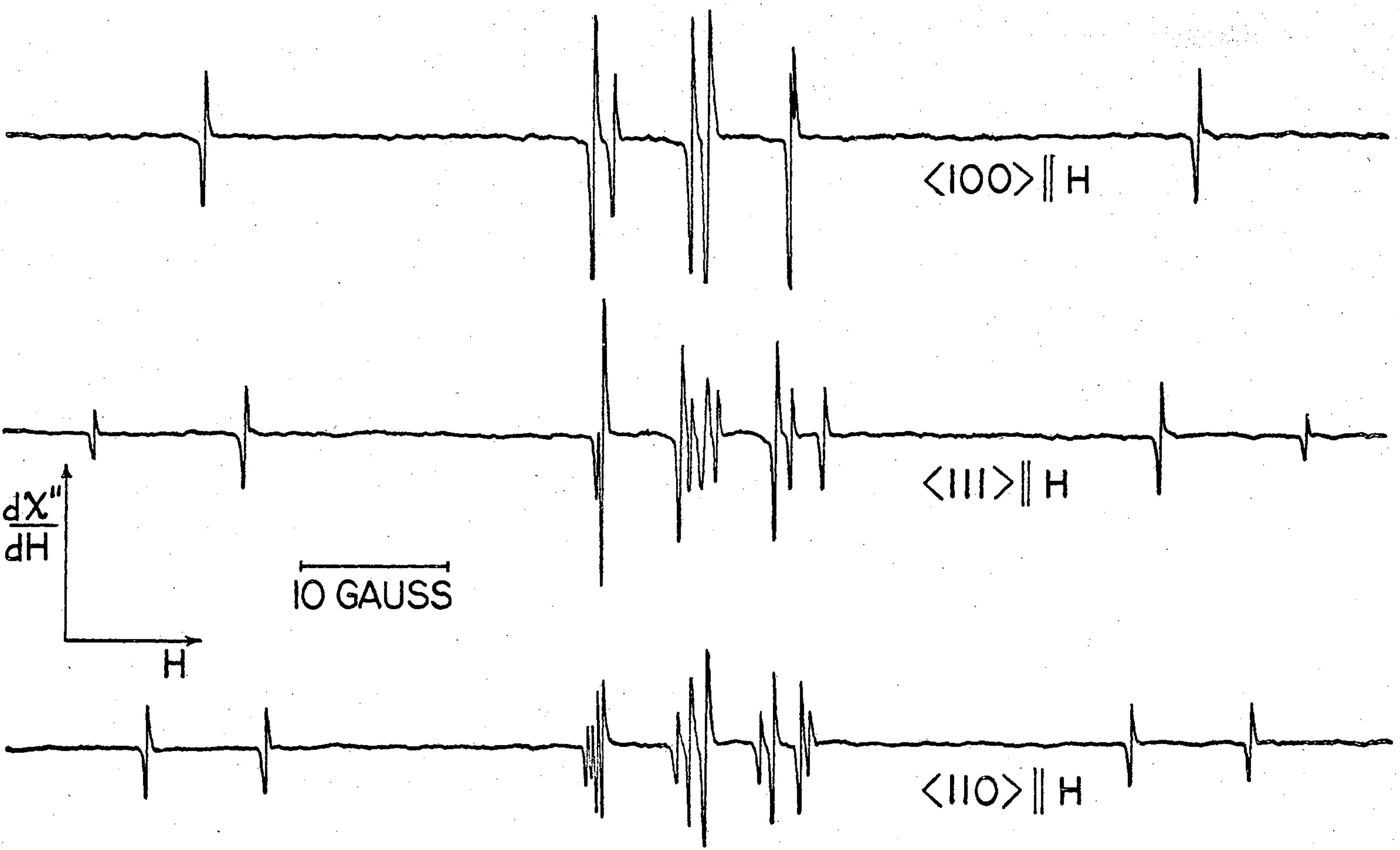

Figure 11. Electron Spin Resonance in Diamonds D-51A and D-51B.

low field sides in Figure 11 are the hyperfine lines in the normal nitrogen spectrum. All lines of the unusual spectra have a very narrow linewidth of approximately 0.17 Gauss, which is considerably less than that of the main nitrogen lines. A slow scan of the central family of lines is shown in Figure 12, in which it can be seen that there are three main groups of lines. The high field group consists of two very closely spaced components with the magnetic field in a $\langle 100 \rangle$ direction. There are 3 lines with relative intensities 6:3:3 in a $\langle 111 \rangle$ direction, and 4 with intensities 2:4:4:2 when $\vec{H}$ is parallel to $\langle 110 \rangle$.

The low field group is comprised of 2 lines of relative intensity 8:4 for $\vec{H} /\!/ \langle 100 \rangle$, 2 lines in the approximate ratio 3:9 with $\vec{H} /\!/ \langle 111 \rangle$, and 4 lines of intensity ratio 2:2:4:4 when $\vec{H}$ is in a $\langle 110 \rangle$ direction.

Finally, in Figure 12 the middle field group is seen to contain 3 lines of relative intensity 6:3:3 with $\vec{H} /\!/ \langle 111 \rangle$, and the central isotropic nitrogen line occurs between the two lower intensity lines. When $\vec{H}$ is along $\langle 100 \rangle$ a single line of intensity 8 units occurs at a slightly lower field than the middle nitrogen line. In a $\langle 110 \rangle$ direction two lines with relative intensity 2:4 appear on the low field side but near the middle nitrogen line. In $\langle 100 \rangle$ and $\langle 110 \rangle$ directions the lines at the central nitrogen position appear greater in intensity than the central nitrogen line with $\vec{H}$ along a $\langle 111 \rangle$ direction. This aspect is associated with the presence of the middle group of lines, and its significance will be discussed later.

Figure 13 shows the complete spectra of D-58 with the magnetic field parallel to a $\langle 100 \rangle$, $\langle 110 \rangle$, and $\langle 111 \rangle$ direction. The number and relative intensities of the outermost lines on the high

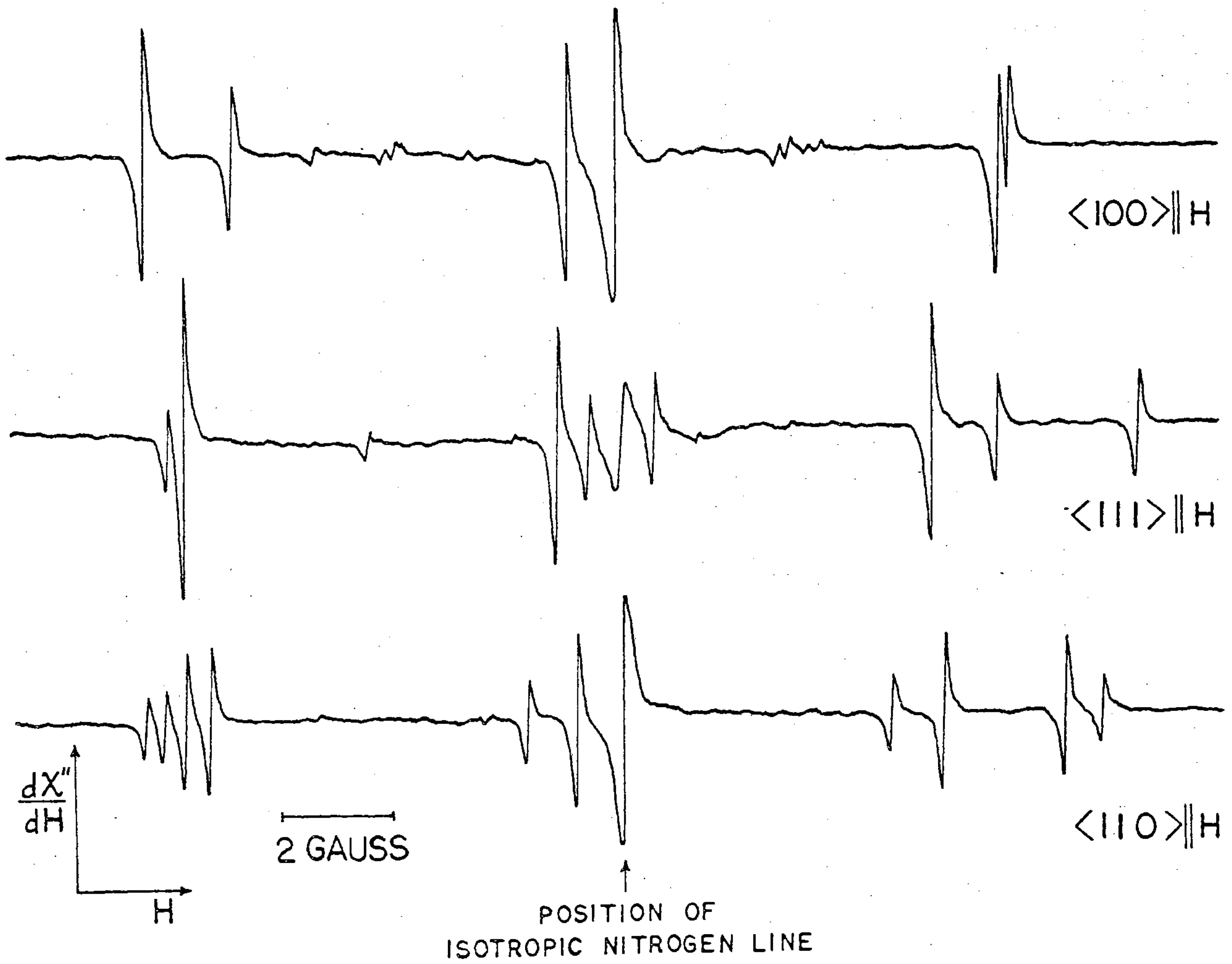

Figure 12. Slow Scan of the Unusual Electron Spin Resonance Spectra in Diamonds D-51A and D-51B.

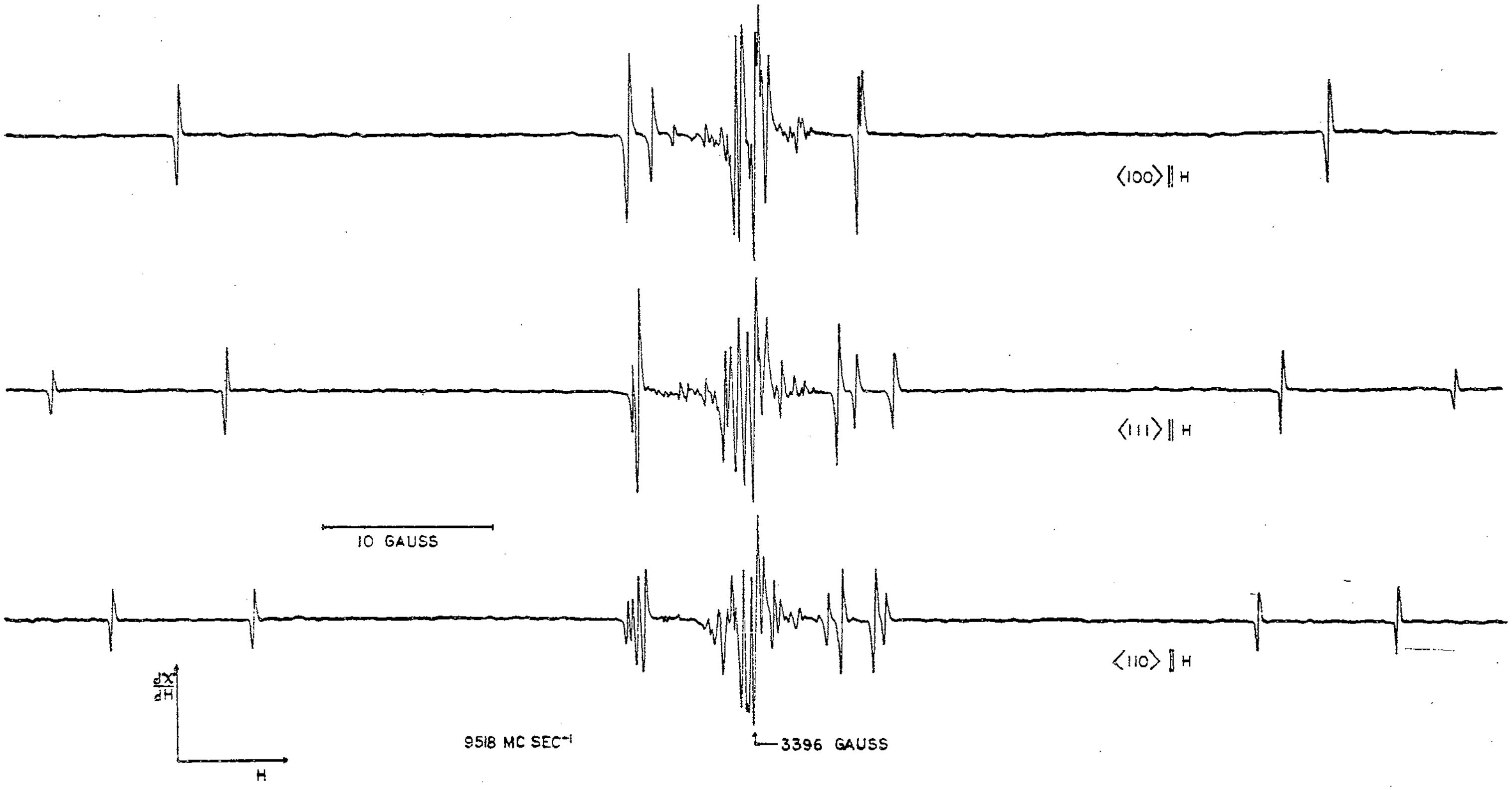

Figure 13. Electron Spin Resonance in Diamond D-58.

and low field extremities indicate that the spectrum from substitutional nitrogen donors is present in the diamond D-58. However, the additional complex spectral lines exhibited by D-58 completely mask the central isotropic nitrogen line. A slow scan of the central region of the D-58 spectrum is shown in Figure 14; it can be seen that the outer groups of lines on the high and low field sides of the complex portion are identical in number and corresponding relative intensities to the outer groups of D-51A and D-51B in Figure 12. However, the additional complex structure of D-58 obscures the middle group of lines possessed by D-51A and D-51B.

The experimentally observed angular dependencies of the unusual spectra of D-51A and D-51B when H is rotated in a $\{110\}$ crystalline plane are shown on the left in Figures 15, 16, and 17. The outer groups of lines in the D-58 spectrum of Figure 14 have the same angular dependence in a $\{110\}$ plane as that of D-51A and D-51B shown in Figures 15 and 17. For arbitrary angle θ, the high field group in Figure 15 splits into a maximum of 7 lines with relative intensities 2:2:2:2:1:2:1. The middle field group in Figure 16 exhibits a maximum of 6 lines except for a partial splitting of one near $\theta = 68^\circ$. Finally, at arbitrary angle θ, 6 lines with intensity ratios 2:4:2:1:2:1 characterize the angular behavior of the low field group in Figure 17.

When the magnetic field is rotated in a $\{100\}$ plane of the diamond each of the groups splits into as many as 6 lines as shown on the left in Figures 18, 19, and 20.

The observed angular behavior of the high field group when $\vec{H}$ is rotated in a $\{111\}$ plane is shown on the left in Figure 21. As many as 11 lines are observed, 10 of unit intensity and 1 of double

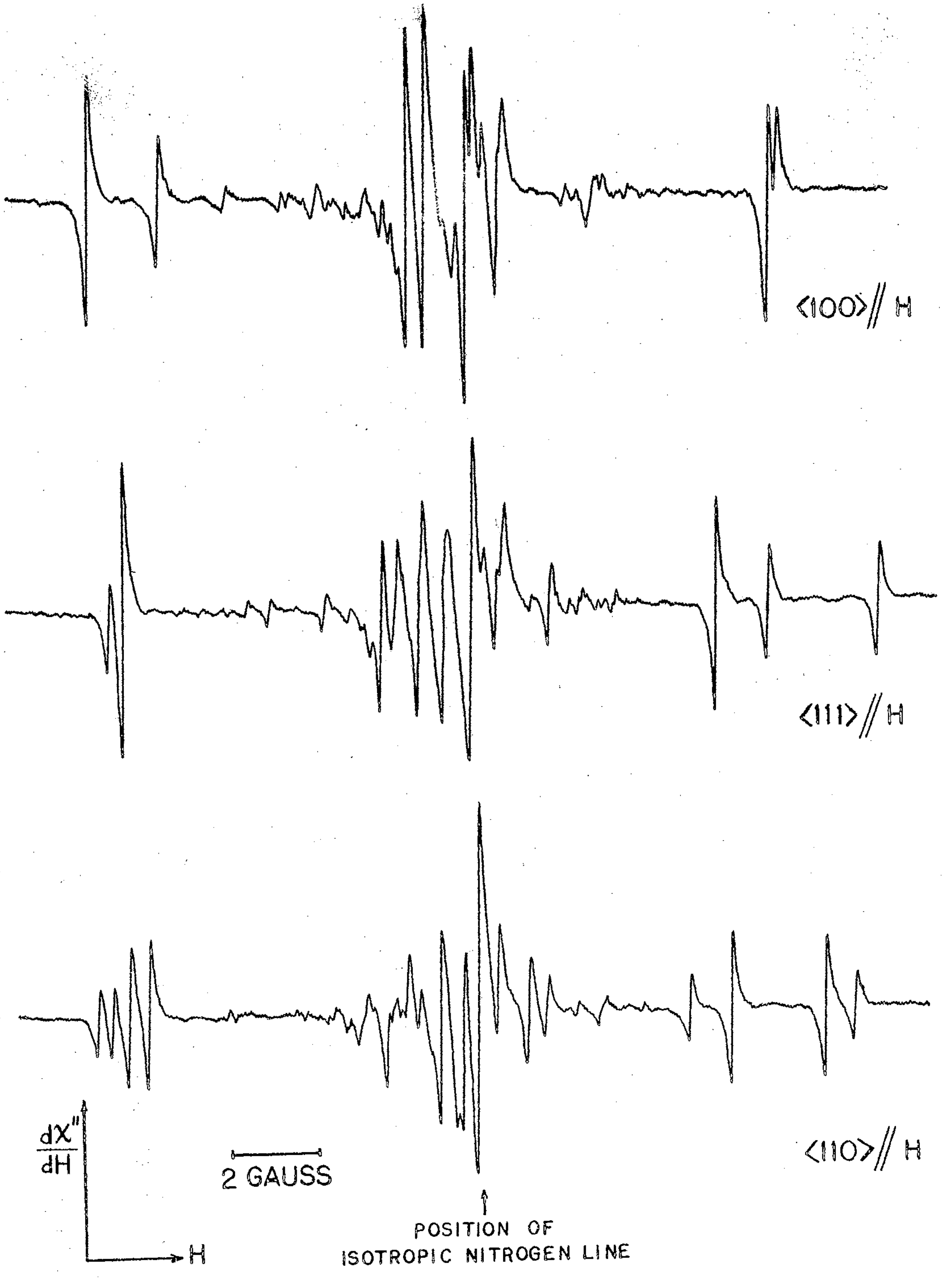

Figure 14. Slow Scan of the Unusual Electron Spin Resonance Spectra in Diamond D-58.

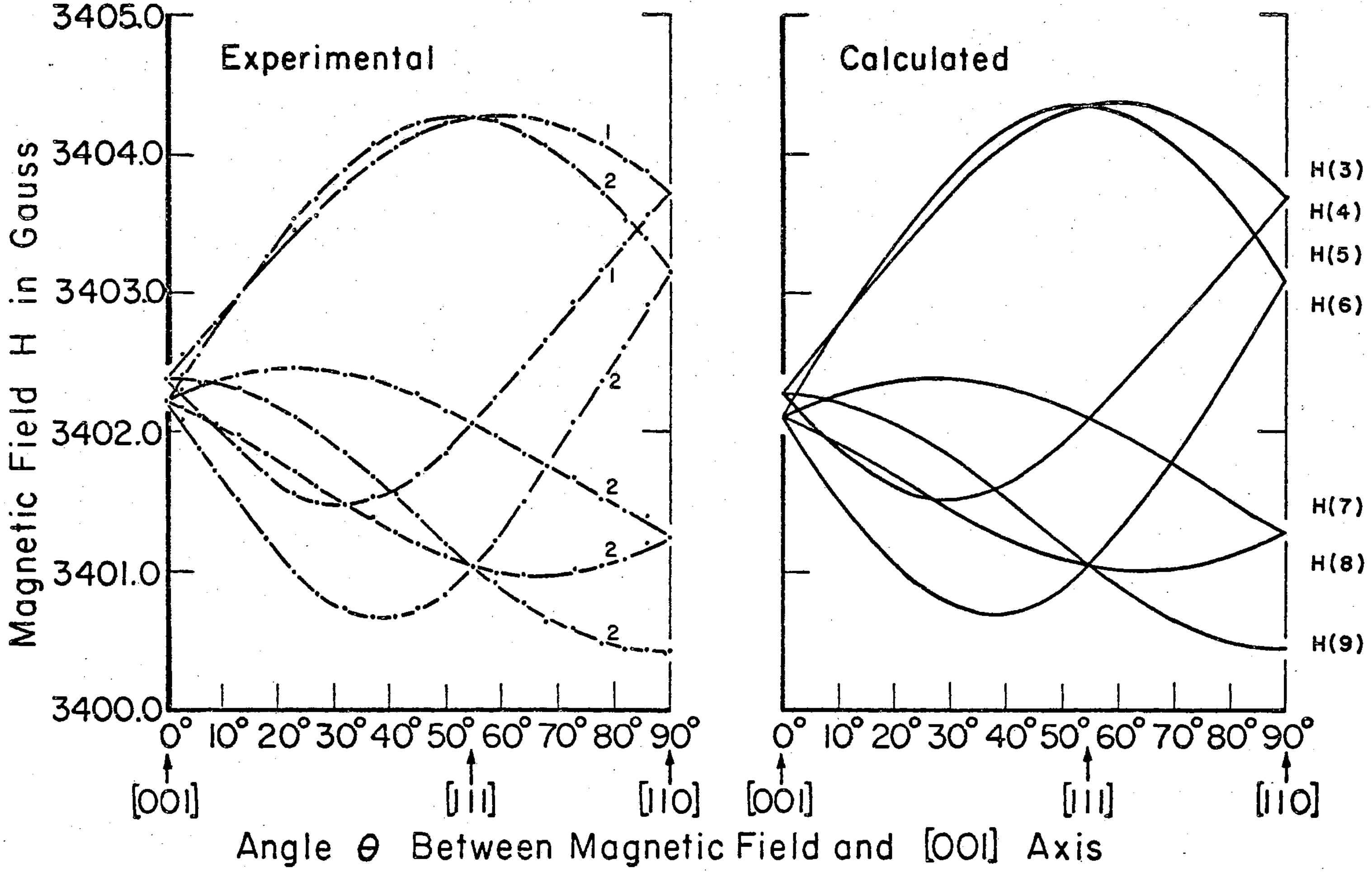

Figure 15. Experimental and Theoretical Angular Dependence of the High Field Group of Lines when the Magnetic Field H is Rotated in a {110} Plane of the Diamond.

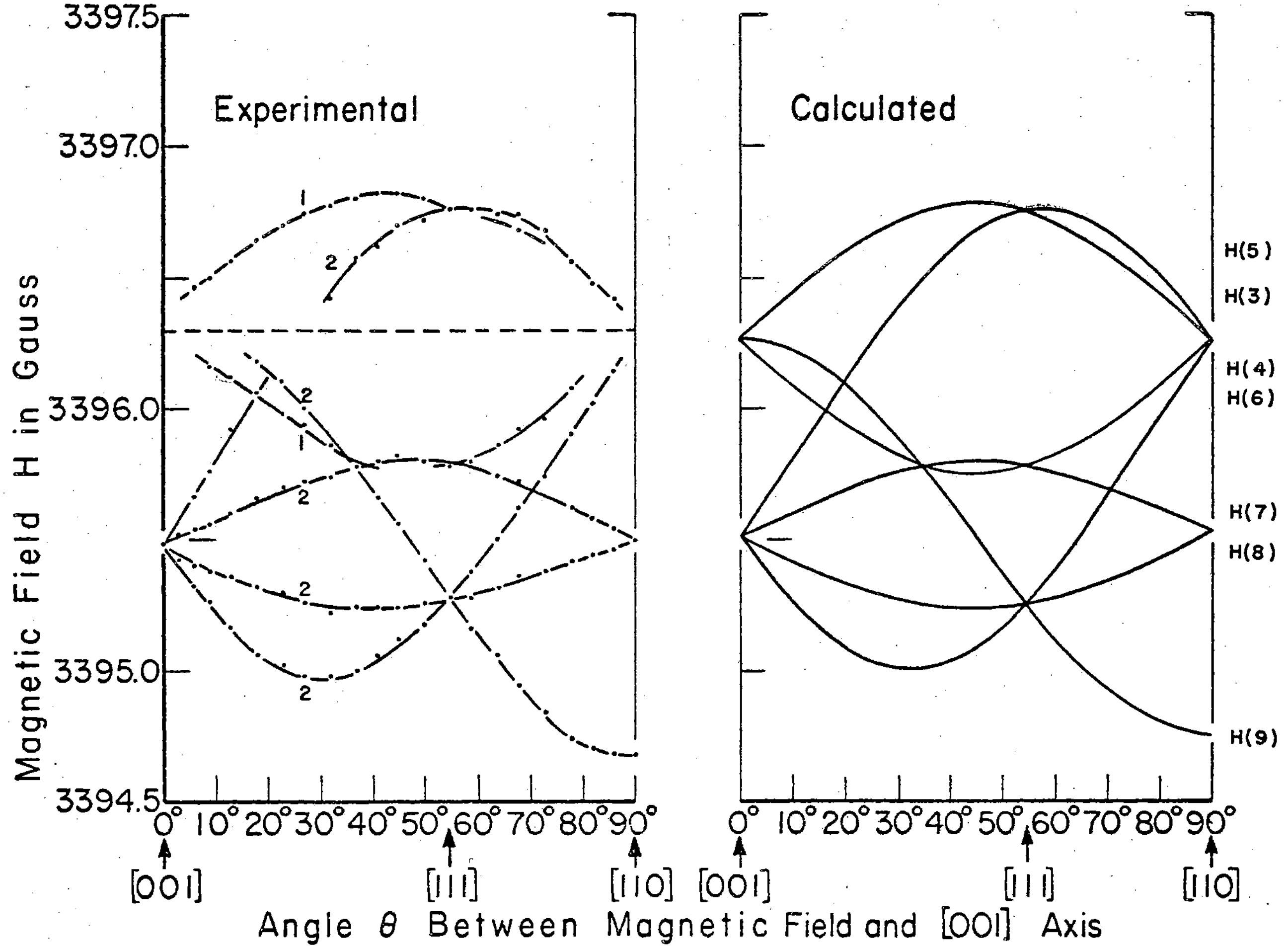

Figure 16. Experimental and Theoretical Angular Dependence of the Middle Field Group of Lines when the Magnetic Field is Rotated in a $\{110\}$ Plane of the Diamond.

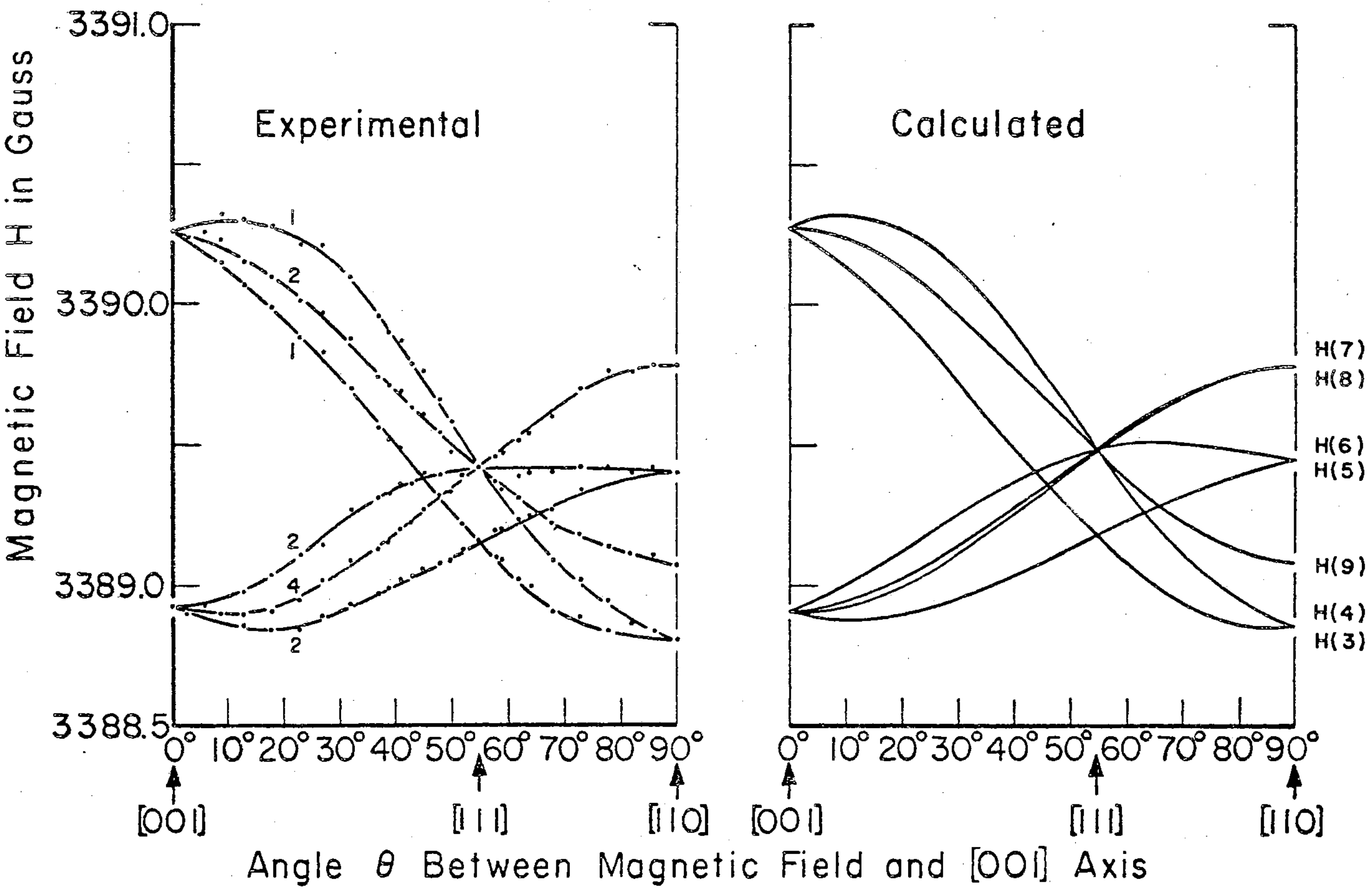

Figure 17. Experimental and Theoretical Angular Dependence of the Low Field Group of Lines when the Magnetic Field is Rotated in a $\{110\}$ Plane of the Diamond.

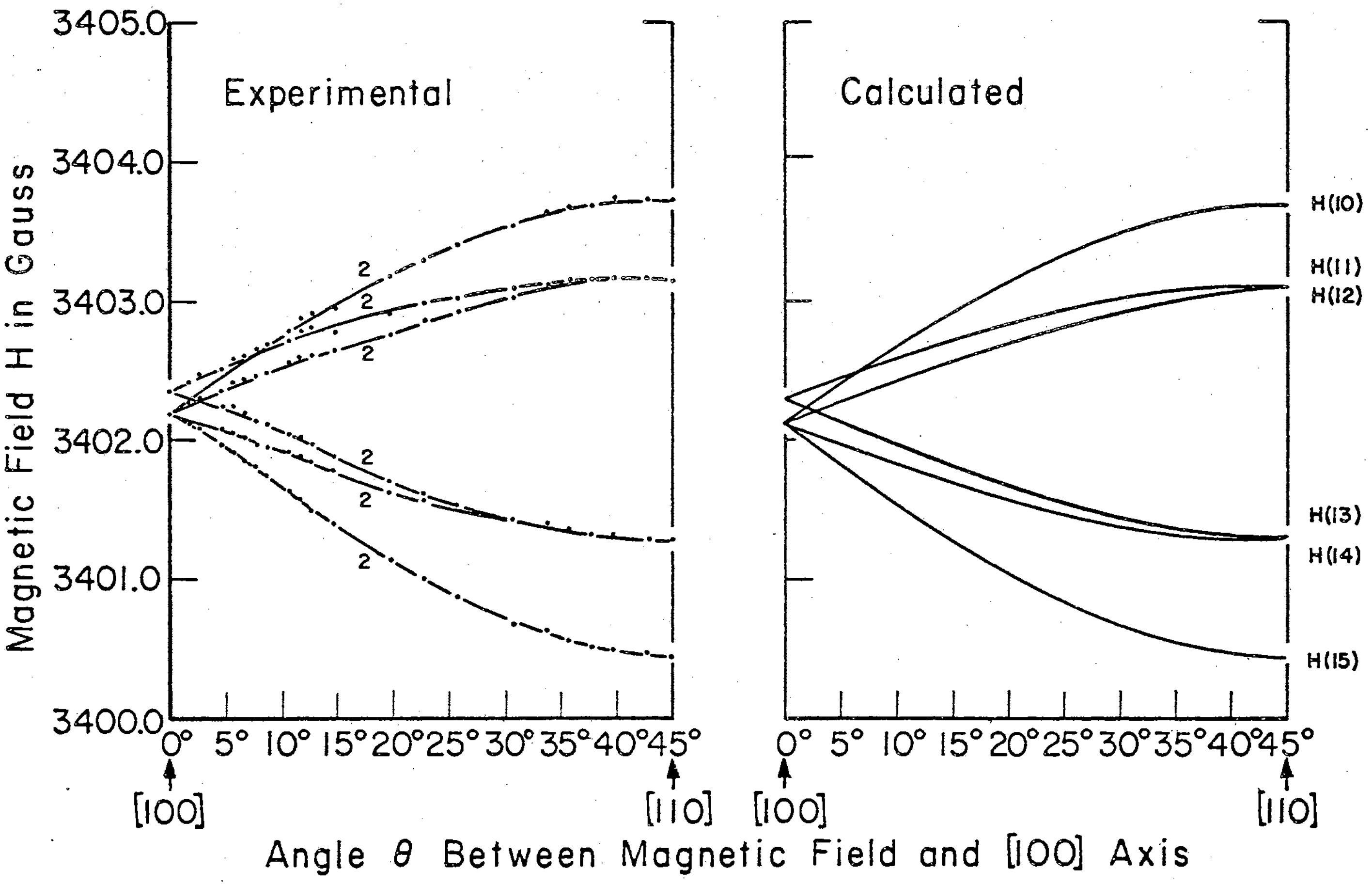

Figure 18. Experimental and Theoretical Angular Dependence of the High Field Group of Lines when the Magnetic Field is Rotated in a {100} Plane of the Diamond.

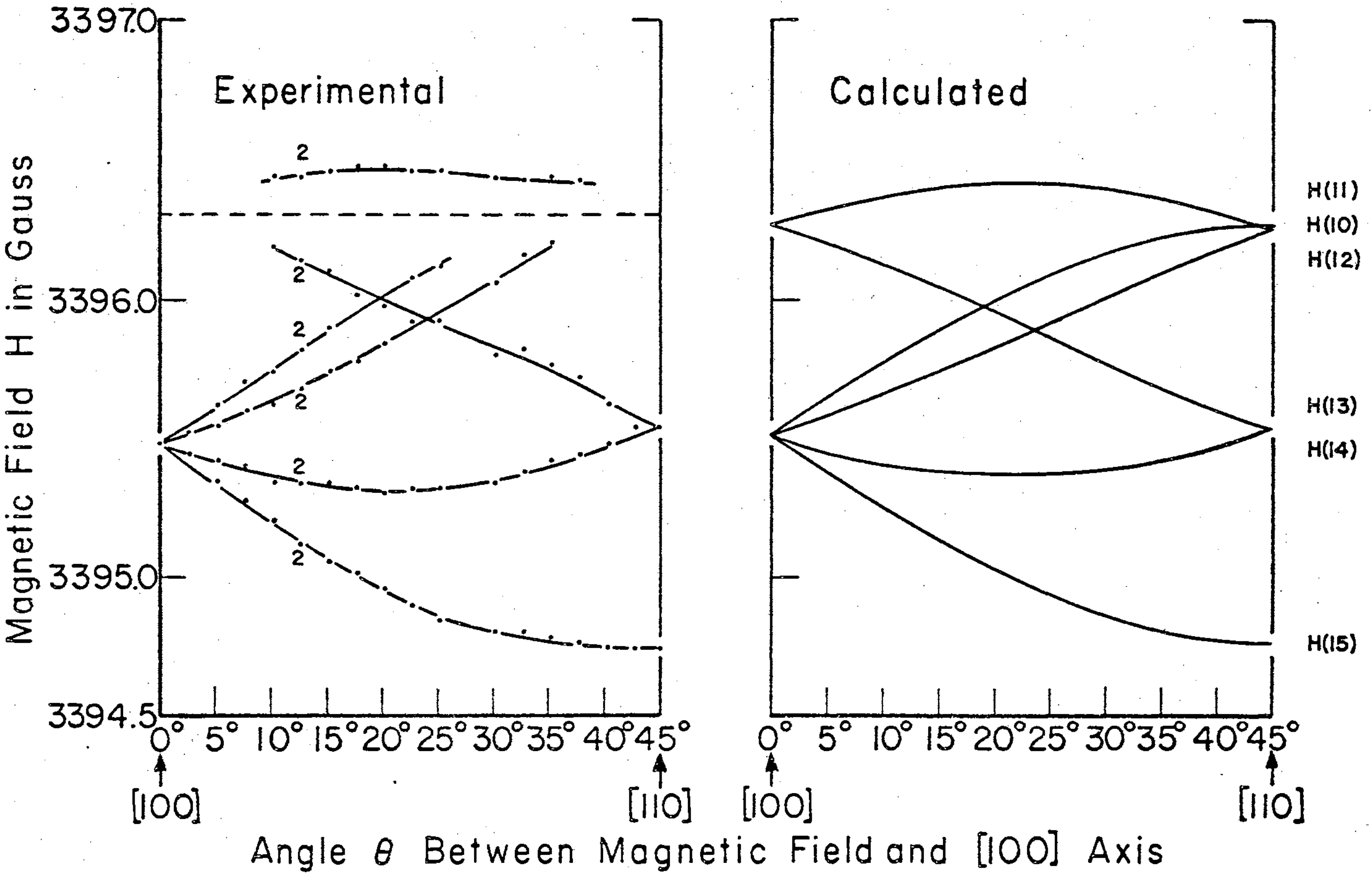

Figure 19. Experimental and Theoretical Angular Dependence of the Middle Field Group of Lines when the Magnetic Field is Rotated in a {100} Plane of the Diamond.

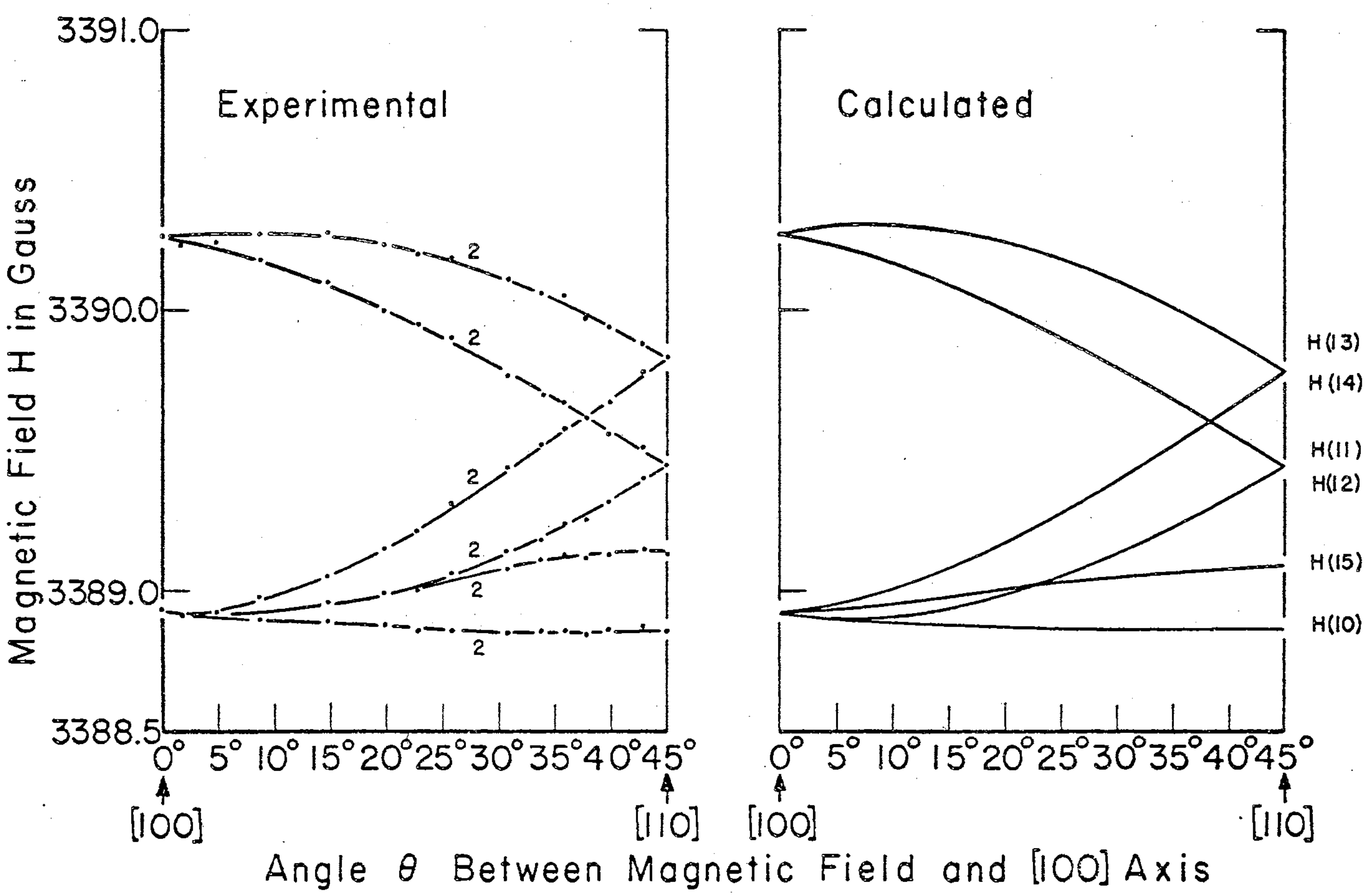

Figure 20. Experimental and Theoretical Angular Dependence of the Low Field Group of Lines when the Magnetic Field is Rotated in a {100} Plane of the Diamond.

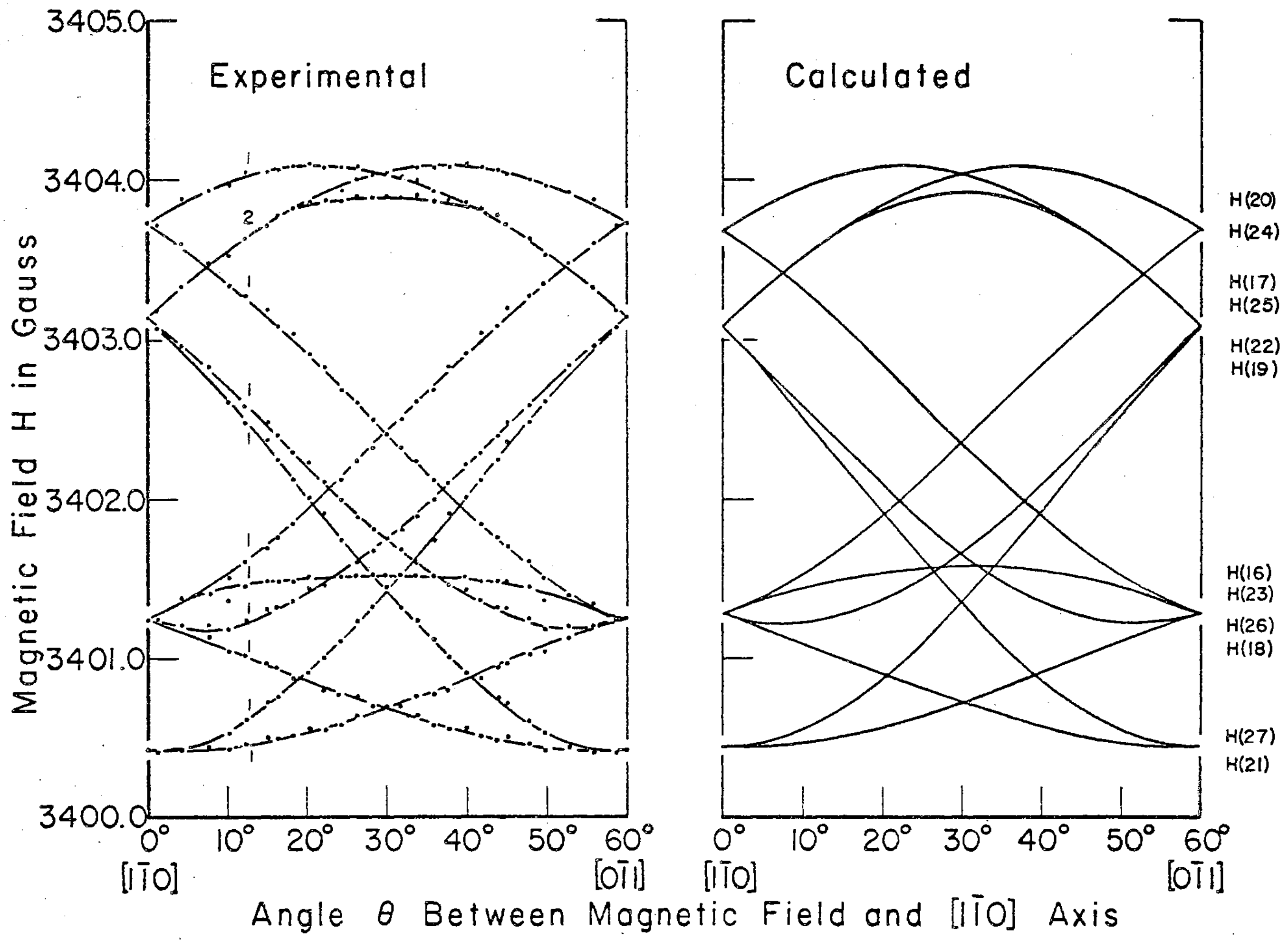

Figure 21. Experimental and Theoretical Angular Dependence of the High Field Group of Lines when the Magnetic Field is Rotated in a {111} Plane of the Diamond.

intensity. Only the results for the high field group are shown because not all the lines in the middle and low field groups could be resolved with $\vec{H}$ in a $\{111\}$ plane. The lack of resolution of all the lines can be understood by noting that the total splitting of the low field group for $\vec{H} // \langle 110 \rangle$ is less than 1 Gauss, or less than one-third that of the high field group. Complete resolution is impossible for the middle field group not only because the $\langle 110 \rangle$ splitting is less than half that of the high field lines but also the central nitrogen line obscures a large portion of the detail in a $\{111\}$ plane.

In King's (37) study of the effect of light on ESR in diamonds, the spectra of D-51A, D-51B, and D-58 were found to be insensitive to irradiation with ultra violet light. In comparing other experimental characteristics of the three diamonds with the remaining samples of our collection, no prominent features in the optical absorption spectra, for example, are present which would distinguish the diamonds from those in which the unusual ESR is unobservable. Neither does any correlation exist regarding the photoconductive or photovoltaic responses (38). However, it is interesting to note that the diamonds containing the unusual ESR also exhibit strong luminescence properties compared with other diamonds in the collection (38).

The Spin Hamiltonian and the Calculated Results

Corresponding lines in the three groups are of equal intensity, and the lines in the high and low field groups are separated approximately equally on either side of their corresponding lines in the middle group. Therefore, it was first assumed and later confirmed that the three groups of lines considered as a whole arise from hyperfine interaction of an unpaired electron with a nucleus of spin one. The spin-one nucleus is believed to be nitrogen for the following reasons. Only H_2, Li, Cu^{64}, and Cs^{130} in addition to nitrogen have a nuclear spin of 1. The radioactive isotopes Cu^{64} and Cs^{130} have half-lives of only 12.8 hr. and 30 min., respectively, and therefore have to be excluded. Lithium has been tested for but not found in natural diamonds (39). Using a gas analysis technique Kaiser and Bond (40) found large concentrations of nitrogen but only small quantities of hydrogen present in natural Type I diamonds. The spin-one isotope of hydrogen has a natural abundance of only 0.0156% and therefore can be ruled out. Since nitrogen is known to be a major impurity in natural diamonds it is believed that the nitrogen nucleus of spin one is responsible for the 2I+1 or 3 groups of lines in the unusual ESR spectra.

The spin Hamiltonian will be of the form

$$\mathcal{H} = \beta \bar{g}\cdot\bar{S}\cdot\bar{H} + \bar{A}\cdot\bar{I}\cdot\bar{S} \tag{4-1c}$$

with $s = \frac{1}{2}$ and $I = 1$. The anisotropic nature of the unusual spectrum suggests that $\bar{g}$ and $\bar{A}$ are anisotropic tensors whose principal axes are not coincident. The allowed ESR transitions $(\Delta m_S = \pm 1,\ \Delta m_I = 0)$ given by equation (2-38) are

$$h\nu = g\beta H + m_I A + \frac{A^2}{2g\beta H}\left[I(I+1) - m_I^2\right] \tag{4-1d}$$

$$g^2 = g_1^2\cos^2\phi_1 + g_2^2\cos^2\phi_2 + g_3^2\cos^2\phi_3 \tag{4-1e}$$

$$A^2 = A_1^2\cos^2\Phi_1 + A_2^2\cos^2\Phi_2 + A_3^2\cos^2\Phi_3 \tag{4-1f}$$

The ϕ_i and Φ_i are the angles between the principal components of $\bar{g}$ and $\bar{A}$, respectively, and the external magnetic field $\vec{H}$. It was pointed out in Chapter II that the expression in equation (4-1d) obtained from the Breit-Rabi relation of equation (2-34) neglects the anisotropy in $\bar{g}$. However, use of equation (4-1d) is entirely justifiable in the present case since, as will be seen later, the maximum anisotropy in $\bar{g}$ is only 0.06% of the average magnitude of g itself. Equation (4-1d) can be expressed explicitly in terms of the magnetic field to yield

$$H = \frac{1}{2g\beta}\left[(h\nu - m_I A) + \sqrt{(h\nu - m_I A)^2 - 2A^2\left[I(I+1) - m_I^2\right]}\right]. \quad (4\text{-}2)$$

The anisotropic features of the spectrum can be explained on the basis of a model in which identical defect centers are present whose axes are oriented differently in the diamond lattice. In fact, the proper number of spectral lines, their relative intensities, and the angular behaviors in the major crystalline planes are properly predicted if the principal components g_1 and A_1 are oriented along each of the twelve $\langle 110 \rangle$ directions. For example, defect sites with g_1 in the $[110]$ direction have g_2 and g_3 in the (110) plane, and g_2 makes an angle ψ with the $[\bar{1}10]$ axis, as shown in Figure 22. For these sites, A_1 also is in the $[110]$ direction and A_2 and A_3 are in the (110) plane, but A_2 is inclined at an angle α with the $[\bar{1}10]$ axis.

In Figure 22 the magnetic field $\vec{H}$ is in the (110) plane and makes an angle θ with the $[001]$ axis. When cos φ_1 , cos φ_2 , and cos φ_3 in equation (4-1e) are expressed in terms of θ and ψ , equation (4-9) is obtained. Similar calculations for the centers having

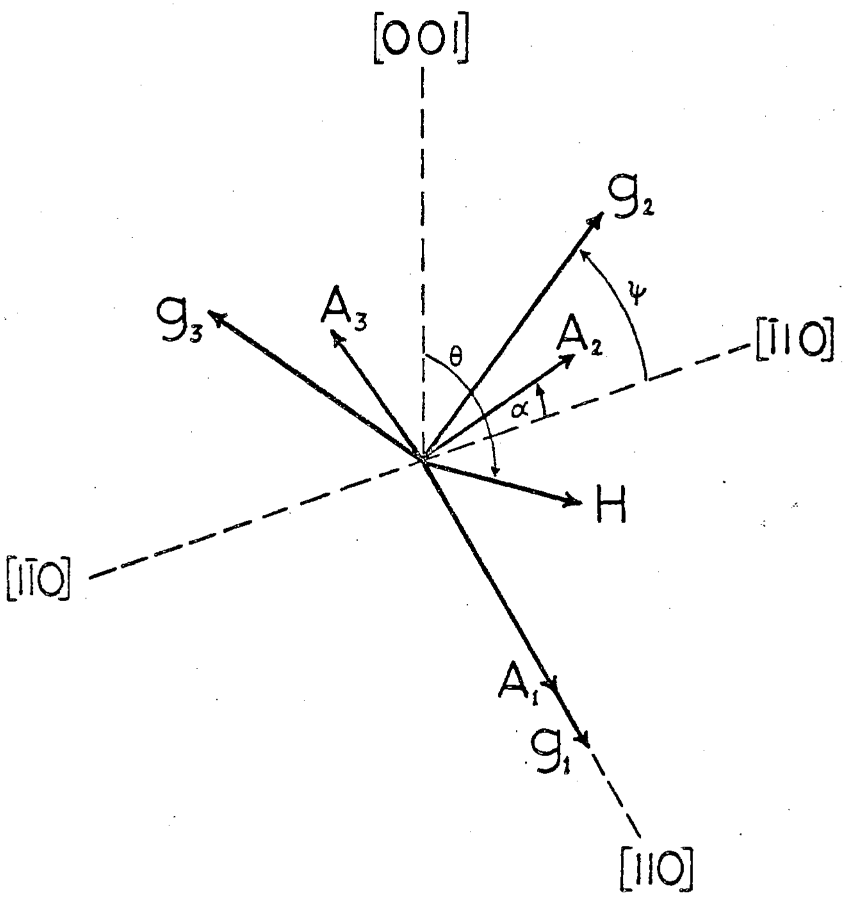

Figure 22. A Possible Defect Orientation which Has its Principal Components g_1 and A_1 in the [110] Direction.

their components g_1 lying in the remaining $\langle 110 \rangle$ directions yield equations (4-3) through (4-8). Note that ten of the centers become equivalent in pairs when $\vec{H}$ is in a $\{110\}$ plane, so only seven independent expressions are obtained for g. The expressions for A are the same in form as those for g, except that g_1, g_2, g_3, and ψ are replaced by A_1, A_2, A_3, and α, respectively. A sample derivation of equations (4-3) through (4-9) is given in the Appendix.

When the seven expressions for g in equations (4-3) through (4-9) and the corresponding ones for A are substituted into equation (4-2), the calculated magnetic field values in the (110) plane for the high, middle, and low field hyperfine groups are obtained by setting $m_I = -1$, 0, and 1, respectively. Preliminary values for g_1, g_2, g_3, and ψ were determined by noting that equation (4-1d) is independent of A for the middle hyperfine group ($m_I = 0$) provided the second order term is neglected. Using equation (4-1d) under this approximation and noting that equation (4-9) reduces to $g = g_1$ for $\theta = 90^\circ$, a preliminary value for g_1 was deduced from the corresponding spectral line of the middle group in the experimental data with $\vec{H}$ parallel to a $\langle 110 \rangle$ direction. When the angle θ between $\vec{H}$ and the $[001]$ axis is equal to the angle ψ, the expression for g in equation (4-4) exhibits an extremum and yields the value $g = g_3$. Therefore, by observing the angle θ at which the corresponding experimental curve in Figure 16 has a tangent line with zero slope, the angle ψ was determined directly; the experimental value of g at which the curve exhibits zero slope provided a preliminary value for g_3. Similarly, it is seen that the expression for g in equation (4-3) has the extremal value $g = g_2$ when θ is equal to $90^\circ - \psi$; by observing the value of g at which the

$g_1 : [1\bar{1}0]$

$$g = \left\{ g_2^2 \sin^2(\psi+\theta) + g_3^2 \cos^2(\psi+\theta) \right\}^{\frac{1}{2}} \tag{4-3}$$

$g_1 : [\bar{1}10]$

$$g = \left\{ g_2^2 \sin^2(\psi-\theta) + g_3^2 \cos^2(\psi-\theta) \right\}^{\frac{1}{2}} \tag{4-4}$$

$g_1 : [\bar{1}01], [01\bar{1}]$

$$g = \left\{ g_1^2 \left[\frac{\cos\theta}{\sqrt{2}} - \frac{\sin\theta}{2} \right]^2 + \frac{1}{4} g_2^2 \left[-\sin\theta\cos\psi - \sqrt{2}(\sin\theta\sin\psi + \cos\theta\cos\psi) \right]^2 + \frac{1}{4} g_3^2 \left[\sin\theta\sin\psi - \sqrt{2}(\sin\theta\cos\psi - \cos\theta\sin\psi) \right]^2 \right\}^{\frac{1}{2}} \tag{4-5}$$

$g_1 : [101], [0\bar{1}\bar{1}]$

$$g = \left\{ g_1^2 \left[\frac{\cos\theta}{\sqrt{2}} + \frac{\sin\theta}{2} \right]^2 + \frac{1}{4} g_2^2 \left[-\sin\theta\cos\psi - \sqrt{2}(\sin\theta\sin\psi - \cos\theta\cos\psi) \right]^2 + \frac{1}{4} g_3^2 \left[\sin\theta\sin\psi - \sqrt{2}(\sin\theta\cos\psi + \cos\theta\sin\psi) \right]^2 \right\}^{\frac{1}{2}} \tag{4-6}$$

$g_1 : [10\bar{1}], [0\bar{1}1]$

$$g = \left\{ g_1^2 \left[\frac{\cos\theta}{\sqrt{2}} - \frac{\sin\theta}{2} \right]^2 + \frac{1}{4} g_2^2 \left[\sin\theta\cos\psi - \sqrt{2}(\sin\theta\sin\psi - \cos\theta\cos\psi) \right]^2 + \frac{1}{4} g_3^2 \left[-\sin\theta\sin\psi - \sqrt{2}(\sin\theta\cos\psi + \cos\theta\sin\psi) \right]^2 \right\}^{\frac{1}{2}} \tag{4-7}$$

$g_1 : [\bar{1}0\bar{1}], [011]$

$$g = \left\{ g_1^2 \left[\frac{\cos\theta}{\sqrt{2}} + \frac{\sin\theta}{2} \right]^2 + \frac{1}{4} g_2^2 \left[\sin\theta\cos\psi - \sqrt{2}(\sin\theta\sin\psi + \cos\theta\cos\psi) \right]^2 + \frac{1}{4} g_3^2 \left[-\sin\theta\sin\psi - \sqrt{2}(\sin\theta\cos\psi - \cos\theta\sin\psi) \right]^2 \right\}^{\frac{1}{2}} \tag{4-8}$$

$g_1 : [110], [\bar{1}\bar{1}0]$

$$g = \left\{ g_1^2 \sin^2\theta + \cos^2\theta \left(g_2^2 \sin^2\psi + g_3^2 \cos^2\psi \right) \right\}^{\frac{1}{2}} \tag{4-9}$$

corresponding experimental curve in Figure 16 exhibits zero slope, a preliminary value for g_2 was determined. Finally, using the preliminary parameters of the $\bar{g}$-tensor and taking advantage of the fact that the expressions for A are identical in analytic form to those for g , a similar procedure was employed in arriving at preliminary values for the $\bar{A}$-tensor components. This was accomplished through consideration of the individual experimental curves in the outer groups in Figures 15 and 17.

Using the Oklahoma State University IBM 360 computer facility the angular dependences of the lines in a $\{110\}$ plane were calculated using equation (4-2) in conjunction with the expressions for g in equations (4-3) through (4-9) and similar ones for A. The parameters of the $\bar{g}$ and $\bar{A}$ tensors were adjusted to yield the best over-all representation of the experimental data. The calculated results with $g_1 = 2.0031 \pm 0.0003$, $g_2 = 2.0019 \pm 0.0003$, $g_3 = 2.0025 \pm 0.0003$, $\psi = 45.2^\circ \pm 0.3^\circ$, and $A_1 = 1.054 \pm 0.001 \times 10^{-19}$ erg, $A_2 = 1.424 \pm 0.001 \times 10^{-19}$ erg, $A_3 = 1.052 \pm 0.001 \times 10^{-19}$ erg, $\alpha = 22.4^\circ \pm 0.1^\circ$ are presented on the right in Figures 15, 16, and 17. In the figures, H(4-7) for example, has been abbreviated as H(7). Hyperfine components are often expressed in reciprocal centimeters. Using the relation $E = h\nu = h\frac{c}{\lambda}$ the principal hyperfine components listed above can be converted to units cm^{-1} by merely dividing each by the factor (hc).

By noting the number of equivalent sites represented by each of the expressions in equations (4-3) through (4-9), it is seen that the model predicts 5 lines of double intensity and 2 of unit intensity for each of the hyperfine groups. Figure 17 indicates that only 6 components were resolved experimentally for the low field group, whereas the model predicts 7. However, two of the calculated curves, H(7) and H(8), are nearly coincident for all values of θ, their largest divergence being only 0.02 Gauss at $\theta \approx 30^\circ$. Experimentally, the two could not by resolved and would appear only as a single line with relative intensity 4 units.

In the middle hyperfine group of Figure 16 only 6 lines were observed experimentally, except for a partial splitting of one line near $\theta = 68^\circ$. This is not at variance with the predicted number of 7 for the following reasons. In the interval $\theta = 0^\circ \rightarrow 32^\circ$, either H(9) or H(5) is too near the isotropic nitrogen line for resolution. Either H(9) and H(4) or H(4) and H(7) are too near one another for resolution in the interval $\theta = 32^\circ \rightarrow 60^\circ$. Finally, H(5) and H(3) are separated by a maximum of only 0.09 Gauss (at $\theta = 70^\circ$) in the interval $\theta = 60^\circ \rightarrow 90^\circ$. Note from the calculated angular dependence shown in Figure 16 that H(3), H(4), and H(9) should converge at approximately the same field value as the isotropic nitrogen line when $\vec{H} \parallel [001]$; furthermore, four of the calculated lines converge at a field value nearly coincident with the central nitrogen line in the [110] direction. However, for $\vec{H}$ in the [111] direction, none of the anisotropic lines coincides with the central nitrogen line. This explains why the lines observed at the central nitrogen position with $\vec{H}$ parallel to $\langle 100 \rangle$ and $\langle 110 \rangle$ are greater in intensity than the central nitrogen line in the $\langle 111 \rangle$ directions.

The predictions of the model for the case in which the magnetic field $\vec{H}$ lies in a $\{100\}$ plane can be obtained with reference to a figure similar to Figure 22 but with $\vec{H}$ lying in the (001) plane and making an angle θ with the [100] axis.

When the cos φ_i in equation (4-1e) are expressed in terms of θ and ψ only 6 independent relations for g are obtained and each represents two equivalent types of centers. The independent expressions are given in equations (4-10) through (4-15). A sample derivation is given in Appendix A. The calculated angular behavior, using equation (4-2) with equations (4-10) through (4-15) and similar ones for A, is shown on the right in Figures 18, 19, and 20.

When the cos φ_i in equation (4-1e) are expressed in terms of θ and ψ for the case in which $\vec{H}$ lies in the (111) plane and makes an angle θ with the $[110]$ axis in this plane equations (4-16) through (4-27) are obtained, and each represents only one type of center. A sample derivation is given in the appendix. The calculated values of H for the lines in the high field hyperfine group ($m_I = -1$) are shown on the right in Figure 21. The calculated lines H(20) and H(25) as well as H(17) and H(25) are within 0.02 Gauss of each other except within a small region centered about $\theta = 30^\circ$. Therefore, only eleven lines, ten of unit intensity and one of double intensity, would be resolvable experimentally.

It should be noted that a physically different orientation of the $\bar{g}$ and $\bar{A}$ tensors can be generated from that shown in Figure 22 by rotating g_2 and A_2 by 180° about the direction of g_1 and A_1. In the new orientation obtained in this manner g_1 and A_1 still lie in the $[110]$ direction but g_2 and A_2 will make angles ψ and α, respectively, with the $[1\bar{1}0]$ axis instead of the $[\bar{1}10]$ axis as in Figure 22. There is no reason why Nature would prefer the orientation in Figure 22 as opposed to the one generated from it by the 180° rotation, and the two defect orientations should be distributed with equal probability

$g_1 : [1\bar{1}0],\ [\bar{1}10]$

$$g = \left\{ g_1^2 \cos^2(45^\circ + \theta) + g_2^2 \cos^2\psi \sin^2(45^\circ + \theta) + g_3^2 \sin^2\psi \sin^2(45^\circ + \theta) \right\}^{\frac{1}{2}} \qquad (4\text{-}10)$$

$g_1 : [0\bar{1}\bar{1}],\ [01\bar{1}]$

$$g = \left\{ \frac{1}{2} g_1^2 \sin^2\theta + g_2^2 \left[\cos\theta \sin\psi + \frac{1}{\sqrt{2}} \sin\theta \cos\psi \right]^2 + g_3^2 \left[\cos\theta \cos\psi - \frac{1}{\sqrt{2}} \sin\theta \sin\psi \right]^2 \right\}^{\frac{1}{2}} \qquad (4\text{-}11)$$

$g_1 : [101],\ [\bar{1}01]$

$$g = \left\{ \frac{1}{2} g_1^2 \cos^2\theta + g_2^2 \left[\sin\theta \sin\psi + \frac{1}{\sqrt{2}} \cos\theta \cos\psi \right]^2 + g_3^2 \left[\sin\theta \cos\psi - \frac{1}{\sqrt{2}} \cos\theta \sin\psi \right]^2 \right\}^{\frac{1}{2}} \qquad (4\text{-}12)$$

$g_1 : [011],\ [0\bar{1}1]$

$$g = \left\{ \frac{1}{2} g_1^2 \sin^2\theta + g_2^2 \left[\cos\theta \sin\psi - \frac{1}{\sqrt{2}} \sin\theta \cos\psi \right]^2 + g_3^2 \left[\cos\theta \cos\psi + \frac{1}{\sqrt{2}} \sin\theta \sin\psi \right]^2 \right\}^{\frac{1}{2}} \qquad (4\text{-}13)$$

$g_1 : [10\bar{1}],\ [\bar{1}0\bar{1}]$

$$g = \left\{ \frac{1}{2} g_1^2 \cos^2\theta + g_2^2 \left[\sin\theta \sin\psi - \frac{1}{\sqrt{2}} \cos\theta \cos\psi \right]^2 + g_3^2 \left[\sin\theta \cos\psi + \frac{1}{\sqrt{2}} \cos\theta \sin\psi \right]^2 \right\}^{\frac{1}{2}} \qquad (4\text{-}14)$$

$g_1 : [110],\ [\bar{1}\bar{1}0]$

$$g = \left\{ g_1^2 \cos^2(45^\circ - \theta) + g_2^2 \cos^2\psi \sin^2(45^\circ - \theta) + g_3^2 \sin^2\psi \sin^2(45^\circ - \theta) \right\}^{\frac{1}{2}} \qquad (4\text{-}15)$$

$g_1:[110]$

$$g=\left\{\frac{1}{3}g_1^2\sin^2\theta+g_2^2\left[\sqrt{\frac{2}{3}}\sin\theta\sin\psi-\cos\theta\cos\psi\right]^2+g_3^2\left[\sqrt{\frac{2}{3}}\sin\theta\cos\psi+\cos\theta\sin\psi\right]^2\right\}^{\frac{1}{2}} \tag{4-16}$$

$g_1:[\bar{1}\bar{1}0]$

$$g=\left\{\frac{1}{3}g_1^2\sin^2\theta+g_2^2\left[\sqrt{\frac{2}{3}}\sin\theta\sin\psi+\cos\theta\cos\psi\right]^2+g_3^2\left[\sqrt{\frac{2}{3}}\sin\theta\cos\psi-\cos\theta\sin\psi\right]^2\right\}^{\frac{1}{2}} \tag{4-17}$$

$g_1:[1\bar{1}0]$

$$g=\left\{g_1^2\cos^2\theta+\frac{1}{3}g_2^2\left[\sqrt{2}\sin\theta\sin\psi-\sin\theta\cos\psi\right]^2+\frac{1}{3}g_3^2\left[\sqrt{2}\sin\theta\cos\psi+\sin\theta\sin\psi\right]^2\right\}^{\frac{1}{2}} \tag{4-18}$$

$g_1:[\bar{1}10]$

$$g=\left\{g_1^2\cos^2\theta+\frac{1}{3}g_2^2\left[\sqrt{2}\sin\theta\sin\psi+\sin\theta\cos\psi\right]^2+\frac{1}{3}g_3^2\left[\sqrt{2}\sin\theta\cos\psi-\sin\theta\sin\psi\right]^2\right\}^{\frac{1}{2}} \tag{4-19}$$

$g_1:[011]$

$$\begin{aligned}g=\Bigg\{&\frac{1}{4}g_1^2\left[\frac{\sin\theta}{\sqrt{3}}-\cos\theta\right]^2\\&+g_2^2\left[\frac{1}{\sqrt{6}}\sin\theta\sin\psi-\frac{3}{2\sqrt{3}}\sin\theta\cos\psi-\frac{1}{\sqrt{2}}\cos\theta\sin\psi-\frac{1}{2}\cos\theta\cos\psi\right]^2\\&+g_3^2\left[\frac{1}{\sqrt{6}}\sin\theta\cos\psi+\frac{3}{2\sqrt{3}}\sin\theta\sin\psi-\frac{1}{\sqrt{2}}\cos\theta\cos\psi+\frac{1}{2}\cos\theta\sin\psi\right]^2\Bigg\}^{\frac{1}{2}}\end{aligned} \tag{4-20}$$

$g_1:[01\bar{1}]$

$$\begin{aligned}g=\Bigg\{&\frac{1}{4}g_1^2\left[\sqrt{3}\sin\theta+\cos\theta\right]^2\\&+g_2^2\left[\frac{1}{\sqrt{6}}\sin\theta\sin\psi-\frac{1}{2\sqrt{3}}\sin\theta\cos\psi-\frac{1}{\sqrt{2}}\cos\theta\sin\psi+\frac{1}{2}\cos\theta\cos\psi\right]^2\\&+g_3^2\left[\frac{1}{\sqrt{6}}\sin\theta\cos\psi+\frac{1}{2\sqrt{3}}\sin\theta\sin\psi-\frac{1}{\sqrt{2}}\cos\theta\cos\psi-\frac{1}{2}\cos\theta\sin\psi\right]^2\Bigg\}^{\frac{1}{2}}\end{aligned} \tag{4-21}$$

$g_1:[101]$

$$\begin{aligned} g = \Big\{ & \frac{1}{4} g_1^2 \Big[\frac{\sin\theta}{\sqrt{3}} + \cos\theta\Big]^2 \\ & + g_2^2\Big[\frac{1}{\sqrt{6}}\sin\theta\sin\psi + \frac{3}{2\sqrt{3}}\sin\theta\cos\psi + \frac{1}{\sqrt{2}}\cos\theta\sin\psi - \frac{1}{2}\cos\theta\cos\psi\Big]^2 \\ & + g_3^2\Big[\frac{1}{\sqrt{6}}\sin\theta\cos\psi - \frac{3}{2\sqrt{3}}\sin\theta\sin\psi + \frac{1}{\sqrt{2}}\cos\theta\cos\psi + \frac{1}{2}\cos\theta\sin\psi\Big]^2\Big\}^{\frac{1}{2}} \end{aligned} \tag{4-22}$$

$g_1:[\bar{1}01]$

$$\begin{aligned} g = \Big\{ & \frac{1}{4} g_1^2 \Big[\sqrt{3}\sin\theta - \cos\theta\Big]^2 \\ & + g_2^2\Big[\frac{1}{\sqrt{6}}\sin\theta\sin\psi - \frac{1}{2\sqrt{3}}\sin\theta\cos\psi + \frac{1}{\sqrt{2}}\cos\theta\sin\psi - \frac{1}{2}\cos\theta\cos\psi\Big]^2 \\ & + g_3^2\Big[\frac{1}{\sqrt{6}}\sin\theta\cos\psi + \frac{1}{2\sqrt{3}}\sin\theta\sin\psi + \frac{1}{\sqrt{2}}\cos\theta\cos\psi + \frac{1}{2}\cos\theta\sin\psi\Big]^2\Big\}^{\frac{1}{2}} \end{aligned} \tag{4-23}$$

$g_1:[0\bar{1}\bar{1}]$

$$\begin{aligned} g = \Big\{ & \frac{1}{4} g_1^2 \Big[\frac{-\sin\theta}{\sqrt{3}} + \cos\theta\Big]^2 \\ & + g_2^2\Big[\frac{1}{\sqrt{6}}\sin\theta\sin\psi + \frac{3}{2\sqrt{3}}\sin\theta\cos\psi - \frac{1}{\sqrt{2}}\cos\theta\sin\psi + \frac{1}{2}\cos\theta\cos\psi\Big]^2 \\ & + g_3^2\Big[\frac{1}{\sqrt{6}}\sin\theta\cos\psi - \frac{3}{2\sqrt{3}}\sin\theta\sin\psi - \frac{1}{\sqrt{2}}\cos\theta\cos\psi - \frac{1}{2}\cos\theta\sin\psi\Big]^2\Big\}^{\frac{1}{2}} \end{aligned} \tag{4-24}$$

$g_1:[10\bar{1}]$

$$\begin{aligned} g = \Big\{ & \frac{1}{4} g_1^2 \Big[-\sqrt{3}\sin\theta + \cos\theta\Big]^2 \\ & + g_2^2\Big[\frac{1}{\sqrt{6}}\sin\theta\sin\psi + \frac{1}{2\sqrt{3}}\sin\theta\cos\psi + \frac{1}{\sqrt{2}}\cos\theta\sin\psi + \frac{1}{2}\cos\theta\cos\psi\Big]^2 \\ & + g_3^2\Big[\frac{1}{\sqrt{6}}\sin\theta\cos\psi - \frac{1}{2\sqrt{3}}\sin\theta\sin\psi + \frac{1}{\sqrt{2}}\cos\theta\cos\psi - \frac{1}{2}\cos\theta\sin\psi\Big]^2\Big\}^{\frac{1}{2}} \end{aligned} \tag{4-25}$$

$g_1:[\bar{1}0\bar{1}]$

$$\begin{aligned} g = \Big\{ & \frac{1}{4} g_1^2 \Big[\frac{\sin\theta}{\sqrt{3}} + \cos\theta\Big]^2 \\ & + g_2^2\Big[\frac{1}{\sqrt{6}}\sin\theta\sin\psi - \frac{3}{2\sqrt{3}}\sin\theta\cos\psi + \frac{1}{\sqrt{2}}\cos\theta\sin\psi + \frac{1}{2}\cos\theta\cos\psi\Big]^2 \\ & + g_3^2\Big[\frac{1}{\sqrt{6}}\sin\theta\cos\psi + \frac{3}{2\sqrt{3}}\sin\theta\sin\psi + \frac{1}{\sqrt{2}}\cos\theta\cos\psi - \frac{1}{2}\cos\theta\sin\psi\Big]^2\Big\}^{\frac{1}{2}} \end{aligned} \tag{4-26}$$

$g_1:[0\bar{1}1]$

$$\begin{aligned} g = \Big\{ & \frac{1}{4} g_1^2 \Big[\sqrt{3}\sin\theta + \cos\theta\Big]^2 \\ & + g_2^2\Big[\frac{1}{\sqrt{6}}\sin\theta\sin\psi + \frac{1}{2\sqrt{3}}\sin\theta\cos\psi - \frac{1}{\sqrt{2}}\cos\theta\sin\psi - \frac{1}{2}\cos\theta\cos\psi\Big]^2 \\ & + g_3^2\Big[\frac{1}{\sqrt{6}}\sin\theta\cos\psi - \frac{1}{2\sqrt{3}}\sin\theta\sin\psi - \frac{1}{\sqrt{2}}\cos\theta\cos\psi + \frac{1}{2}\cos\theta\sin\psi\Big]^2\Big\}^{\frac{1}{2}} \end{aligned} \tag{4-27}$$

throughout the diamond lattice. However, the two cannot be distinguished in the ESR spectrum. This can be understood by noting that the g expression in equation (4-9) was obtained from the orientation of $\bar{g}$ and $\bar{A}$ in Figure 22; when $\psi + 180^\circ$ is substituted in place of ψ in equation (4-9) the expression for g (and the corresponding one for A) remains unchanged. By a rotation of 180° similar to that above, a new defect orientation can be generated from each of the other orientations in which g_1 and A_1 lie in the remaining $\langle 110 \rangle$ directions. In the ESR spectrum none of the additional possible orientations can be distinguished from the orientation from which it was obtained by 180° rotation. This can be shown by observing that substitution of $\psi + 180^\circ$ for ψ in each of the remaining expressions for g in equations (4-3) through (4-8) and (4-10) through (4-27) leaves the expression unaltered.

Frequency Dependence

Examination of an ESR spectrum at two different microwave frequencies is often useful in distinguishing whether two given lines arise from different paramagnetic species or are related to a single species through hyperfine interaction. The magnetic field interval separating two hyperfine lines having the same g value will be independent of the frequency whereas the interval between lines arising from different species will depend in a definite manner upon the frequency of observation. The typical x-band ($\sim$ 9 Kmc $\sec^{-1}$) and K- band ($\sim$20 Kmc $\sec^{-1}$) frequencies are ideal for studying an ESR spectrum at two different frequencies because there is a factor of two difference in frequency. However, measurement at x- and K-band frequencies requires two complete but separate spectrometers.

During the early stages of obtaining experimental data on the ESR spectra in Figure 12 advantage was made of the fact that the resonant frequency of the Varian model V-4531 microwave cavity with its quartz dewar in place differs by approximately 386 mc sec^{-1} from its resonant frequency with the dewar removed. Although the frequency difference provided by recording the spectra with and without the quartz dewar in place is much smaller than that of an x-band versus a K-band spectrometer, it was interesting to make the investigation. The spectra were recorded with the quartz dewar in place for the magnetic field $\vec{H}$ parallel to a $\langle 100 \rangle$, $\langle 110 \rangle$, and a $\langle 111 \rangle$ direction, and the frequency was determined to be 9.5198 Kmc sec^{-1}. Then, without disturbing the Duco cement bonding the diamond to the quartz orientation tube, the spectra for $\vec{H}$ parallel to a $\langle 100 \rangle$, $\langle 110 \rangle$, and a $\langle 111 \rangle$ axis were recorded with the quartz dewar removed from the cavity; for this case the frequency was determined to be 9.1340 Kmc sec^{-1}. A noticeable change in the appearance of the spectrum was observed only for the low field group of lines in the recording with the magnetic field parallel to a $\langle 110 \rangle$ crystalline direction. Since the frequency difference (386 mc sec^{-1}) between the recordings is relatively small, it is not surprising that more pronounced changes were not observed. Recordings of the spectra at the two frequencies for $\vec{H} \parallel \langle 110 \rangle$ are shown in Figure 23. The only noticeable difference between the two spectra is the position of line a_2 relative to lines d_2 and c_2. In the observation at 9.5198 Kmc sec^{-1}, the line a_2 is nearer d_2 than c_2 whereas a_2 is nearer c_2 than d_2 in the recording made at 9.1340 Kmc sec^{-1}.

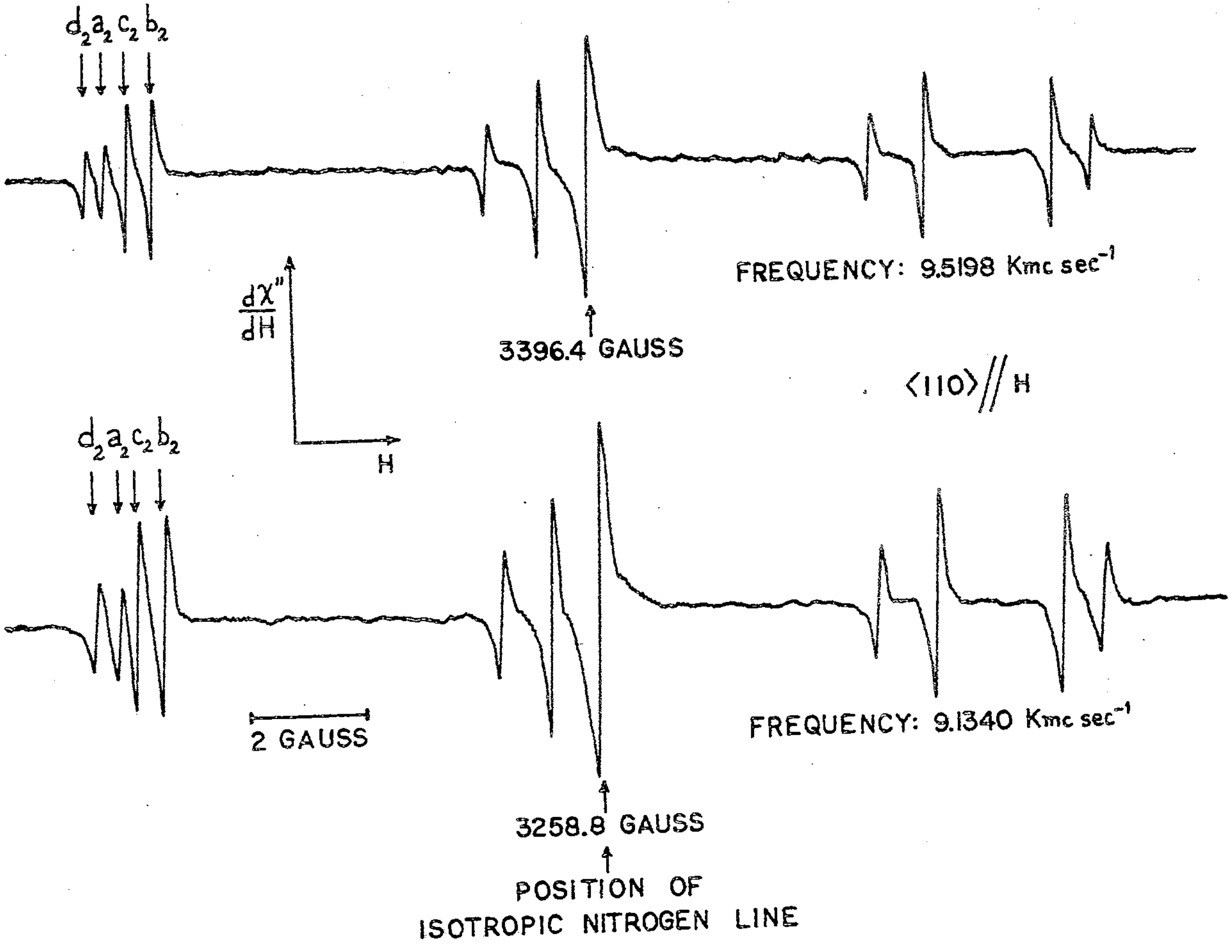

Figure 23. Observation of the Unusual ESR Spectra at Two Different Frequencies.

The frequency dependence displayed in Figure 23 can be understood on the basis of the model developed earlier in this chapter. Consider two hypothetical ESR spectral lines with g values g_1 and g_2 ($g_1 > g_2$) occurring at magnetic fields H_1 and H_2, respectively, as indicated in Figure 24.

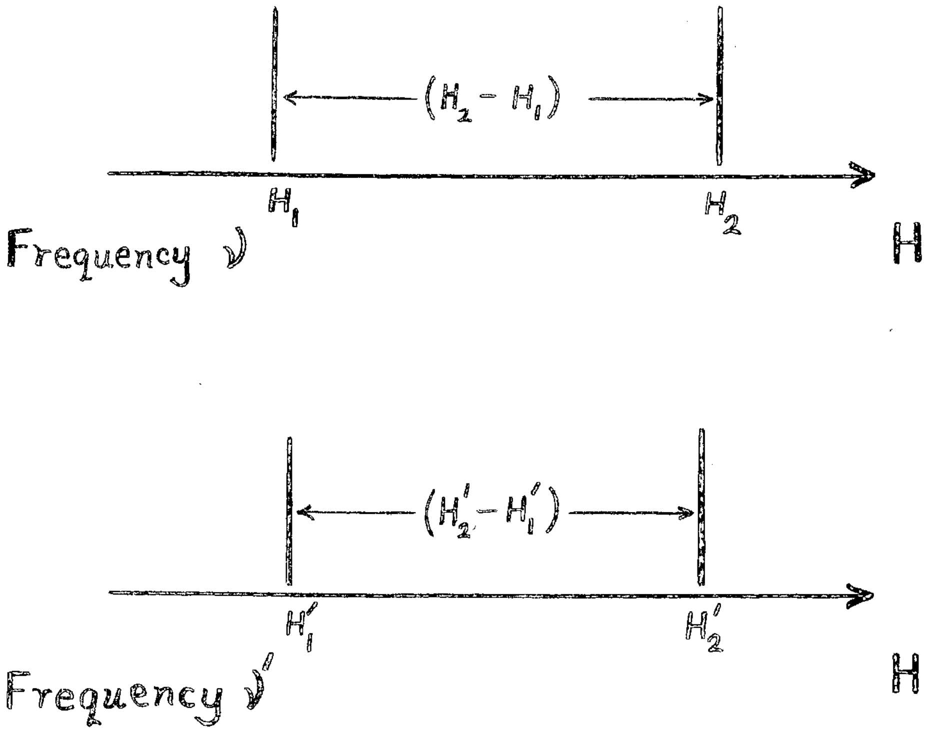

Figure 24. Hypothetical ESR spectral lines observed at two different frequencies

In the upper portion of Figure 24 the two lines are observed at a microwave frequency ν , and the lower schematic trace is recorded at a different frequency ν' . According to equation (2-14) the following relations hold.

For Observation at Frequency ν : $h\nu = g_1\beta H_1 = g_2\beta H_2$ (4-28)

For Observation at Frequency ν' : $h\nu' = g_1\beta H_1' = g_2\beta H_2'$ (4-29)

With the aid of simple algebraic manipulation the two relations above can be combined to yield the expression

$$(H_2 - H_1) - (H_2' - H_1') = \frac{h\delta}{\beta}\left[\frac{g_1 - g_2}{g_1 g_2}\right] \quad . \tag{4-30}$$

where $\delta \equiv \nu - \nu'$. Equation (4-30) states that the magnetic field interval measured between two ESR lines observed at frequency ν' will be less than the interval measured between the lines when they are observed at frequency ν , provided $\nu > \nu'$. If $\nu < \nu'$ the field interval at frequency ν' will exceed the interval at frequency ν . Note from equation (4-30) that any two lines associated with the same g value ($g_1 = g_2$) will be separated by the same magnetic field interval regardless of the difference in frequency between the observations. For example, the magnetic field interval between any two lines of the normal nitrogen spectrum in Figure 8 does not depend upon the frequency at which the spectrum is observed because the g-factor is isotropic with the value 2.0024 and therefore $g_1 \equiv g_2$.

In order to explain the frequency dependence shown in Figure 23, a schematic representation of the spectra for $\vec{H} // \langle 110 \rangle$ is presented in Figure 25. The labeling code of the lines in Figure 25 (as well as those in Figure 23) was determined by considering the ordering of H(3), H(4), H(5), H(6), H(7), H(8), and H(9) at $\theta = 90^\circ$

(i.e., $\vec{H} \parallel \langle 110 \rangle$) in the calculated results on the right in Figures 15, 16, and 17. For example, the lines labeled c_0, c_1, and c_2 in Figure 25 are related hyperfine lines and therefore the magnetic field interval $c_o \rightarrow c_1$ is equal to the interval $c_2 \rightarrow c_o$ in the first-order approximation. According to equation (4-30) the magnetic field interval $c_o \rightarrow c_1$ will be independent of frequency because the lines c_o, c_1, and c_2 all have the same g value equal to 2.00221 for $\vec{H} \parallel \langle 110 \rangle$. Similarly, each of the field intervals $a_o \rightarrow a_1$ ($= a_2 \rightarrow a_o$), $b_o \rightarrow b_1$ ($= b_2 \rightarrow b_o$), and $d_o \rightarrow d_1$ ($= d_2 \rightarrow d_o$) is independent of the frequency of observation because the lines of each triplet are related by the corresponding single g-value given in Figure 25.

Next, consider a magnetic field interval between two hyperfine lines whose g values for $\vec{H} \parallel \langle 110 \rangle$ are different, as for example the interval $b_o \rightarrow c_o$ in Figure 25. Making use of the fact that g_1 = 2.00264 and g_2 = 2.00221 for b_o and c_o, respectively, and $\delta \equiv \nu - \nu'$ $\cong$ 385.8 mc sec^{-1}, equation (4-30) predicts a difference of 0.03 Gauss between the interval $b_o \rightarrow c_o$ measured at 9.5198 Kmc sec^{-1} and that measured at 9.1340 Kmc sec^{-1}. The same is true concerning the intervals $b_1 \rightarrow c_1$ and $b_2 \rightarrow c_2$. Although an interval of 0.03 Gauss can be measured on a given recording of a spectrum, limitations in the magnetic field scanning stability and the corresponding field measurements prohibit the measurement of a 0.03 Gauss difference in comparing a field interval measured on one recording with an interval measured on a different recording. Furthermore, the change in interval, 0.03 Gauss, is only $\frac{1}{60}$ of the interval between lines b_1 and c_1, and therefore is unnoticeable in Figure 23. Similar remarks apply concerning experimentally unobservable shifts in other regions of the spectra

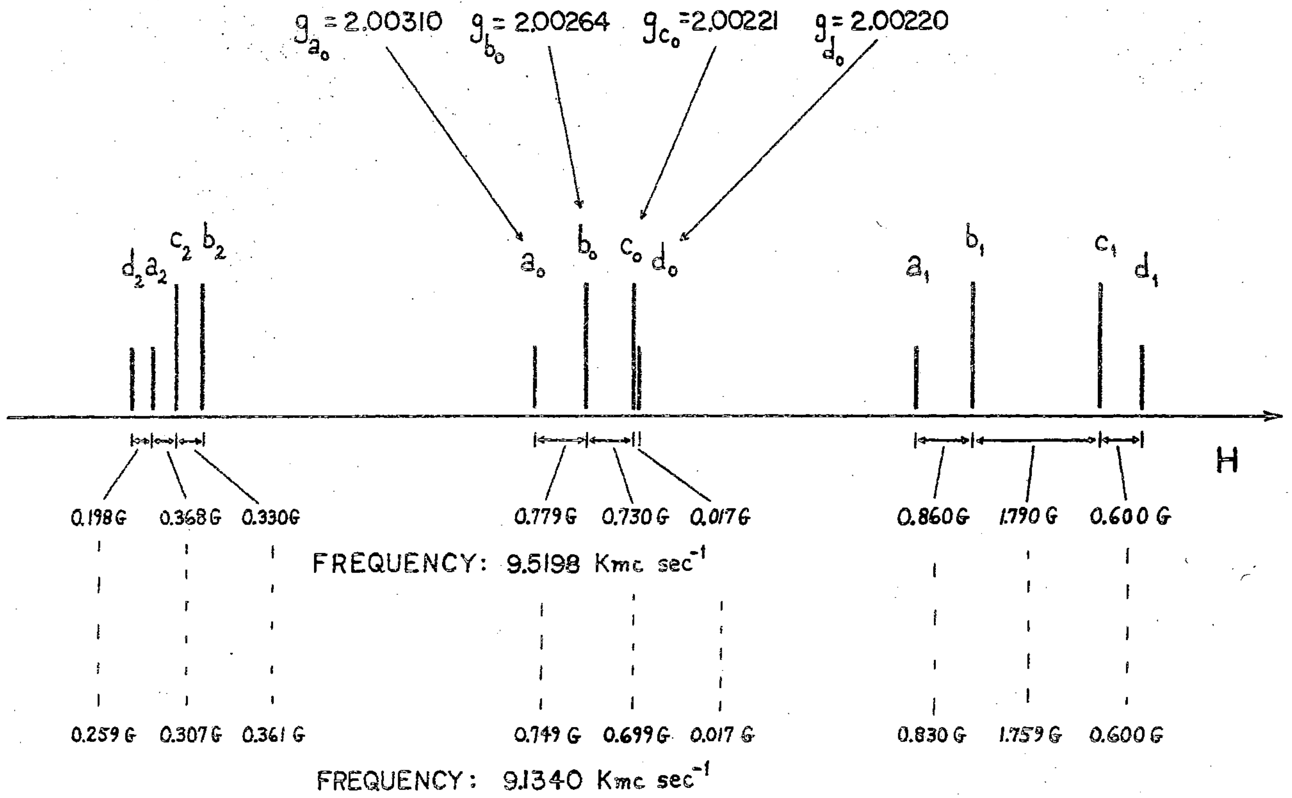

Figure 25. Theoretical Magnetic Field Intervals Between Lines in the Unusual ESR Spectra at Two Different Frequencies.

in Figure 23.

Note from Figure 25 that the lines c_o and d_o have nearly identical g values and therefore according to equation (4-30) the field interval between them should not vary with the frequency of observation. Also, the intervals $c_2 \rightarrow d_2$ and $d_1 \rightarrow c_1$ will be independent of the frequency. Since a_o and c_o (or d_o) are separated by the largest difference in g value, the field interval $a_2 \rightarrow c_2$ (or $a_1 \rightarrow c_1$) will undergo the greatest change when comparison is made between observations made at different frequencies. The magnitude of the change computed from equation (4-30) by substituting $g_1 = 2.00310$ and $g_2 = 2.00221$ is 0.06 Gauss. This change in interval is only $\frac{1}{50}$ of the interval between the components a_1 and c_1 and would be unobservable when comparing one recording with another. However, the change of 0.06 Gauss is 1/3 of the interval separating a_2 and c_2 and ¼ of that separating d_2 and a_2. From the preceding discussion it follows that the four lowest field lines in Figure 23 present a unique situation for testing the effect of the small frequency difference between the observations. First, the four lines d_2, a_2, c_2, and b_2 are well resolved but spaced very closely, thereby making relative changes easily detectable. Second, the components c_2 and d_2 have nearly identical g values so that their interval remains fixed regardless of the frequency, thus providing a reference against which small changes appear more noticeable. Third, but equally important, the difference $(g_1 - g_2)$ in equation (4-30) is largest for the lines a_2 and c_2 (or d_2), and a_2 occurs near the middle of the small but fixed interval $d_2 \rightarrow c_2$. Therefore, the relatively large shift of 0.06 Gauss originating from the difference $g_1 - g_2$ appears in the region of the spectrum where conditions are optimum for the shift to be observed.

Finally, the observation shown in Figure 23 that a_2 is nearer c_2 at the frequency 9.1340 Kmc sec^{-1} than at the frequency 9.5198 Kmc sec^{-1} can be understood by the following reasoning. As mentioned earlier, the interval $d_2 \rightarrow c_2$ does not change with frequency because the g values of c_o and d_o are essentially identical; furthermore, the interval $c_2 \rightarrow c_o$ does not depend upon frequency because c_2 and c_o are hyperfine lines with the same g value. Applying equation (4-30) to the two lines c_o and a_2 and taking care to write the subscripts and primes properly in relation to the defining Figure 24, the following expression is obtained.

$$(H_{C_o}-H_{A_2})-(H'_{C_o}-H'_{A_2})=\frac{h\delta}{\beta}\left[\frac{g_{A_2}-g_{C_o}}{g_{A_2}g_{C_o}}\right] \qquad (4\text{-}31)$$

In the above expression $\delta \equiv \nu - \nu'$ and the primed field values are measured at frequency ν' and the unprimed fields at frequency ν.

From Figure 25 it is seen that $g_{A_2} - g_{C_o} > 0$ and hence the right side of equation (4-31) is positive provided ν = 9.5198 Kmc sec^{-1} and ν' = 9.1340 Kmc sec^{-1}. This implies that the unprimed interval measured at the frequency 9.5198 Kmc sec^{-1} is greater than the primed interval measured at 9.1340 Kmc sec^{-1}. That is, since c_2 is fixed relative to c_o, a_2 will be nearer c_2 in the recording made at 9.1340 Kmc sec^{-1} than in that made at 9.5198 Kmc sec^{-1}. This is in agreement with the experimental observations presented in Figure 23.

Summary

The unusual ESR spectrum observed in three natural Type I diamonds is composed of three anisotropic systems of lines. The lines of the high and low field groups occur at approximately the same magnetic field interval above and below the corresponding lines of the central group. Furthermore, for an arbitrary orientation of the magnetic field in the major crystalline planes, the three corresponding lines are of the same intensity. These aspects suggest that the spectrum arises from hyperfine interaction of an unpaired electron with a spin-one nucleus. The diamonds exhibiting the uncommon spectrum also contain the nitrogen spectrum reported by Smith et al., and therefore it is reasonable to assume that an unpaired electron located at a defect center undergoes hyperfine interaction with the nitrogen nucleus whose spin is one. The spin Hamiltonian characterizing the defect centers is of the form $\mathcal{H} = \beta\ \bar{g}\cdot\bar{S}\cdot\bar{H} + \bar{A}\cdot\bar{I}\cdot\bar{S}$ with $S = \frac{1}{2}$ and $I = 1$. Figures 15 through 21 show that the number of lines, their angular behavior, and the relative intensities are properly predicted by a model in which identical defect centers are differently oriented in the diamond lattice. For example, the defect center could be a substitutional nitrogen atom associated with a defect such as a carbon atom vacancy. The principal components g_1 and A_1 of the aniostropic $\bar{g}$ and $\bar{A}$ tensors can lie along any of the twelve $\langle 110 \rangle$ directions. Although for a given defect center the components g_1 and A_1 coincide, the remaining components of $\bar{g}$ and $\bar{A}$ for the center are not coincident; that is, the tensors $\bar{g}$ and $\bar{A}$ are not diagonal in the same coordinate system. For example, those sites having g_1 in the $[110]$ direction have g_2, g_3, A_2, and A_3 lying in the $(\bar{1}10)$ plane, but g_2 and A_2 make angles $\psi = 45.2^\circ$ and $\alpha = 22.4^\circ$, respectively, with the $[\bar{1}10]$ axis in the $(\bar{1}10)$ plane. The angular dependencies shown on the right in Figures 15 through 21 were calculated with the aid of the IBM 360 computer and are in good agreement with the experimentally observed angular behaviors. Finally, the observed frequency dependence presented in Figure 23 was shown to be consistent with the defect model advanced earlier in accounting for the anisotropic properties of the spectrum.

CHAPTER V

A SEARCH FOR AN EFFECT OF STRESS ON ELECTRON SPIN RESONANCE IN DIAMOND

Preliminary Remarks

It is a relatively simple matter to study the effect of stress on the electron spin resonance spectra of impurity ions in plastically deformable host crystals. The spectrum of the undeformed paramagnetic solid is merely recorded in the usual manner, after which the solid is removed from the microwave cavity of the electron spin resonance spectrometer and deformed plastically by any of several available means. Finally, the deformed crystal is again placed in the cavity of the spectrometer and its paramagnetic spectrum is recorded for comparison with the spectrum of the crystal in its undeformed state. A study such as this does not require any special design or modification of the spectrometer microwave cavity. However, in some cases more physical information is obtainable from an investigation of the ESR spectrum of a solid while the solid is simultaneously subjected to stress. In addition to preserving the crystal for further experimentation this method allows stress effects to be studied as a function of the magnitude of applied stress. Alterations of the microwave cavity are necessary, however, if a solid is to be subjected to stress at the same time its electron spin resonance spectrum is being observed.

Design of Microwave Cavity and Stress Application Device

To investigate the electron spin resonance spectrum of a solid simultaneously subjected to uniaxial stress it is necessary that stress be transmitted to the solid while the solid is maintained stationary in the region of maximum microwave magnetic field of the cavity, and the cavity remains in its usual position in the presence of the large external magnetic field. To meet these requirements the choice of material for introducing stress into the cavity is a crucial matter. The material must possess a high degree of rigidity for stress studies involving large stresses. Especially is this true when stress experiments are performed on a substance such as diamond. It is also required that the material for applying the stress be diamagnetic since it must necessarily remain in the presence of the large external magnetic field required for the resonance condition. Moreover, a portion of the stress transmission material must enter the microwave cavity and therefore the material must have excellent insulating properties to prevent microwave energy absorption and the resultant decrease in the cavity "Q-factor". Finally, the material must be free from any electron spin resonance signal of its own which would confuse the analysis of the spectrum under consideration. Workers studying the effect of stress on ESR in solids other than diamond have successfully employed Teflon as a stress transmitting material (41). Delrin, which has a higher elastic limit than Teflon by a factor of ten, also meets the above requirements. In our particular case of stress studies on diamond, a particular type of alumina ceramic has proved far superior to either Teflon or Delrin.

The stress application device and special cavity design developed for studying electron spin resonance in a solid simultaneously subjected to uniaxial compressive stress are shown diagrammatically in Figures 26 and 27. The microwave cavity, in the form of a rectangular parallelopiped, is constructed from four pieces, three of which are diamagnetic stainless steel. The fourth, a brass top plate, serves also to connect the cavity to the waveguide. The square-cornered, U-shaped section with two ¼" diameter holes which allow entry of the stress rods serves as a form to which the top plate and the broad sides of the cavity are attached. Each of the broad sides is constructed from 0.015" thick stainless steel. The 100 Kc sec^{-1} modulation field coils are mounted on the external sides of the broad cavity walls such that their centers coincide with the geometric center of the cavity opening. The thickness of the broad walls is adequate to provide mechanical stability but small enough to prevent excessive 100 Kc sec^{-1} eddy current density which would introduce extraneous fields at the position of the sample and interfere with the 100 Kc sec^{-1} modulation process. The top plate of the cavity contains a 3/16" diameter iris hole for the coupling of microwave energy from the spectrometer waveguide into the cavity. The brass matching probe can be moved along the diameter of the iris, thereby providing a fine adjustment on the coupling of microwave energy for optimum sensitivity.

The inner cross-sectional dimensions of the cavity are those of the standard x-Band waveguide employed in the spectrometer, i.e., 0.40" x 0.90". The 1.70" length of the cavity opening is such that the

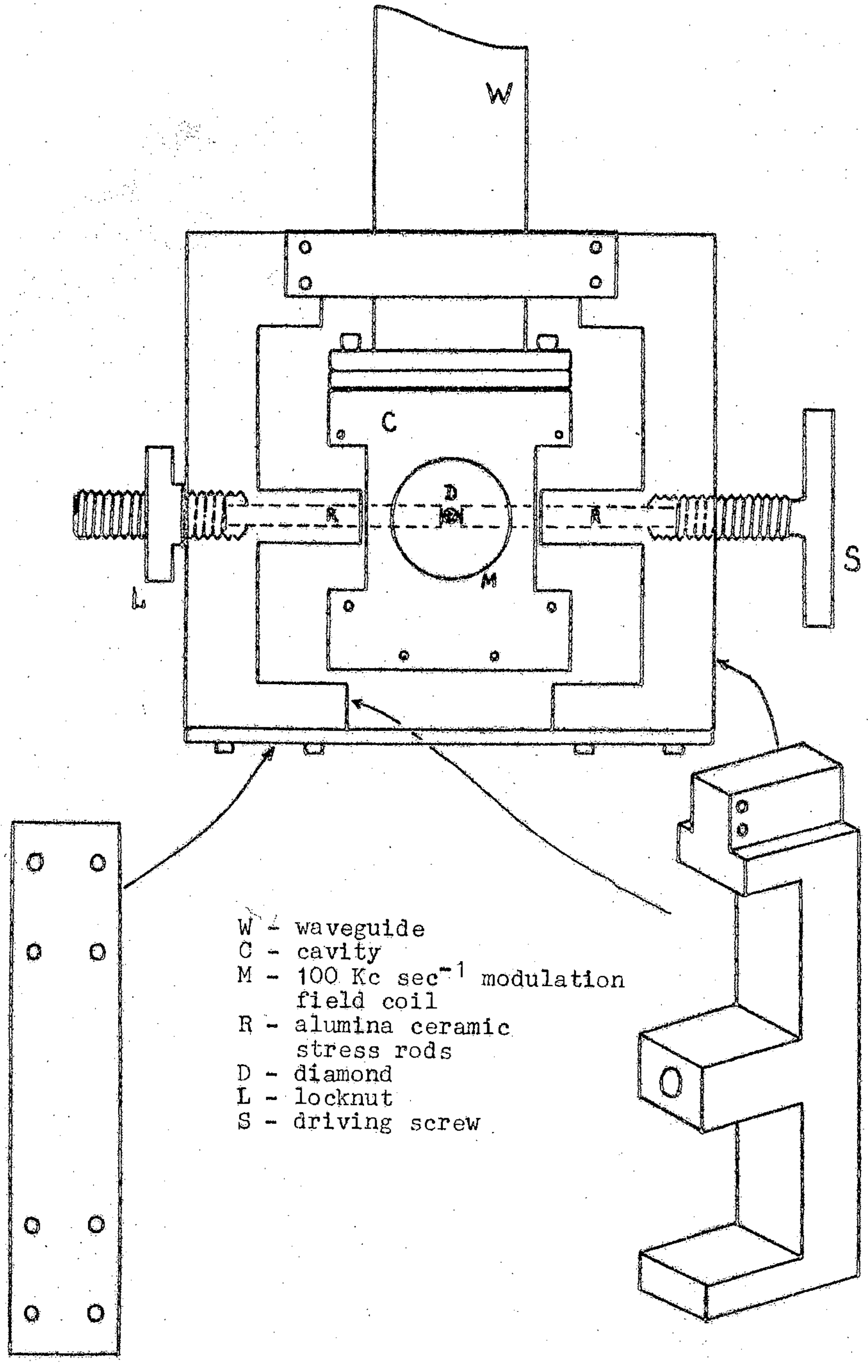

W - waveguide
C - cavity
M - 100 Kc sec^{-1} modulation field coil
R - alumina ceramic stress rods
D - diamond
L - locknut
S - driving screw

Figure 26. Special Microwave Cavity and Stress Application Device.

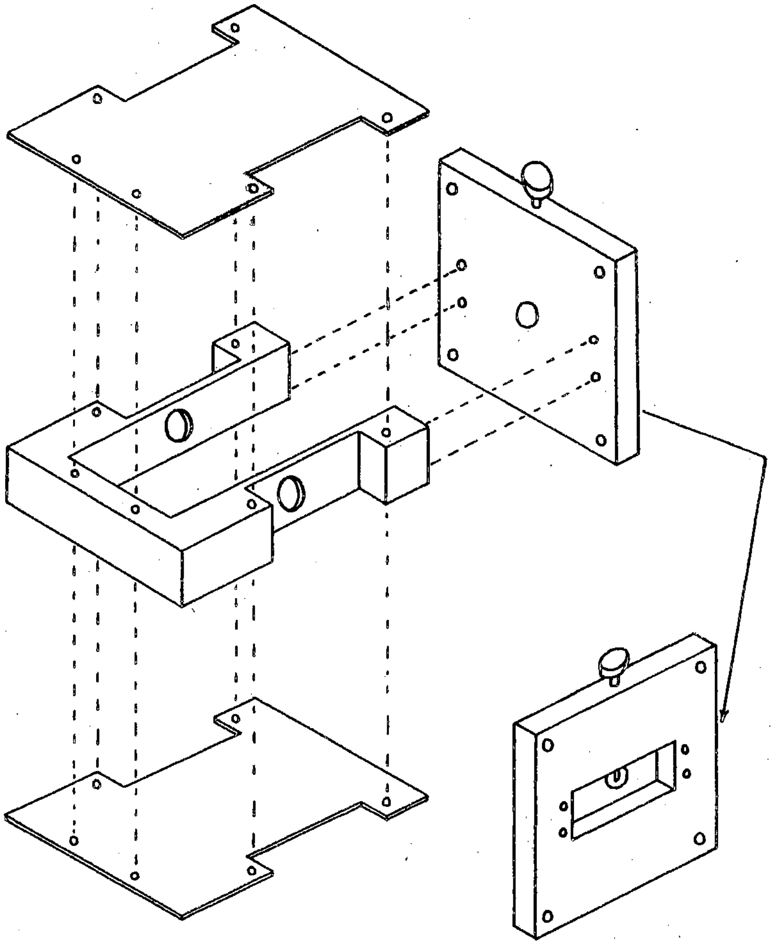

Figure 27. Expanded View of the Special Microwave Cavity.

TE_{102} mode of the rectangular parallelopiped cavity is sustained at a resonant frequency of approximately 9.3 Kmc sec^{-1}. Operation in this mode requires that the paramagnetic solid be located at the geometric center of the cavity. All relevant portions of the four-piece cavity design are silver plated to provide the required conducting surfaces for the cavity interior. The thickness of the silver plating is 0.0004 in. ± 0.0001 in. (approximately ten times the skin depth of microwaves at the frequency employed), which is sufficient to prevent dissipation of microwave energy in the cavity walls but sufficiently thin to minimize eddy current distributions induced by the modulation field which would otherwise result in signal distortion.

The device for applying uniaxial stress to the diamond while it is located at the geometric center of the cavity is composed of two E-shaped diamagnetic stainless steel components, each of which contains a 0.237" diameter stress-transmitting rod. A brass strip joins the bottom portions of the stainless steel components, and their upper portions are joined by two brass strips which also function in clamping the device firmly to the waveguide just above the point at which the cavity is connected. The stress transmission rods enter the cavity through holes positioned in the center of the two long narrow cavity sides. These holes are slightly larger than the diameter of the stress rods, and when the device is properly aligned uniaxial stress can be applied to the sample at the cavity center without introducing any torques or stresses on the cavity body. One of the stainless steel components of the stress device is provided with a screw and locknut acting as an anchor against which one of the stress rods is forced. One flat face of the diamond under study is attached with

Duco cement to one end of this stress rod and the rod is then positioned by means of the screw and locknut so that the sample is located at the geometric center of the cavity (i.e., at the region of maximum microwave magnetic field for the TE_{102} mode). Uniaxial compressive stress can then be applied by forcing the other stress rod against the diamond mounted on the stationary stress rod. The thin film of cement between the diamond and the anchored stress rod aids in distributing the stress evenly over the face of the diamond. A small circular Teflon disc 0.01" thick attached to the movable stress rod before each experiment aids in achieving a uniform stress distribution over the surface of the diamond in contact with this rod. A similar Teflon disc lubricated with Vaseline and attached to the opposite end of the movable stress rod prevents the driving screw S from rotating the rod as the diamond is stressed.

Experimental Study on Diamond

The special microwave cavity and stress application device were used in studying the effect of uniaxial compressive stress on electron spin resonance in Type I diamonds. Teflon and Delrin were employed as stress rods during the early stages of the work. In view of the great rigidity of the diamond lattice neither Teflon nor Delrin can function effectively as stress rods. However, a particular type of alumina ceramic called "Al Si Mag 614" and manufactured by the American Lava Corp. of Chattanooga, Tennessee, was found to be ideal in applying large stresses to the diamonds. The ceramic has a hardness rating of 9 on the Moh Scale, which is next to that of diamond whose rating on the same scale is 10. Not only does its introduction into the cavity result in negligible microwave energy absorption but also the ceramic is free from any inherent paramagnetic resonance near $g = 2.00$ which would interfere with that of diamond. Important for stressing diamonds is the fact that the ceramic possesses a very large compressive strength of 375,000 lbs in.$^{-2}$.

The effectiveness of the ceramic stress rods in elastically distorting the diamond lattice was evident from the ease with which stress birefringence effects could be induced in the diamonds. Nearly all diamonds exhibit some birefringence in their natural state (42). The striking changes in the birefringence pattern were observed by removing the stress application device from the cavity, inserting a diamond between the stress rods and placing the apparatus on the stage of a polarizing microscope. Upon applying stress to the diamond while viewing the specimen through the microscope, a continuously changing pattern of brilliant colors moved across the field of view as the stress was increased. Complete removal of the stress resulted in a return of the birefringence pattern exhibited by the diamond in the absence of external stress. The absence of any hysteresis in the stress birefringence effects indicated that the deformation of the diamond was entirely elastic.

Only those diamonds having two naturally flat, parallel opposite faces were suitable for subjection to stress. A total of fourteen diamonds was examined in the study. Taking into account the estimated force transmitted by a certain torque applied to the driving screw and considering the area of contact between the diamonds and the stress rods, the estimated maximum uniaxial stress applied to the diamonds was approximately 1.5×10^4 Kg cm^{-2}. In making a study with a given diamond the apparatus was assembled with the diamond and stress rods in position and the ESR spectrum was first recorded in the absence of applied stress; stress was then applied and the spectrum again recorded. After each subsequent increase of stress the ESR spectrum of the diamond was recorded. Each recording of the ESR spectrum under application of stress was carefully compared with the stress-free recording to determine if (1) any broadening of the spectral lines resulted, (2) any change in relative intensity of the lines occurred, (3) any change in magnetic field interval between spectral components occurred, and (4) any spectral lines disappeared or any new lines appeared. No change resulting from the application of stress was observed in the nitrogen spectrum or in the additional complex spectra of any of the fourteen diamonds investigated. Two diamonds were accidently shattered during the application of stress but no change was observed in the ESR spectra up to the point of fracture.

A study was also made to determine whether the g value of the nitrogen resonance is sensitive to application of uniaxial compressive stress. The method discussed in Chapter IV of preparing a small sample of powdered DPPH ($g = 2.0036 \pm 0.0003$) to serve as a standard g-value indicator attached directly to the diamond was actually developed during the experiments designed to study the effect of stress on the g value of the nitrogen resonance. A schematic view of the diamond D-82, alumina ceramic stress rods, and the DPPH sample is shown in Figure 28. The DPPH sample was attached to the diamond in a manner such that no contact was made with the stress rods. This made it possible to record the standard DPPH resonance line simultaneously with the nitrogen spectrum. Since the g values of the nitrogen signal and DPPH

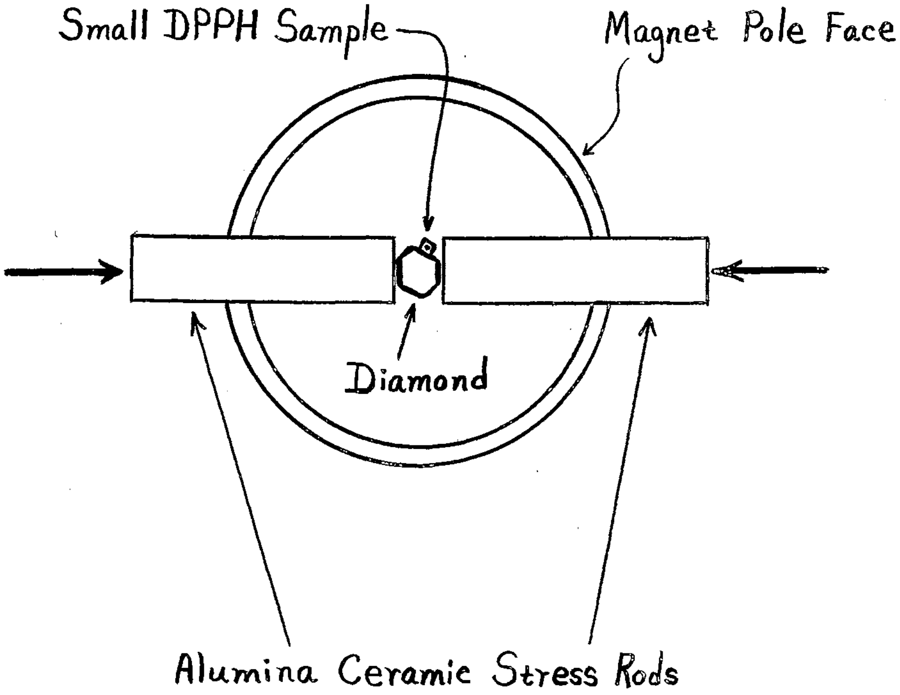

Figure 28. Schematic diagram of stress rods, diamond, and DPPH sample when viewed in a direction parallel to the external magnetic field.

resonance line are 2.0024 and 2.0036, respectively, application of equation (2-14) shows that the central nitrogen line is separated from the DPPH line by approximately 1.99 Gauss at a nominal cavity resonant frequency of 9.3 Kmc sec^{-1}. A change in g value of the nitrogen spectrum under application of uniaxial stress would manifest itself as a change in magnetic field interval between the central nitrogen line and the DPPH signal. Therefore, to test the effect of stress on the nitrogen g-value the magnetic field interval $H_{DPPH} \rightarrow H_{Diamond}$ in a stress-free recording must be compared with the same interval when the diamond is subjected to stress. This necessarily requires comparison of a magnetic field interval measured on one recording with that measured on another. Although a relative interval of magnitude 0.03 Gauss can be measured on a given recording, approximately ± 0.08 Gauss is the lower limit of accuracy when comparing intervals on different recordings. No shift in the nitrogen g-value was observed under maximum applied stress and if one is present its magnitude is less than ± 0.00005 or less than ± 0.003% of the nitrogen g-value.

Summary and Discussion

The absence of an observable stress effect on the ESR spectra in diamonds appears somewhat paradoxical when it is recalled that changes in the birefringence patterns of the diamonds were easily induced with the aid of the stress application device. It would seem that a deformation of the diamond lattice sufficient to produce easily detectable alterations in the birefringence would alter the lattice parameters to the extent that a stress-induced change would occur in the ESR spectra. The readily observable stress birefringence effects can be made compatible with the unobservable effect of stress on the ESR spectra through the following reasoning. The diamond structure consists essentially of an array of very compact carbon nuclei which are relatively widely separated but bound by electrons moving about two adjacent nuclei. During an elastic deformation of the crystal bond distances and angles are changed slightly, but the nuclei are virtually unaffected. Changes in the bond characteristics give rise to modifications in the polarizability of the bonding electrons which results in a change in the refractive index of the diamond. Now, consider a substitutional nitrogen atom whose donor electron is confined mainly to the nitrogen and one of the four nearest neighbor carbon atoms. Under the application of uniaxial stress the nitrogen nucleus substituted for a carbon nucleus is essentially unaffected as are the carbon nuclei. The amplitude of the donor electronic wave function at the position of the nitrogen nucleus, which determines the isotropic portion of the hyperfine splitting, is relatively undisturbed by the application of stress. In connection with the highly localized nature of the unpaired donor electron it follows that the donor electron does not "belong" to the entire crystal as do the bonding electrons whose stress-induced change in polarizability results in the observable stress-birefringence effects. As a result of the extreme localization of the donor electron wave function, the ground state energy level of the unpaired electron lies "deep" within the large forbidden energy gap (approximately 5.6 electron volts) separating the valence band from the conduction band in the diamond energy band structure. In fact, the ground state level lies 1.7 eV below the bottom of the conduction band. The localized donor electron is truly isolated from stress-induced perturbations of the band-gap edges arising from elastic distortion of the diamond lattice. In view of the great rigidity of the diamond structure it appears that fracture will result before sufficient elastic deformation can occur to alter significantly the magnetic environment of the nitrogen paramagnetic species.

SELECTED BIBLIOGRAPHY

(1) J. H. E. Griffiths, J. Owen, and I. M. Ward, "Paramagnetic Resonance in Neutron-Irradiated Diamond and Smoky Quartz," Nature 173, 439 (1954).

(2) M. C. M. O'Brien and M. H. L. Pryce, "Paramagnetic Resonance in Irradiated Diamond and Quartz: Interpretation," Conference on Defects in Crystalline Solids, (Physical Society, London, 1955) p. 88.

(3) J. A. Baldwin, "Electron Paramagnetic Resonance Investigation of the Vacancy in Diamond," Phys. Rev. Letters 10, 220 (1963).

(4) E. A. Faulkner and J. N. Lomer, "Electron Spin Resonance in Electron-Irradiated Diamond," Phil. Mag. 7, 1995 (1962).

(5) E. A. Faulkner, E. W. J. Mitchell, and P. W. Whippey, "Electron Spin Resonance in Neutron-Irradiated Diamond," Nature 198, 981 (1963).

(6) E. A. Harris, J. Owen, and C. Windsor, "Damage Centers in Irradiated Diamond," Bull. Am. Phys. Soc. 8, 252 (1963).

(7) W. V. Smith, P. P. Sorokin, I. L. Gelles, and G. J. Lasher, "Electron Spin Resonance of Nitrogen Donors in Diamond," Phys. Rev. 115, 1546 (1959).

(8) J. H. N. Loubser and L. Du Preez, "New Lines in the Electron Spin Resonance Spectrum of Substitutional Nitrogen Donors in Diamond," Brit. J. Appl. Phys. 16, 457 (1965).

(9) W. V. Smith, I. L. Gelles, and P. P. Sorokin, "Electron Spin Resonance of Acceptor States in Diamond," Phys. Rev. Letters 2, 39 (1959).

(10) J. P. King, M. D. Bell, and W. J. Leivo, "Effects of Light on the Electron Spin Resonance of Diamond," Bull. Am. Phys. Soc. 11, 834 (1966).

(11) W. C. Steckelberg and W. J. Leivo, "Electron Spin Resonance of Natural Diamonds," Bull. Am. Phys. Soc. 13, 1473 (1968).

(12) R. Robertson, J. J. Fox, and A. E. Martin, "Two Types of Diamond," Phil. Trans. Roy. Soc. London A232, 463 (1934).

(13) J. F. H. Custers, "Unusual Phosphorescence of a Diamond," Physica 18, 489 (1952).

(14) H. B. Dyer, F. A. Raal, L. Du Preez, and J. H. N. Loubser, "Optical Absorption Features Associated with Paramagnetic Nitrogen in Diamond," Phil. Mag. 11, 763 (1965).

(15) M. D. Bell and W. J. Leivo, "Electron Spin Resonance in Semiconducting Diamonds," J. Appl. Phys. 38, 337 (1967).

(16) G. S. Danil'chuk, L. N. Ganjuk, A. E. Koval'skii, P. P. Pogoretskii, G. A. Podzyarei, and L. A. Shul'man, "Nitrogen Impurity Centers in Synthetic Diamond Powder," Theoretickeskaya i Eksperimental'naya Khimiya 1, 367 (1965).

(17) L. A. Shul'man and G. A. Podzyarei, "Dipole-Dipole and Exchange Interactions of Nitrogen Centers in Synthetic Diamonds," Theroeticheskaya i Eksperimental'naya Khimiya 1, 561 (1965).

(18) M. J. A. Smith, B. R. Angel, and R. G. Emmons, "Distribution of Substitutional Nitrogen Donors in Synthetic Diamonds," Nature 210, 692 (1966).

(19) C. M. Huggins and P. Cannon, "Diamonds Containing Controllable Impurity Concentrations," Nature 194, 829 (1962).

(20) J. H. N. Loubser and W. P. Van Ryneveld, "Electron Spin Resonance of Nickel in Synthetic Diamond," Nature 211, 517 (1966).

(21) B. R. Angel and M. J. A. Smith, "The Reduction of Electron-Spin-Resonance Linewidths in Synthetic Diamond," Brit. J. Appl. Phys. (J. Phys. D) 1, 373 (1968).

(22) G. E. Uhlenbeck and S. Goudsmit, "Ersetzung der Hypothese vom unmechanischen Zwang durch eine Forderung bezuglich des inneren Verhaltens jedes einzelnen Elektrons," Die Naturwiss. 13, 953 (1925).

(23) J. Schwinger, "On Quantum-Elcetrodyanamics and the Magnetic Moment of the Electron," Phys. Rev. 73, 416 (1948).

(24) E. Merzbacher, Quantum Mechanics, (Wiley and Sons, New York, 1961) p. 345.

(25) I. I. Rabi, "Use of Rotating Coordinates in Magnetic Resonance Problems," Rev. of Mod. Phys. 26, 167 (1954).

(26) G. E. Pake, Paramagnetic Resonance, (Benjamin, New York, 1962).

(27) A. Messiah, Quantum Mechanics, Vol. II, (North-Holland, Amsterdam, 1962) p. 708.

(28) C. P. Slichter, *Principles of Magnetic Resonance*, (Harper and Row, New York, 1963) p. 190.

(29) G. Breit and I. I. Rabi, "Measurement of Nuclear Spin," Phys. Rev. *38*, 2082 (1931).

(30) H. J. Reich, J. G. Skalnik, P. F. Ordung, and H. L. Krauss, *Microwave Principles*, (D. Van Nostrand, Princeton, 1957). p. 65.

(31) M. D. Bell, "Electron Spin Resonance in Diamond," (Ph. D. thesis, Oklahoma State University, 1964).

(32) C. H. Townes and A. L. Schawlow, Microwave Spectroscopy, (McGraw-Hill, New York, 1955) p. 401.

(33) D. J. E. Ingram, *Spectroscopy at Radio and Microwave Frequencies*, (Butterworths, London, 1967).

(34) M. W. P. Stranberg, M. Tinkham, I. H. Solt, Jr., and C. F. David, "Recording Magnetic-Resonance Spectrometer," Rev. Sci. Instr. *27*, 596 (1956).

(35) C. P. Poole, Jr., *Electron Spin Resonance*, (Interscience Publishers, New York, 1967).

(36) "Tentative Method for Determining the Orientation of a Metal Crystal," ASTM Designation: E 82-49T (1949).

(37) J. P. King, "Effects of Light on the Electron Spin Resonance of Diamond," (Ph. D. thesis, Oklahoma State University, 1966).

(38) C. J. Northrup, "Photovoltage at a Metal to Diamond Contact," Ph. D. thesis, Oklahoma State University, 1966).

(39) F. G. Chesley, "Investigation of the Minor Elements in Diamond," Am. Mineral. *27*, 20 (1942).

(40) W. Kaiser and W. L. Bond, "Nitrogen, a Major Impurity in Common Type I Diamond," Phys. Rev. *115*, 857 (1959).

(41) R. A. Levy, "Resonant Spin-Spin Interaction Between Donors and Acceptors in Silicon," Phys. Rev. Letters *5*, 425 (1960).

(42) S. Tolansky, "Birefringence of Diamond," Nature *211*, 158 (1966).

APPENDIX

The expression for g given by equation (4-3) can be obtained with the aid of Figure 29 in which g_1 is in the $\left[1\bar{1}0\right]$ direction and $\vec{H}$ is in the $(1\bar{1}0)$ plane.

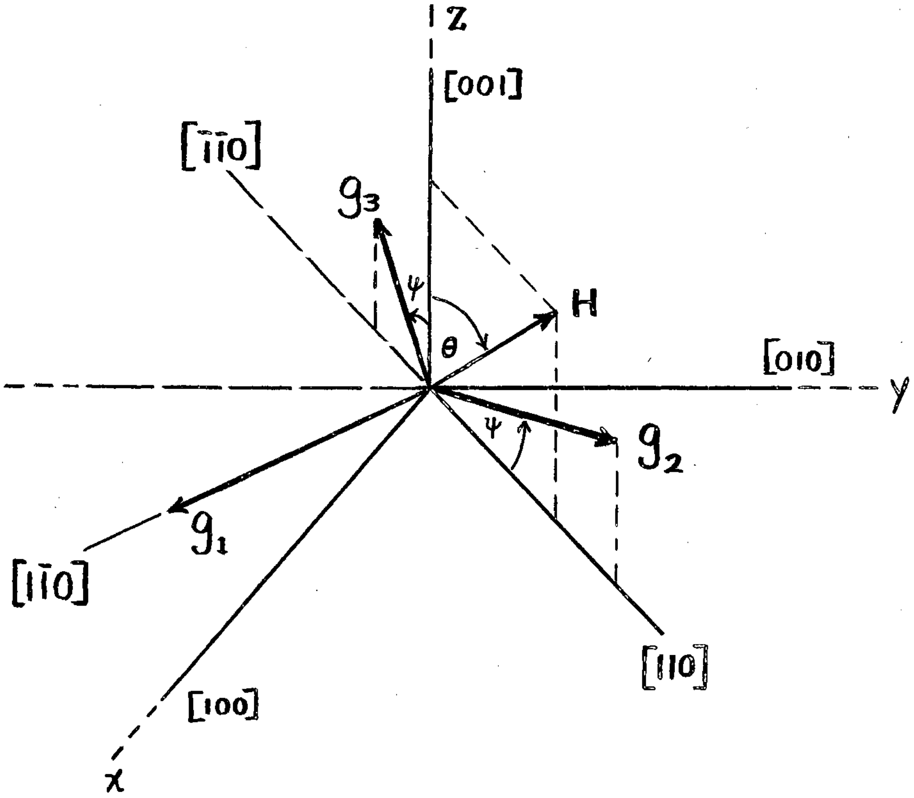

Figure 29. Geometry Used in Deriving Equation (4-3).

It is readily seen that the angles φ_1, φ_2, and φ_3 which $\vec{H}$ makes with the directions of g_1, g_2, and g_3, respectively, are given by

$$\left.\begin{aligned}\varphi_1 &= 90^\circ \\ \varphi_2 &= 90^\circ - (\psi + \theta) \\ \varphi_3 &= \theta + \psi\end{aligned}\right\} \quad \text{(A-1)}$$

When the angles in equation (A-1) are substituted into the expression $g = \sqrt{g_1^2\cos^2\varphi_1 + g_2^2\cos^2\varphi_2 + g_3^2\cos^2\varphi_3}$, equation (4-3) in the text is obtained. The corresponding expression for A is obtained by replacing g_1, g_2, g_3, and ψ by A_1, A_2, A_3, and α, respectively. A similar procedure for the case in which g_1 is in each of the remaining $\langle 110 \rangle$ directions and $\vec{H}$ is still in the $(1\bar{1}0)$ plane yields equations (4-4) through (4-9). However, the geometry is considerably more involved.

The relation for g in equation (4-10) can be derived by reference to Figure 30 which shows g_1 in the $[1\bar{1}0]$ direction and $\vec{H}$ in the (001) plane. The angles φ_1, φ_2, and φ_3 between $\vec{H}$ and the directions of g_1, g_2, and g_3 can be determined from Figure 30 as follows.

$$\varphi_1 = 45^\circ + \theta \quad \text{(A-2)}$$

$$c^2 = a^2 + b^2 - 2ab\cos\varphi_2$$

But, $$c^2 = h^2 + a^2 + b^2\cos^2\psi - 2ab\cos\psi\cos(45^\circ - \theta)$$
$$= b^2\sin^2\psi + a^2 + b^2\cos^2\psi - 2ab\cos\psi\cos(45^\circ - \theta)$$

Therefore, $$\cos\varphi_2 = \cos\psi\cos(45^\circ - \theta) \quad \text{(A-3)}$$
$$\equiv \cos\psi\sin(45^\circ + \theta)$$

Similarly, $$c'^2 = a^2 + b'^2 - 2ab'\cos\varphi_3$$

But, $$c'^2 = b'^2\cos^2\psi + a^2 + b'^2\sin^2\psi - 2ab'\sin\psi\cos(90^\circ + 45^\circ + \theta)$$

Thus, $$\cos\varphi_3 = -\sin\psi\sin(45^\circ + \theta) \quad \text{(A-4)}$$

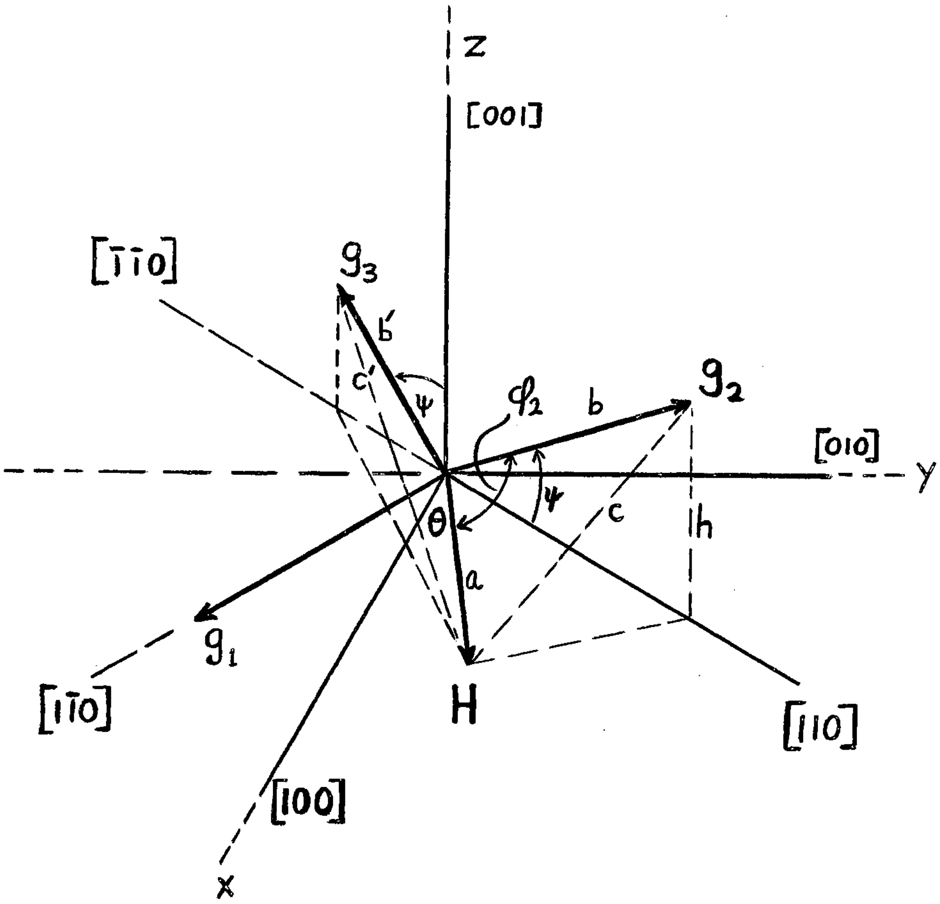

the angle φ_3 (not shown) is the angle between g_3 and H

Figure 30. Geometry Used in Deriving Equation (4-10).

When the expressions in equations (A-2), (A-3), and (A-4) are substituted into equation (2-24) the expression for g in equation (4-10) of the text is obtained. A similar procedure for the case in which g_1 is in each of the remaining $\langle 110 \rangle$ directions and $\vec{H}$ is in the (001) plane leads to equations (4-11) through (4-15).

The relation for $\cos^2 \varphi_1$ multiplying g_1^2 in equation (4-16) can be derived with the aid of Figure 31 which shows g_1 in the $[110]$ direction and $\vec{H}$ in the (111) plane. Reference to Figure 31 leads to the expression for $\cos \varphi_1$ in the following manner.

$$c^2 = a^2 + b^2 - 2ab\cos\varphi_1$$

$$= h^2 + e^2 + a^2 - 2ea\cos(90^\circ + \theta')$$

But, $h^2 = b^2 - e^2$ and thus

$$b\cos\varphi_1 = -e\sin\theta' \tag{A-5}$$

Since $b^2 = \frac{f^2}{2} + e^2$, $f^2 = b^2 + 2 - 2b\sqrt{2}\cos\theta$, and $\frac{f^2}{2} = e^2 + 2 - 2e\sqrt{2}\cos\theta'$, a little manipulation shows that

$$\cos\theta' = \frac{b}{e}\cos\theta \tag{A-6}$$

When equations (A-5) and (A-6) are combined, the following results.

$$\cos\varphi_1 = -\sqrt{\frac{1}{2} - \frac{1}{b^2} + \frac{\sqrt{2}\cos\theta}{b} - \cos^2\theta} \tag{A-7}$$

Finally, $\cos(30^\circ - \theta) = \frac{K}{b} = \frac{\sqrt{2}\sin 60^\circ}{b}$ or

$$\frac{1}{b} = \frac{2\cos(30^\circ - \theta)}{\sqrt{6}} \tag{A-8}$$

When equations (A-7) and (A-8) are combined and simplified, the following expression is obtained.

$$\cos\varphi_1 = \frac{1}{\sqrt{3}}\sin\theta \tag{A-9}$$

Squaring the relation in equation (A-9) to obtain $\cos^2\varphi_1$ yields the factor multiplying g_1^2 in equation (4-16). The expressions for $\cos^2\varphi_2$ and $\cos^2\varphi_3$ multiplying g_2^2 and g_3^2, respectively, in

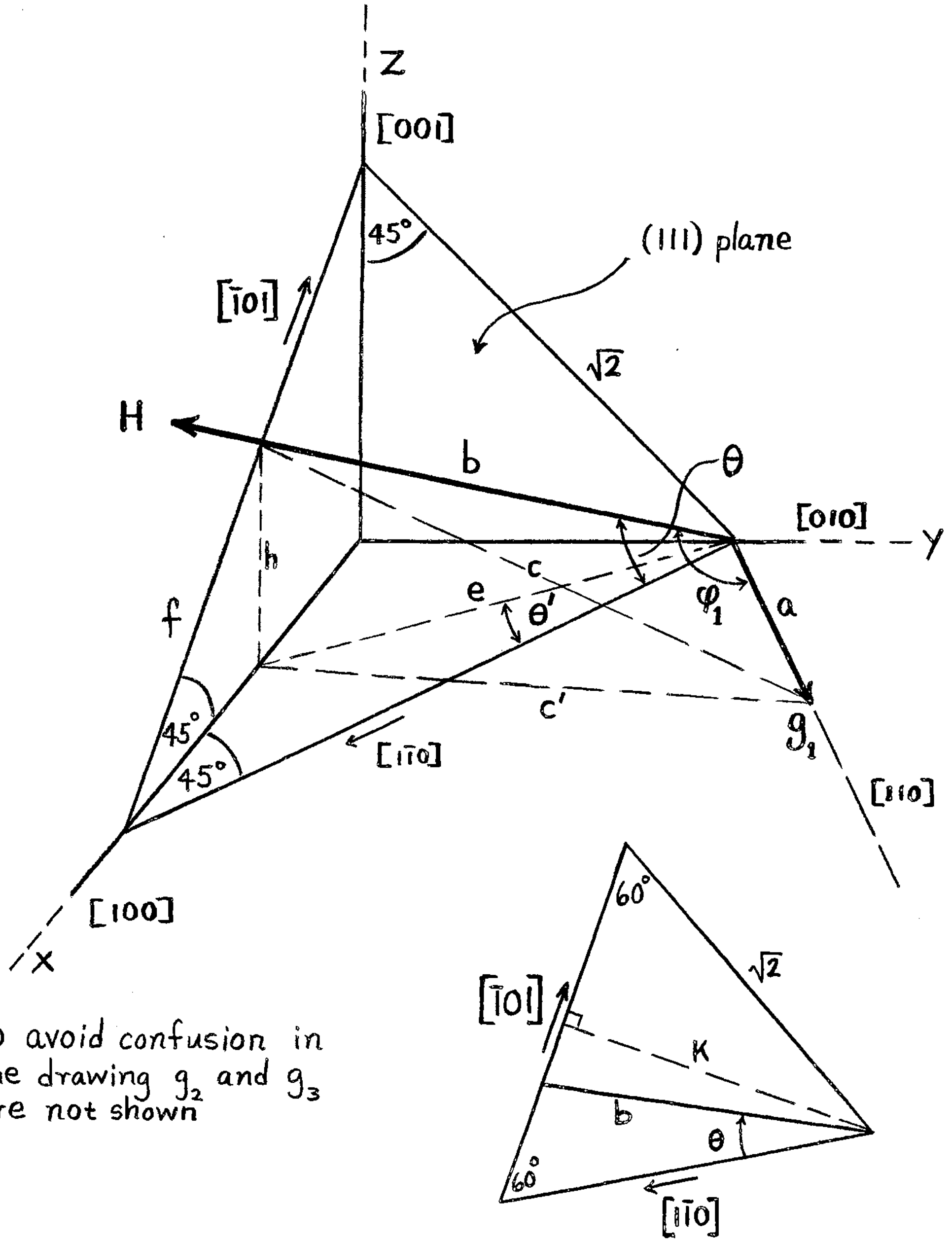

to avoid confusion in the drawing g_2 and g_3 are not shown

Figure 31. Portion of Geometry Used in Deriving Equation (4-16).

equation (4-16) can be obtained from Figure 31 by drawing g_2 and g_3 in their proper positions. (g_2 and g_3 were not shown in Figure 31 because their presence would have cluttered the diagram for the derivation of cos φ_1 .) The components g_2 and g_3 lie in the (110) plane and g_2 makes an angle ψ with the $[\bar{1}10]$ axis. The geometry is more complicated for the calculation of cos φ_2 and cos φ_3 . Following a similar procedure in calculating the cos φ_i for the case in which g_1 lies in each of the remaining $\langle 110 \rangle$ directions and $\vec{H}$ is in the (111) plane yields equations (4-17) through (4-27) in the text.

VITA

3

Paul Edward Klingsporn

Candidate for the Degree of

Doctor of Philosophy

Thesis: ANALYSIS OF UNUSUAL ELECTRON SPIN RESONANCE SPECTRA IN DIAMONDS

Major Field: Physics

Biographical:

Personal Data: Born in Monett, Missouri, September 3, 1940, the son of Mr. and Mrs. Urban Klingsporn.

Education: Graduated from Monett High School, Monett, Missouri, in May, 1958; received the Bachelor of Science degree from Southwest Missouri State College in August, 1961, with a major in physics; received the Master of Science degree from Kansas State College of Pittsburg in May, 1964, with a major in physics; completed requirements for the Doctor of Philosophy degree at Oklahoma State University in August, 1969.

Professional Experience: Student instructor of general physics, Oklahoma State University, 1965-67.

Organization: Member of Society of Physics Students, and associate member of Sigma Xi.